

Mathematics and biophysics of cortical microtubules in plants

by

Jun Allard

A THESIS SUBMITTED IN PARTIAL FULFILLMENT OF
THE REQUIREMENTS FOR THE DEGREE OF

DOCTOR OF PHILOSOPHY

in

The Faculty of Graduate Studies

(Mathematics)

THE UNIVERSITY OF BRITISH COLUMBIA

(Vancouver)

December 2010

© Jun Allard 2010

Abstract

Microtubules confined to the two-dimensional cortex of elongating plant cells must form a parallel yet dispersed array transverse to the elongation axis for proper cell wall expansion. Collisions between microtubules, which migrate via hybrid treadmilling, can result in plus-end entrainment (“zipping”) or catastrophe. Here, I present (1) a cell-scale computational model of cortical microtubule organization and (2) a molecular-scale model for microtubule-cortex anchoring and collision-based interactions between microtubules. The first model treats interactions phenomenologically while the second addresses interactions by considering energetic competition between crosslinker binding, microtubule bending and microtubule polymerization. From the cell-scale model, we find that plus-end entrainment leads to self-organization of microtubules into parallel arrays, while collision-induced catastrophe does not. Catastrophe-inducing boundaries can tune the dominant orientation. Changes in dynamic-instability parameters, such as in *mor1-1* mutants in *Arabidopsis thaliana*, can impede self-organization, in agreement with experiment. Increased entrainment, as seen in *clasp-1* mutants, conserves self-organization, but delays its onset. Modulating the ability of cell edges to induce catastrophe, as the CLASP protein may do, can tune the dominant direction and regulate organization. The molecular-scale model predicts a higher probability of entrainment at lower collision angles and at longer unanchored lengths of plus-ends. The models lead to several testable predictions, including the effects of reduced microtubule severing in katanin mutants and variable membrane-anchor densities in different plants, including *Arabidopsis* cells and *Tobacco* cells.

Table of Contents

Abstract	ii
Table of Contents	iii
List of Tables	vi
List of Figures	vii
List of Abbreviations	viii
Acknowledgements	ix
Statement of Co-Authorship	x
1 Introduction	1
1.1 Microtubules	1
1.2 Functions of microtubules	4
1.2.1 Asters and organelle positioning	5
1.2.2 The mitotic spindle and the cell cycle	5
1.2.3 Plant CMTs and cell elongation	6
1.3 Brief chapter summaries	8
2 Plant cortical microtubules and mathematical modelling . .	10
2.1 Introduction	10
2.2 Plant morphology: Why plants need cortical microtubules . .	10
2.2.1 Modelling plant morphology	13
2.3 Experimental data	15
2.3.1 Representing individual MTs	15
2.3.2 Collision resolutions	16
2.3.3 Nucleation and density	19
2.3.4 Severing at crossover	20
2.3.5 Cell geometry	21
2.3.6 Angle distribution	21
	iii

Table of Contents

2.3.7	Mutants and other experimental perturbations	22
2.4	Mathematical models of CMT organization	24
2.4.1	Classes and aims of mathematical models	24
2.4.2	Liquid crystals	25
2.4.3	Angle-dependent collision resolutions	26
2.4.4	Collision-induced pausing	26
2.4.5	Mean-field analysis	26
2.4.6	Simulations that match mutants	27
2.4.7	Dynamics on polyhedral cells	28
2.4.8	Dynamics on cylindrical cells	29
2.4.9	Organization from a simplified catastrophe model	29
2.5	Outlook: Branching of new questions from existing ones	30
3	Biophysical basis of cortical microtubule interactions	32
3.1	Introduction	32
3.2	MT-cortex anchoring	33
3.3	MT-MT interactions	36
3.3.1	Collision-induced catastrophe	37
3.3.2	Crossover	40
3.3.3	Plus-end entrainment	42
3.4	Entrainment and crossover probabilities	48
4	Cortical microtubule organization at the cell scale	52
4.1	Introduction	52
4.2	Materials and methods	52
4.2.1	Details of computer simulation	58
4.3	Results	60
4.3.1	Collision-induced catastrophe only	60
4.3.2	Plus-end entrainment	62
4.3.3	The <i>mor1-1</i> mutant	62
4.3.4	Static minus-ends	65
4.3.5	Increased entrainment	66
4.3.6	Branched nucleation	67
4.3.7	Cell boundaries	67
4.4	Discussion	69
5	Cell edges can drive cortical microtubule organization	73
5.1	Introduction	73
5.2	Biophysical basis for edge-induced catastrophe	73
5.3	Computer modelling of cell edge effects on MT organization	75

Table of Contents

5.4	Discussion	80
6	Conclusions	82
6.1	Mathematical modelling techniques	82
6.2	The reductionist approach in cell biology	83
6.3	The appeal of modelling plant cortical microtubules	85
	Bibliography	86

Appendices

A	PDE models and the mean field approximation	100
A.1	The five-dimensional system	100
A.2	Spatial homogenization	101
A.2.1	Asymptotic expansion in p	102
A.2.2	Discussion	104
B	Orientational order parameters in 2D	105
B.1	Introduction	105
B.2	Defining four order parameters	105

List of Tables

3.1	Anchoring kinetics	34
3.2	Dimer-level parameters	39
3.3	Collision resolution parameters	44
4.1	Dynamic instability parameters	55
4.2	Cell-level parameters	56
5.1	Edge-induced catastrophe probabilities	76

List of Figures

1.1	Microtubule polymer structure	2
1.2	Microtubule structures in plants	7
1.3	The cortical microtubule array	8
2.1	Plant anatomy	11
2.2	Pathway of plant morphology	14
2.3	Schematic depictions of collision resolutions	17
2.4	Collision resolution probabilities	18
3.1	Free length distribution	35
3.2	Collision resolution schematics	37
3.3	Collision-induced catastrophe	41
3.4	Pathway of entrainment	46
3.5	Entrainment probabilities	50
4.1	Collision detection algorithm	59
4.2	CIC-only snapshots	61
4.3	CIC and entrainment snapshots	63
4.4	Time series and angle distributions from WT simulation	64
4.5	Time series and angle distributions from <i>mor1-1</i> simulations	65
4.6	Snapshots from modified simulations	68
4.7	Local order emerges near boundaries	70
5.1	Biophysical basis for edge-induced catastrophe	75
5.2	(A)-(C). Simulations with edge interactions	77
5.2	(D)-(E). Simulations with edge interactions	78
5.2	(F)-(G). Simulations with edge interactions	79
6.1	Pathway of CMT organization	84

List of Abbreviations

CIC Collision-induced catastrophe

CLASP CLIP-associated protein

CMT Cortical microtubule

EB1 End-binding protein 1

γ -TuRC γ -tubulin ring complex

GDP Guanine diphosphate

GTP Guanine triphosphate

MAP Microtubule-associated protein

MOR1 Microtubule organizing protein 1

MT Microtubule

MTOC Microtubule organizing centre

PDE Partial differential equation

PPB Preprophase band

SP edge Side-periclinal edge

TP edge Transverse-periclinal edge

TS edge Transverse-side edge

WT Wild type

Acknowledgements

I thank my advisor, Eric Cytrynbaum, who treated me as a scientific peer and provided the desire and technical skill so that I may eventually become one. I thank Geoffrey Wasteneys and Chris Ambrose (UBC Botany) for rewarding collaborations; UBC Mathematical Biology, especially Leah Edelstein-Keshet, Dan Coombs and their graduate students and post-docs, for an ecosystem in which it is impossible not to develop affection for science; Eldon Emberley (Simon Fraser Physics), Andrew Rutenberg (Dalhousie Physics), David Odde (Minnesota, Biomedical Engineering) and Bela Mulder (FOM Institute AMOLF, Netherlands) for valuable discussions; and Terry Soo, Alan Lindsay, Jennifer Morrison, Matt Matchett, Joey Basque, Lindsay Donders and Jacques Allard for support.

This work was financially supported by NSERC and the Pacific Institute for Mathematical Science IGTC. Computer resources were provided by WestGrid (Compute/Calcul Canada).

Statement of Co-Authorship

Eric Cytrynbaum, Geoffrey Wasteneys and Chris Ambrose have been involved in all projects presented in this thesis, providing feedback and technical expertise. In all cases, I developed the mathematical/biophysical models, designed and wrote computer programs in C and Matlab, performed the computation and mathematics, and analyzed the resulting data. I wrote first drafts of the manuscripts, which were edited by Eric Cytrynbaum (Chapters 3-5), Geoffrey Wasteneys (Chapters 3-5), and Chris Ambrose (Chapters 3 and 5).

In Chapter 3, a biophysical model of cortical microtubule interactions, Chris Ambrose provided experimental data on microtubule free lengths, including crucial statistical distributions as opposed to just averages which had been previously published.

Chapter 5, the effect of cell edges, is the computational part of a joint experimental-computational study. Chris Ambrose and I designed the computational research, which I performed and analyzed. Portions of the Introduction (Sec. 5.1) and Discussion (Sec. 5.4) were written by Chris Ambrose.

Chapter 1

Introduction

Microtubules (MTs) are long rigid structural polymers that form part of a living cell’s “cytoskeleton” [1]. These dynamic polymers can grow and shrink in response to stimuli and play an important role in many cell functions, including mitosis [1], organelle positioning [88], axon formation in neurons [38, 119], immune cell activation [17], cell shape determination [34], cell motility [95] and vesicle transport [103]. They are implicated in disease including Alzheimer’s disease [12], Parkinson’s disease [49], many forms of cancer [82] and transmission of bacterial infection [99]. MTs exist in animal, plant and fungal cells, but many of their roles are different.

MTs form a variety of ordered structures inside cells of different organisms. A fundamental question is how MTs become organized into these structures. Specifically, how do the molecular properties of MTs and associated components result in the emergence of MT organization in a manner that is responsive to the cell’s environment? In plant cells, one MT structure is the the cortical MT (CMT) array. The aim of this thesis is to address the above question in the context of the plant CMT array.

1.1 Microtubules

MTs are polymers composed of dimers of the proteins α -tubulin and β -tubulin, arranged in a hollow cylinder 25 nm in diameter. The length of MTs varies and can reach up to $10^3 \mu\text{m}$ *in vivo* [140]. MTs are members of the class of biological polymers that constitute the cytoskeleton. In eukaryotes, the cytoskeleton consists of MTs and microfilaments of the protein actin [1]. Animal cells contain a third kind of cytoskeletal element called intermediate filaments, whose presence in plants is debated [19, 68]. In bacteria, homologues of all three cytoskeletal proteins exist [26].

MTs are highly dynamic due to polymerization. They are polar, with distinct polymerization properties at the so-called plus-end and minus-end. The plus-end randomly switches between states of growth, rapid shrinking [94] and intermittent pauses [120]. Transition from growth to shrinkage is

1.1. Microtubules

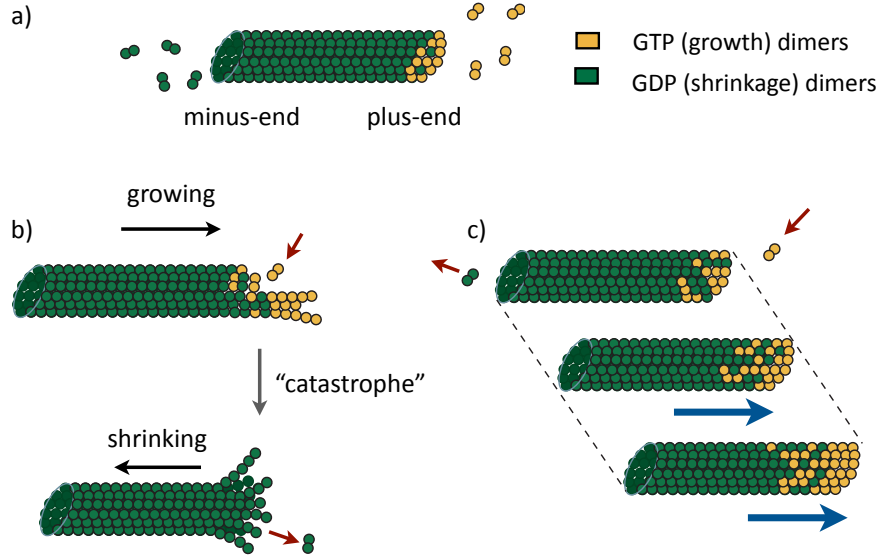


Figure 1.1: Schematic of the structure of a MT, shown in (a) as a tube composed of dimers of the protein tubulin that is associated with either GTP (yellow) or GDP (green). (b) A MT switches between growth and shrinkage, known as ‘dynamic instability’. (c) Depolymerization at the minus-end and dynamic instability at the plus-end leads to hybrid treadmilling, discussed in Sec. 2.3.1.

known as catastrophe, and transition from shrinkage to growth is known as rescue. This behaviour is termed dynamic instability.

The polymerization properties of individual MTs are represented in different ways [21, 46, 90, 129]. A common model, referred to here as the growth-state model, was described by Mitchison and Kirschner [94] and developed in partial differential equation (PDE) form by Dogterom and Leibler [46] (described explicitly in Sec. 4.2). This model, in either PDE form or individual-based form (see Sec. 2.4.1), represents MTs as rods with a continuous length (in microns, as opposed to number of subunits) and assumes transition times between growth states and shrinkage states to be exponentially distributed. This model predicts that, in the absence of interactions, MTs will be exponentially distributed in length. Experiment has confirmed both exponentially distributed lengths [80] and transition times [74], although both theoretical and experimental evidence exists for non-exponential transition times [105]. Omitting nucleation, the growth-state

1.1. Microtubules

model is described by four parameters: growth and shrinkage velocities and two transition rate constants. These polymerization properties emerge from the molecular properties of MTs. The dimers of tubulin can be associated with either GTP or GDP (guanosine triphosphate and guanosine diphosphate, respectively). Dimers at the plus-end are GTP-associated. Catastrophe is the spontaneous switch of the MT plus-end from a state in which growth dominates, to a state in which shrinkage dominates, due to the loss of the polymerization-promoting GTP-tubulin cap through hydrolysis.

In addition to their polymerization properties, the dynamics of MTs are also affected by their mechanical properties. The elastic properties of a biopolymer can be interpreted using the linear elastic rod model [10] in which the mechanical energy is

$$H = \int \frac{1}{2}B [\text{curvature}]^2 + \frac{1}{2}C [\text{twist}]^2 + \frac{1}{2}D [\text{stretch}]^2 + \frac{1}{2}F [\text{shear}]^2 dl$$

where there are four possible modes of deformation (bending/curvature, twist, stretch and shear), each with an associated elastic modulus (A , B , C , D , F). The parameter B is the bending rigidity, also known as the flexural rigidity or bending modulus, with units of pN nm² ($= 10^{-30}$ N m²). Typically for biopolymers such as MTs, bending as described by the curvature is the most important mode of deformation [6]. For MTs, experiments have measured bending rigidities ranging over $B \approx 1 \times 10^6$ to 44×10^6 pN nm² [129]. For uniform, isotropic materials [85], the elastic modulii are related by

$$B = EI \tag{1.1}$$

$$C = GI \tag{1.2}$$

$$D = EA \tag{1.3}$$

$$F = GA \tag{1.4}$$

where E is the Young's modulus, G is the shear modulus of the material, A is the cross-sectional area and I is the second moment of the area. Mickey and Howard [91] calculated the Young's modulus of a MT to be $E = 1.4\text{GPa} = 1.4 \times 10^3$ pN/ nm², roughly the same as the Young's modulus computed for actin, intermediate filaments, collagen (another biopolymer) and DNA [71]. The similarity of Young's modulii for those biopolymers suggests the uniform, isotropic model of biopolymers is appropriate. This further suggests that the cylindrical structure of MTs endows them with high bending stiffness, since a hollow cylinder has larger I than an equal amount of mass concentrated in a linear or helical polymer.

1.2. Functions of microtubules

Both polymerization and mechanical properties of MT dynamics described above are affected by other proteins, collectively known as MT-associated proteins (MAPs) that bind polymerized tubulin. A few MAPs are listed here.

- The animal XMAP215 [129] and its plant homologue MOR1 [136] bind along the length of MTs and modify their dynamic instability parameters.
- In animals, the CLASP protein captures MT plus-ends near the cell cortex, possibly by decreasing the hydrolysis rate of GTP-tubulin dimers and therefore down-regulating the catastrophe rate [92]. CLASP is also present in plant cells, and its function is discussed in Sec. 2.3.7.
- Katanin, named for the Japanese word *katana* meaning “sword”, severs MTs along their length, often near their minus-end [130].
- A protein genetically related to tubulin, called γ -tubulin, forms a ring known as the γ -tubulin ring complex (γ -TuRC) which nucleates new MTs [88].
- Members of the plant MAP65 family, and its homologues Ase1p [75] in fission yeast *Schizosaccharomyces pombe* and PRC1 in humans [89], is involved in bundling adjacent MTs [137].
- Phospholipase-D binds MTs in plants and is involved in anchoring MTs to the cell membrane [53].
- A class of MAPs important in many cell functions are MT-based molecular motors dynein and kinesin [71]. These motors move along the length of MTs at speeds up to $7\text{ }\mu\text{m/s}$ and have the ability to generate forces up to tens of pN [71].

Studies of MTs are aided by drugs that affect MT dynamics. The drug taxol [31, 92, 132] stabilizes MTs by inhibiting their polymerization dynamics, and affects MT mechanical rigidity, although it is unclear how [129]. The drug oryzalyn [8, 125], in contrast, induces depolymerization of MTs in plants and protists, but not in animal cells.

1.2 Functions of microtubules

As mentioned, MTs in cells form various structures that play a role in several vital cell functions. Three structures and their functions are discussed

1.2. Functions of microtubules

here: asters and organelle positioning, the mitotic spindle and eukaryotic cell division, and plant CMTs and plant cell elongation.

1.2.1 Asters and organelle positioning

A common structure formed by MTs in cells is a polarized, radial array [40, 88] in which the minus-ends are anchored and stabilized at a focus, and the plus-ends extend outward from this focus. The focus is one example of a MT organizing centre (MTOC) and the array is called an aster, after the greek word $\alpha\sigma\tau\eta\rho$ meaning “star”. The focus is typically near the geometric centre of the cell and/or on the surface of the cell nucleus [140]. Indeed, the astral structure is required for the proper centering of the cell nucleus, as well as centering other cell components including pigment granules in melanophores [40] (the cells that endow exothermic (cold-blooded) animals with skin colour).

How asters form and how they approximately find the cell centre is yet to be fully elucidated. In animals, the MTOC is made of a protein structure called a centrosome. Fission yeast *Schizosaccharomyces pombe* and budding yeast *Saccharomyces cerevisiae* have a structure called the spindle pole body, which serves a similar function at the centrosome in animal cells. The centrosome and spindle pole body contain γ -TuRC, which nucleates new MTs and anchors their minus-ends to the centrosome. Some cells lacking centrosomes exhibit asters. In certain plant cells, astral structures form when γ -TuRC localizes to the nuclear membrane. MTs can self-organize into astral structures in anucleate cells and *in vitro* in vesicles [102, 111] with the help of molecular motors.

How do asters find the centre of the cell? Proposed mechanisms differ depending on the cell. For cells whose radius is $\sim 5 \mu\text{m}$, such as fission yeast *S. pombe*, MTs can drive the aster towards the cell centre by pushing on the cell boundaries [40]. In larger cells with radius $\sim 50 \mu\text{m}$ such as eggs of nematode *Caenorhabditis elegans*, pushing forces are complicated since long MTs may buckle under less force (although this is debated in the context of a mechanically resistive cytoplasm) [140], and pulling forces by molecular motors at the cell boundary may contribute to centering [22].

1.2.2 The mitotic spindle and the cell cycle

A key step in the process of a replicating eukaryotic cell is mitosis [1], the process during which the chromosomes are transported to opposing poles of the mother cell such that one copy each is inherited by each of the two

1.2. Functions of microtubules

daughter cells. Mitosis is temporally divided into several phases. The time between successive divisions is called interphase, during which the DNA is replicated. During prophase in animals including *C. elegans*, the frog *Xenopus laevis*, the fruit fly *Drosophila melanogaster* and humans, a microtubule structure forms when the two asters move to opposite ends of the cell. This aster-derived structure is called the mitotic spindle. The mitotic spindle attaches to the chromosomes (during metaphase), along with molecular motors, in structures called kinetochores, and eventually corresponding pairs of chromosomes are pulled apart (during anaphase) with the help of molecular motors. Mitosis is followed by cytokinesis, during which the mother cell is physically split into two daughter cells.

Cell division in budding yeast *S. pombe* and fission yeast *S. cerevisiae* differs from cell division in animals, where the mitotic spindles are comprised of fewer motors, MTs and chromosomes [54, 75, 107, 110].

Mitosis is different in higher plants such as *Arabidopsis thaliana* since, as mentioned above, they do not contain centrosomes. Before prophase, a ring of MTs and actin filaments forms at the site of the future cell wall, near midcell. This band of cytoskeletal elements is called a preprophase band (PPB) [130].

1.2.3 Plant CMTs and cell elongation

Unlike animal cells, plant cells have a stiff cell wall outside the cell membrane. The cell wall is composed primarily of cellulose, which is synthesized in the plasma membrane, then exported to the cell exterior and incorporated into the cell wall [133]. Isotropic insertion of new cell wall material would lead to isotropic cell expansion. Thus plant cells that undergo anisotropic, unidirectional expansion, such as elongating root cells and elongating stem cells, require a mechanism to direct cell wall growth. The internal turgor pressure of plant cells (0.3-0.9 MPa [123]) complicates the task of anisotropic expansion.

While the mechanism of anisotropic cell expansion involves many components, described in Sec. 2.2, a key component is a MT structure located at the cell cortex, the inner surface of the cell membrane. Here, plant CMTs form *de novo* and organize into an array in which they are parallel to each other, yet dispersed throughout the cortex of cell faces that will undergo elongation. A schematic is shown in Fig. 1.2 and a fluorescence image of a CMT array is shown in Fig. 1.3. The direction perpendicular to the CMT array is the direction of anisotropic cell elongation.

Unlike the other MT structures described above, plant CMTs lack an

1.2. Functions of microtubules

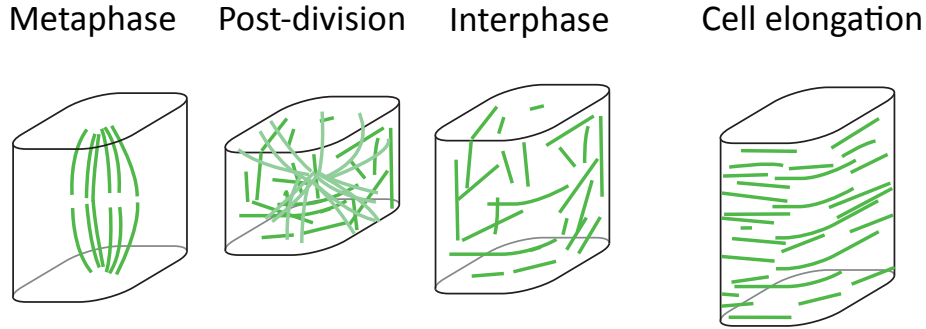


Figure 1.2: Structures formed by MTs in elongating plant cells. From left to right, the mitotic spindle during metaphase, followed by disassembly and reformation at the cortex. During interphase, the MTs reform at the cortex and either remain randomly arranged, if the cell is in the division zone, or become parallel, if the cell is in the elongation zone.

organizing centre to which their minus-ends are attached. Because of the lack of organizing centre, the CMTs are said to be acentrosomal and the CMT array is said to self-organize. The self-organization of plant CMTs occurs in most elongating cells of most higher plants including *Arabidopsis*.

Since CMTs are confined to the two-dimensional surface of the cortex, they can interact with one another upon contact in several ways. Among these are “entrainment”, discussed in detail in Sec. 2.3.2, catastrophe and crossover. Schematic depictions of these collision resolutions are shown in Fig. 2.3. It has been conjectured that these interactions are sufficient to give rise to the organization of the CMT array [44]. In general, two scales of questions about CMT self-organization remain to be elucidated. First are cell-level questions: How do interactions between MTs give rise to cell-scale order? How do changes in the molecular interactions, and in cell geometry and intracellular signalling, affect self-organization? A second scale of questions is molecular: how do interactions such as entrainment and collision-induced catastrophe occur? Why do they occur at different frequencies for different collision angles? How are MTs held to the cortex and how does this anchoring affect MT-MT interactions?

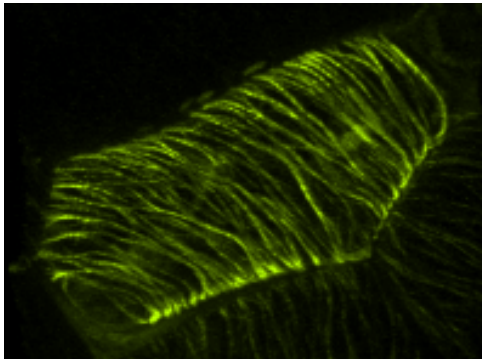


Figure 1.3: Fluorescence image of a CMT array in an elongating cell of *Arabidopsis*. Tubulin is labelled with GFP fluorescent markers. MT arrays in neighboring cells are visible. Obtained with permission from J. Christian Ambrose (UBC Botany).

1.3 Brief chapter summaries

This thesis presents mathematical models of CMTs in plants with a focus on two aspects: first, a quantitative understanding of the dynamics of microtubules based on mechanical and chemical first principles; and second, modelling that recapitulates and informs experiments, particularly data from fluorescence microscopy in *Arabidopsis* wild-type (WT) and mutants.

- In Chapter 2, I present biological background and review recent work on modelling CMTs, including a summary of the main results of this thesis. This review contains some general conclusions.
- Chapter 3 presents a biophysical model of how microtubules are attached to the plant cell cortex, and how this attachment drives interactions between colliding microtubules. This model, on the scale of individual microtubules, explains what gives rise to angle-dependent probabilities of specific interactions and quantitatively predicts these probabilities.
- Chapter 4 presents a model of CMT organization. In this cell-scale model, the microtubule interactions described in Chapter 3 are taken as phenomenological events. Modifications of the model allow us to address mutants, the function of MAPs and the relative importance of different collision resolutions. This model considers microtubules on a

1.3. Brief chapter summaries

two-dimensional surface either without boundaries, or on the surface of a cylinder.

- In Chapter 5, the cell-scale model is extended to include the effects of cell edges revealed in recent experiments of the Wasteneys lab. To more accurately depict the cortex of polyhedral cells, simulations take place on a cube.
- Finally, Chapter 6 contains overall conclusions and a discussion of the tools of mathematical modelling used in the thesis.

Chapter 2

Plant cortical microtubules and mathematical modelling

2.1 Introduction

In this review I discuss the two-dimensional array formed by MTs attached parallel to the cell cortex — the inside of the outer envelope of a plant cell — in elongating plant cells. Plant CMTs are the most prevalent microtubule array in the biosphere [39] and historically were among the first microtubules discovered [87]. Our understanding of CMT organization has made recent progress experimentally (For recent reviews see [47, 64, 132, 133]) and theoretically [2, 3, 48, 121, 126].

This chapter reviews CMT organization with an emphasis on theoretical modelling. In Sec. 2.2, I briefly locate CMT organization in the broader context of plant morphogenesis. In Sec 2.3, I summarize experimental and theoretical literature relevant to modelling. In Sec. 2.4, I summarize recent modelling efforts including my own, the results of which are presented in the remaining chapters of this thesis. Sec. 2.5 presents overall conclusions and open questions that drive continuing theory and experiment.

2.2 Plant morphology: Why plants need cortical microtubules

Many plant cells contain a variety of MT structures, summarized in Fig. 2.1. Elongating cells in the root, stem and petioles (defined in the figure) exhibit organized CMT arrays. The CMT array plays a role in the complex process in which a plant grows into a specific shape, which I describe here.

Being sessile, plants respond to their environment by modifying their morphology. Growth towards a stimulus is called *tropism* (in contrast to movement towards a stimulus, called *taxis*). A simplified description of the pathway leading to elongation, shown in Fig. 2.2, consists of seven steps, where there are many feedback loops and other complications.

2.2. Plant morphology: Why plants need cortical microtubules

Mature dicot (Arabidopsis)

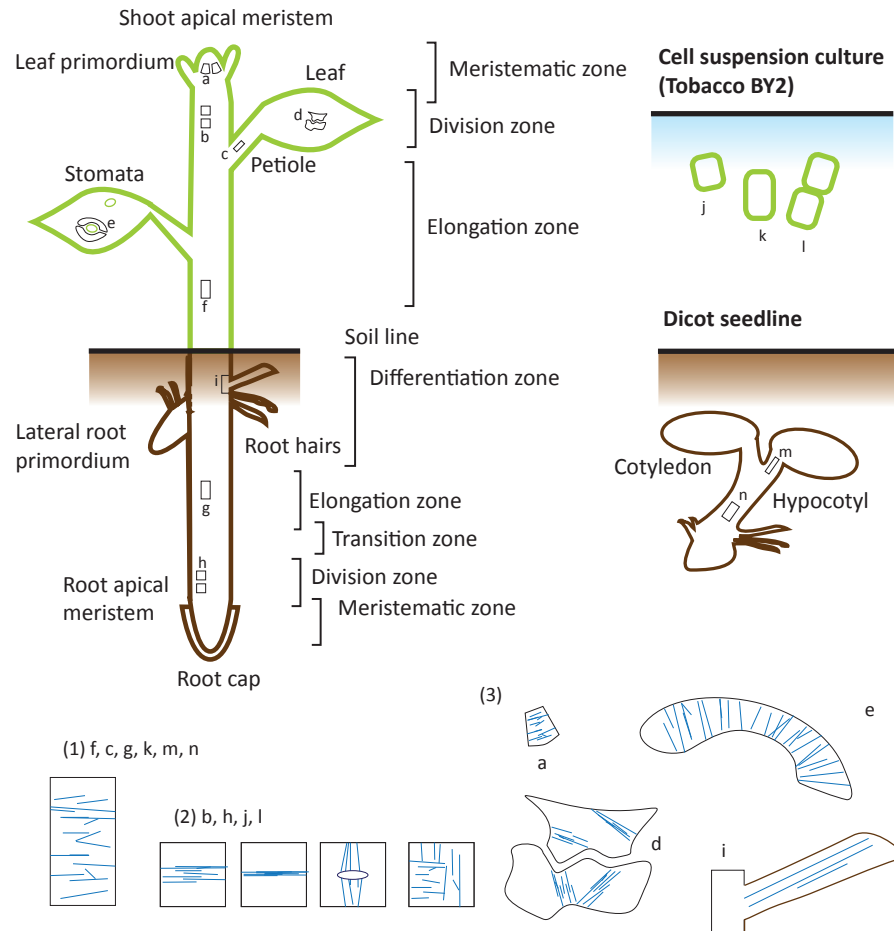


Figure 2.1: Schematic anatomy of a mature and seedling of a higher plant such as *Arabidopsis*, and cell suspension culture such as Tobacco BY-2. (a) Shoot apical meristem, (b) stem division zone cells, (c) petiole cells (d) puzzle-piece leaf pavement cells (e) guard cells surrounding stomata (f) stem elongating cell, (g) root elongating cell, (h) root division zone cells, (i) trichoblast and root hair, (j-l) cell suspension culture cells, (m) cotyledon petiole cells, (n) hypocotyl cells. Plant microtubules, shown in blue, exhibit different patterns. In (1) elongating cells, MTs are transverse to the axis of elongation. (2) Cells in various stages of the division cycle exhibit preprophase bands, phragmoplasts, spindles, and mixed-polarity cortical arrays. (3) In addition, a wide variety of cells have specialized MT patterns.

2.2. Plant morphology: Why plants need cortical microtubules

1. Environmental cue detection or execution of a default plan. Environmental cues include phototropism to light in the shoot [104], chemotropism to nutrients in the root [25], and in both organs gravity and touch [18].
2. Plant-wide (intercellular) signalling, either biochemically by hormones such as auxin, gibberellic acid and ethylene [124], or mechanically by stress [61]
3. Within-cell signalling: directly to MTs or via cell wall expansion machinery. In roots, CMTs receive two signals: one to self-organize, and another defining the major axis, to which their dominant direction will be transverse. Evidence that these two signals are independent comes from mutations in several genetic loci, which allow the CMT array to organize, but in an oblique dominant direction resulting in a helical array [72]. In addition, some mutants have organized arrays, but in random dominant directions that are uncoordinated between neighbouring cells [13]. Other mutants have disorganized CMTs [136]. With these separate signals, the CMT array self-organizes into the dispersed parallel arrays, and tunes its dominant direction. In either case, what is the pathway that takes the *intercellular* signals and transduces them *within-cell* to the CMT array? In leaf pavement cells, hormones signal to rho-of-plant proteins, which in turn signal to RIC1, which interacts directly with MTs [52]. For gravity and touch response in roots, EB1 is involved [18].
4. Self-organization of CMTs. The mechanism enabling MAPs and cell geometry to effect CMT organization is the focus of the remaining sections in this review.
5. CMT signal to lateral cell wall expansion machinery. Since their discovery, researchers theorized that CMTs determine the direction of microfilaments upon their insertion [87]. However, many contraindications [15], including the observation, aided by the *mor1-1* mutant, that the microfibrils and microtubules can each be disrupted independently [69], led to a new hypothesis that CMTs strengthen the cellulose microfilaments, possibly by regulating their length [131]. Thus, with disrupted CMT organization, plant cells can still grow albeit with defects [7, 61, 78]. There is also evidence of feedback from the cell wall to the CMTs [133].

2.2. Plant morphology: Why plants need cortical microtubules

6. Cell growth and anisotropy. As new microfibrils are inserted, they resist the turgor pressure and define the shape of the cell.
7. Organ shape and plant morphology arise ultimately from the shape and arrangement of the constituent cells.

2.2.1 Mathematical modelling of plant morphology and its components

Several steps in the multi-scale pathway leading to tropism (growth towards a stimulus) have been aided by mathematical modelling, some of which I review here.

Intercellular signalling by hormones

Long-range signalling is mediated in part by plant hormones. Plant roots are divided into several zones (Fig. 2.1) including (i) the root apical meristem, where cell division is controlled to produce either downward growth of the primary root or the formation of secondary (lateral) meristems, (ii) the division zone, where cells divide in a plane transverse to the major axis, and (iii) the elongation zone, where cells cease dividing and undergo anisotropic growth. Grieneisen et al. [59] developed a computational model of auxin, and demonstrated that a pattern of auxin-efflux channels (PINs) are sufficient to generate the auxin gradient seen experimentally, and explain the emergence of the different zones. The auxin pattern does not require inhomogeneous auxin sinks or sources, as had been assumed [51]. Further, by assuming that local levels of auxin result in either cell differentiation or cell elongation, Grieneisen et al. [59] demonstrated that the auxin gradient can maintain the defined zones. Their model recapitulates behaviour on multiple timescales: formation of the auxin gradient occurs in hours, while cell and organ expansion occur after tens of days. Laskowski et al. [86] extended the model of Grieneisen et al. [59] and demonstrated that auxin-dependent initiation of lateral roots arises naturally after the apical root is bent.

Intercellular signalling by mechanical forces

Hamant et al. [61] developed a model of plant morphogenesis incorporating the hypothesis of feedback between CMTs and wall expansion. The stem of *Arabidopsis*, similar to the root, has an apical meristem that must produce cells that either divide and elongate in the major axis, extending the

2.2. Plant morphology: Why plants need cortical microtubules

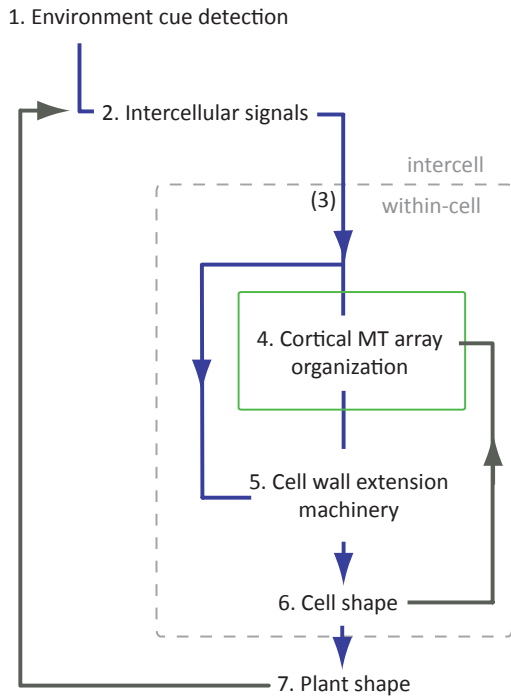


Figure 2.2: The pathway of plant morphology. In this simplified flow chart, environmental cues are detected, leading to intercellular signalling to individual cells, and within-cell signalling to the cell wall insertion machinery and the CMT array. This results in anisotropic cell growth and division, establishing organ shape and ultimately overall plant shape. Many steps are hypothesized based on experimental and theoretical evidence (see main text). There are many feedback loops, some of which are shown (grey arrows). Grey dashed box indicates intercellular signalling and within-cell signalling. Green box indicates the focus of this thesis. A detail of the pathway within the green box is presented in Fig. 6.1.

stem, or differentiate into leaf primordia. By assuming that CMTs in each cell orient parallel with the principal stress in that cell, Hamant et al. [61] recapitulated the MT arrays they observed in the shoot apical meristem.

2.3. Experimental data

Further, by assuming a feedback loop between wall stiffness anisotropy and CMT direction, the model reproduces details of plant morphology as well as defects that occur when MTs are perturbed by the drug oryzalin.

Organ shape and plant shape

Finally, the direction of growth and division of individual cells gives rise to the shape of organs and ultimately the entire plant. Plant morphogenesis has interested theoreticians for decades [57, 93]. For nontrivial geometries, modelling has demonstrated how organ morphology emerges from local growth patterns [35, 70, 76]. Modelling has also successfully recapitulated the formation and growth of complex shapes such as cotyledons (the shoot apical meristem in seedlings, see Fig. 2.1) — where it has provided explanations for how many cotyledons a plant seed will develop [70] — trichoblasts (specialized root cells, see Fig. 2.1) and whole *Arabidopsis* and rice plants [35].

2.3 Experimental data, model parameters and model behavior

Mathematical modelling contributed to our recent understanding of several steps in the plant morphogenesis pathway and is poised to do so for CMT organization. In this section, I describe experimental data that will inform models.

2.3.1 Representing individual MTs

In plant CMTs, photobleaching studies show that individual tubulin sub-units remain mostly fixed relative to the cell cortex [120]. However, MTs are highly dynamic due to subunit turnover (polymerization) at the plus-end, which randomly switches between states of growth, rapid shrinking [94] and intermittent pauses [120].

The most common representation of MTs in the context of the plant cell cortex is the growth-state model. The four or eight parameters (for two-state or three-state models, respectively), referred to here as MT dynamic instability parameters or kinetic parameters, have been measured by a variety of researchers in *Arabidopsis* cotyledon and root cells [30, 73, 78, 101, 120] and Tobacco BY2 cells [44], making the growth-state model attractive for modellers. Eren et al. [48] use a modified version in which the growth and shrinkage rates are normal random variables, giving the model two addi-

2.3. Experimental data

tional parameters (standard deviations). These extra parameters have also been estimated experimentally [78, 120].

VanBuren et al. [128] developed a model for MT polymerization and catastrophe at the dimer level. In this model, dimers associate onto a 13-protofilament tube at a rate k_+^0 and dissociate at a rate

$$k_- = k_+^0 \exp(-\Delta G/k_B T) \quad (2.1)$$

where ΔG is the energy required to remove the dimer from the MT lattice. This energy is different for GTP-tubulin dimers, which favour growth, and GDP-tubulin dimers, which favour disassembly. Newly associated dimers are GTP-tubulin, and they switch to GDP-tubulin through GTP hydrolysis at rate k_{hyd} . This model has successfully described the action of MAPs and the effect of forces on MT plus-ends [2, 117]. This dimer-level model also produces roughly constant growth and shrinkage velocities, and exponentially distributed transition times. Thus, it can be thought of as a fine-grained model consistent with the coarse-grained growth-state model that tells us how the MT-level parameters (velocities and transition rates) are related to dimer-level parameters (on-rates, bond energies and hydrolysis rate). Consistency between scales is fortunate because the dimer-level model is computationally taxing to simulate and could not be used to represent more than a few MTs at a time. Allard et al. [2] (Ch. 3) estimate the dimer-level parameters that correspond to the MT dynamic parameters measured in *Arabidopsis*.

Another model of individual MTs has been developed [50, 90], which is both fine-grained to the dimer level and computationally simple enough to simulate on the cell level. This model represents a MT as a linear polymer of GTP-tubulin or GDP-tubulin subunits, and takes as input parameters polymerization and depolymerization rates for both states, and a hydrolysis rate for all subunits except the plus-end subunit. These rates can also be translated into MT dynamic parameters by formulae [90]. This model is used in the context of CMT organization by Shi and Ma [121], discussed in Sec. 2.4.9. Models that aim to explain dynamic instability at the level of individual dimers continue to be developed [21].

2.3.2 Collision resolutions

Since CMTs are approximately confined to a two-dimensional surface, the growing plus-end of one MT (herein referred to as the incident MT) can collide along the length of another (the barrier MT). The collision may result in several possible outcomes, some of which are depicted in Fig. 2.3. The

2.3. Experimental data

incident MT may undergo a catastrophe, which we refer to as a collision-induced catastrophe (CIC) in contrast to spontaneous catastrophe, or it may continue to grow unperturbed, crossing over the barrier MT. These outcomes have been reported at predominantly steep angles of collision [44]. At shallow angles of collision, the incident MT may become entrained with the barrier MT, after which the plus-end grows parallel to the barrier MT, resulting in a sharp bend in the MT at the site of collision. This phenomenon is commonly referred to as “zippering” [44], plus-end entrainment [3], or bundling [48]. Other collision outcomes are possible: the incident MT may buckle before the barrier [138] or it may cross over the barrier and continue in a perturbed direction [64]

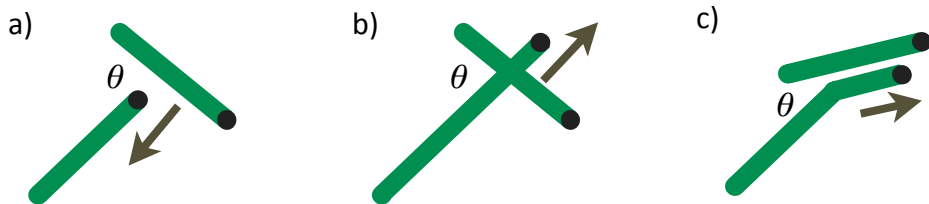


Figure 2.3: Collisions between CMTs may result in several possible outcomes. (a) The incident MT undergoes collision-induced catastrophe. (b) The incident MT crosses over the barrier MT unperturbed. (c) The incident MT is entrained by the barrier MT, becoming parallel and bundled to it. A more biophysically detailed version of this figure is shown in Fig. 3.2

A key insight of Dixit and Cyr [44] was that, upon a collision at angle θ , the probability of each collision resolution depends on the angle. That is, three functions $p_{cat}(\theta)$, $p_{ent}(\theta)$ and $p_{cross}(\theta)$ determine probabilistically the collision resolution. These collision resolution probabilities have been measured experimentally for Tobacco BY-2 cells [44]. Several other studies inform our knowledge of them, which is summarized in Fig. 2.4. Both experimental measurements and theoretical models [3, 48] sometimes approximate the full angle-dependent collision resolution probabilities as piece-wise constant functions (Fig. 2.4D). In this simplification, we specify a critical angle θ_{ent} . Below θ_{ent} , the probability of entrainment is a constant p_{ent} and the probability of CIC is zero. Above θ_{ent} , the probability of CIC is a constant p_{cat} , and the probability of entrainment is zero. Wightman and Turner [138] report that $p_{cat} = 24\%$ in *Arabidopsis* pavement cells (which do not form parallel arrays) and 9% in petiole cells (which do). Ambrose and Wasteneys

2.3. Experimental data

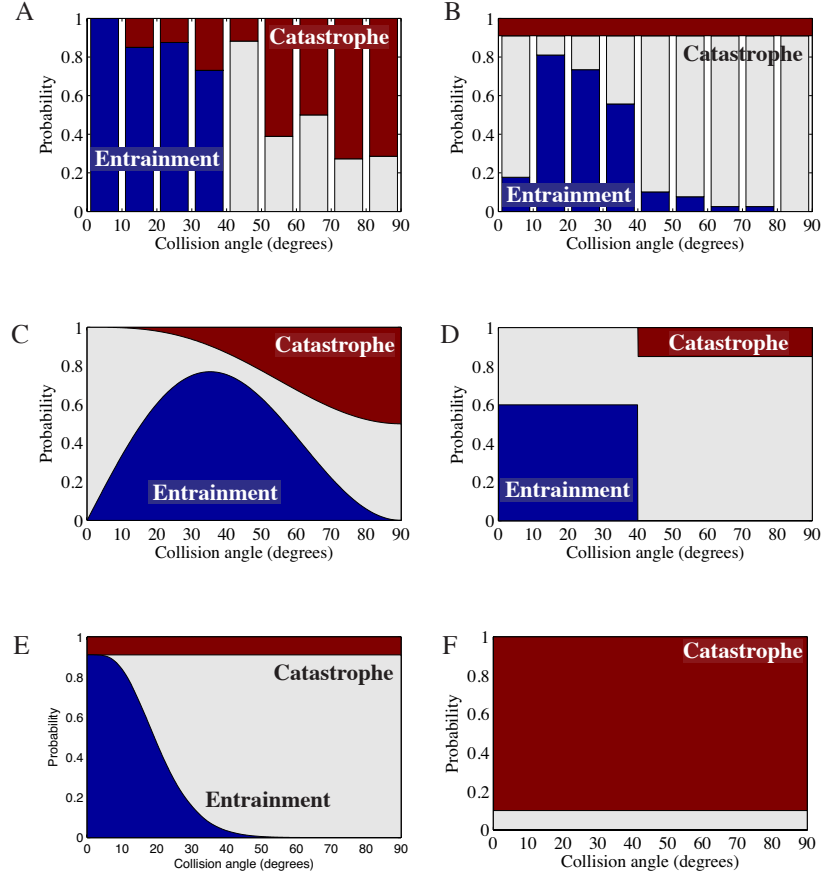


Figure 2.4: Collision resolution probabilities. When two MTs collide, the incident MT may undergo one of three possibilities, with different probabilities; entrainment (blue), collision-induced catastrophe (red) or crossover (grey). (A) Measured in Tobacco BY-2 cells [44]. (B) Measured in *Arabidopsis* elongating cells. The entrainment probability is inferred from Ambrose and Wasteneys [7] assuming uniformly distributed collisions (see main text) and catastrophe probability, assumed to be angle-independent, is from Wightman and Turner [138]. (C) Assumed collision resolution probabilities used for computer simulation by Tindemans et al. [126]. (D) Piecewise-constant collision resolution probabilities used as a simplifying assumption in the computer simulations of Allard et al. [3] (Ch. 4) and Eren et al. [48]. (E) Probabilities computed from a biophysical model in Allard et al. [2] (Ch. 3). (F) Angle-independent catastrophe-only simulated in Baulin et al. [16], Shi and Ma [121] and Allard et al. [3] (Ch. 4).

2.3. Experimental data

[7] report full angle-dependent entrainment data, but rather than the probability a collision will result in entrainment, they report the distribution of all entrainments, $p(\theta|ent)$, which is related to $p_{ent}(\theta)$ by

$$p(\theta|ent) = p_{ent}(\theta)p(\theta)/\int p_{ent}(\theta')p(\theta')d\theta'. \quad (2.2)$$

Here, $p(\theta)$ is the distribution of collisions, which we may assume to be uniform. Ambrose and Wasteneys [7] also report CIC is rare. By using static images from scanning-electron microscopy (which cannot detect CIC), Barton et al. [14] measure the distribution of entrained MTs, as in Ambrose and Wasteneys [7]. It is notable that the probability of CIC varies between measurements from insignificant to dominant. Modelling efforts, discussed below in Sec. 2.4, also disagree about the significance of CIC.

What is the biophysical basis of these collision resolutions? Because of continued hydrolysis of the GTP cap, a MT whose growth is stalled has an enhanced catastrophe frequency, providing a natural mechanism for CIC. This model is considered in Allard et al. [2] (Ch. 3), which finds that the probability of CIC is dependent on how densely MTs are anchored to the cortex. For the anchoring density measured in *Arabidopsis* roots, Allard et al. [2] (Ch. 3) predicts a catastrophe probability of roughly 10%, suggesting that the anchor density in Tobacco is lower. Entrainment is more complicated: After a MT is entrained by another, the MTs form a bundle most likely mediated by members of the MAP65 class of MAPs, which crosslink adjacent MTs together with a spacing of 20-30 nm [29]. Once bundled, MTs remain dynamic [120], although possibly with different polymerization properties [127]. Allard et al. [2] (Ch. 3) developed a model of entrainment based on an energetic competition between the chemical bonding energy of MAP65 and the MT bending stiffness. This model, again dependent on the manner in which MTs are anchored to the cortex, predicts a monotonically decreasing entrainment probability shown in Fig. 2.4E.

2.3.3 Nucleation and density

In the absence of an organizing centre, nucleation of new MTs occurs throughout the cortex. As in other eukaryotes, nucleation is mediated by the γ -tubulin ring complex (γ -TuRC) [100]. There is evidence that nucleation can occur in the absence of existing MTs [30, 134, 135], and also in a MT-dependent fashion where γ -TuRC is distributed along extant MTs. New MTs have been reported to branch off extant MTs at a specific angle of 40° from [100, 135], or parallel with [132], the extant MTs. Once a MT

2.3. Experimental data

is nucleated, one hypothesis is that the minus-end of the new MT remains statically associated with the γ -TuRC for a short time until it is severed by the MT severing protein katanin [100, 130]. Chan et al. [32] report that the nucleation is biased toward the plus-end of the extant MT, with no bias to either left or right sides.

MT-independent nucleation has been modelled by a spatially homogeneous nucleation rate, k_{nuc}^0 with units ($\mu\text{m}^{-2} \text{min}^{-1}$). MT-dependent nucleation is modelled by a nucleation angle, θ_{nuc} , in addition to a nucleation rate. Chemically, this rate constant is tri-molecular, thus the rate of new MTs is proportional to

$$[\text{tubulin}][\gamma\text{-TuRC}][\text{length of extant MTs}]. \quad (2.3)$$

Assuming constant growth velocities for MTs assumes the tubulin concentration is not rate-limiting in polymerization, and so such an assumption can be made here. There are two other simplifying possibilities: that γ -TuRC is rate-limiting, in which case the MT-dependent nucleation rate has units of min^{-1} , or that the extant MTs are rate-limiting, in which case the rate constant has units $\text{min}^{-1} \mu\text{m}^{-1}$, and the per-minute rate is also proportional to the total length of all MTs. The MT-dependent nucleation rate has been measured in *Arabidopsis* as $0.3 - 1.7$ per minute per $10^3 \mu\text{m}^2$ [32]. Nakamura and Hashimoto [101] measured the MT-dependent nucleation rates and report $\approx 2 \times 10^{-3} \text{ min}^{-1} \mu\text{m}^{-1}$, reported per micron of extant MT, and $\approx 2 \times 10^{-3} \text{ min}^{-1} \mu\text{m}^{-2}$, reported per square micron of cortex.

If other parameters are well-constrained, the nucleation rate can be back-engineered from the MT density. The nucleation rate and density have demonstrated key importance in models [3, 121, 126] and experimentally [136].

2.3.4 Severing at crossover

Once MTs have crossed over, they may become severed at the crossover point. Interestingly, the number of severing events at MT crossover points is high in MT arrays that organize, such as *Arabidopsis* petiole cells, while low in cells with disorganized arrays such as leaf pavement cells, with a ratio of roughly 4:1 [138]. Although severing is necessary for MT organization [23, 24], it is unclear whether severing at crossover (as opposed to severing immediately after nucleation) is necessary. This distinction between two classes of severing is easily achieved in computer simulation — thus, the inclusion of severing at crossover will be of interest. For this, the rate of severing, k_{cut} will need to be estimated. As with MT-dependent nucleation,

2.3. Experimental data

MT severing is a bimolecular reaction and can either be rate-limited by the concentration of crossover-severing agents (presumably katanin [138]), or is rate-limited by the number of crossovers. The action of katanin has been shown to be modulated by MT bending in fibroblasts [106], suggesting another possible class of severing events.

2.3.5 Cell geometry

From a theoretical point of view, CMTs can be simulated on an abstract plane with no boundaries, or with periodic boundary conditions. This allows for a theoretical understanding of how intrinsic MT dynamics and MT-MT interactions alone induce organization. However, real cells have faces with edges. An elongating root cell can be approximated as a cylinder [3, 48]. What happens to MTs incident upon the top and bottom edges? A basic assumption, adopted by Allard et al. [3] (Ch. 4) and Eren et al. [48], is that the edges induce catastrophe. Since then, edge-induced catastrophe has been observed and measured in leaf cells [9]. A more complete treatment of cell edges is presented in Ambrose et al. [9] (Ch. 5), discussed in Sec. 2.4.7.

2.3.6 Angle distribution, order parameter and dominant direction

The amount of order in the CMT array is a key feature to be addressed by models, and arguably the key property of real CMT arrays. It is described by the angular distribution, $p(\theta)$, or the length-weighted angular distribution $p_l(\theta)$ of CMTs. One or both of these angle distributions has been measured in *Arabidopsis* elongating root cells Ambrose and Wasteneys [7], Burk and Ye [24], Himmelsbach et al. [69], Nakamura and Hashimoto [101] and several other places along the root [67, 125]. The time evolution of the angle distribution, between 10 min – 240 min after cytokinesis, were recorded for Tobacco BY2 [45]. These last data measure EB1 comets rather than MTs directly, so they represent growing plus-ends.

It can be advantageous to describe orientational order with a single number (typically called an *order parameter*) rather than an entire distribution, for example to study the time course of order or how it varies with a given input parameter. For a population of N microtubules, each with orientation θ_i and length l_i , where $i = 1 \dots N$, the order parameter S can be defined in several ways; the classical order parameter for liquid crystals (see Appendix B) has $S = 0$ for a completely disordered state and $S = 1$ for a perfectly ordered state. Allard et al. [3], Baulin et al. [16], Tindemans et al.

2.3. Experimental data

[126] and Shi and Ma [121] define S in apparently different ways, but they are all equal (see Appendix B). Eren et al. [48] uses a parameter (referred to as entropy, E) that is zero for a perfectly array and 5.19 for a perfectly random array, also discussed in the appendix. The advantage of dominant direction and order parameter, rather than mean and standard deviation of $p(\theta)$, is primarily due to the periodic nature of angle distribution — a mean angle of $\theta = \pi/2$ could mean either MTs predominantly at $\theta = \pi/2$ or at $\theta = 0$.

Another key feature of CMT arrays is the time it takes for the array to self-organize from a particular initial condition. After drug-induced depolymerization, the array reforms within 120 min of the initiation of MT assembly [135]. After disruption of Phospholipase-D, which is required for MTs to be anchored to the cortex, anchoring returns within 30 min [42], although this increases substantially with temperature. As mentioned above, the time course for the angle distribution has been measured in Tobacco BY-2 cells [45], in which the system reaches a steady state within 100 minutes. Hypothesized mechanisms of organization must generate ordered arrays in the physiological timescales summarized here, providing another question models may address.

2.3.7 Mutants and other experimental perturbations

In addition to recapitulating the CMT arrays observed in WT plants, successful models must also reproduce the arrays in mutant systems and other experimental perturbations, described here.

MOR1 and MT dynamics

MOR1 is a MT-associated protein with the ability to alter several dynamic instability parameters, including increasing both shrinking and growing velocities. It is a homologue of XMAP215, which modifies all MT dynamics parameters in vitro [20] and can be explained at the dimer level [129]. Altering these parameters has a dramatic effect on the CMT array. The temperature-sensitive mutant *mor1-1* has an organized array at permissive temperature 21°C, while the dynamic instability parameters are modified significantly at 31°C and the MTs become short and disorganized [78, 136]. Simulations in Allard et al. [3] (Ch. 4) confirm that changes in the dynamic instability parameters are sufficient to explain the loss of organization.

2.3. Experimental data

CLASP, MT anchoring, edge effects

Strong association of CMTs to the cortex is essential for a properly organized array [7, 42]. Anchoring is believed to involve phospholipase-D [42] and the CLASP protein [7]. Inhibiting phospholipase-D results in total cortical detachment and loss of self-organization [42].

In the *clasp-1* mutant, where CLASP transcripts are not present, anchor density is decreased and the distance between anchors is increased [7] — the free, unanchored length at the plus-end of a growing MT appears to entrain more readily in these mutants, as the free end can explore more space and be entrained with less curvature. Furthermore, the *clasp-1* mutant’s array, measured in [7], is more highly ordered (that is, with fewer deviations from the dominant orientation) than the WT array. However, CLASP may have other roles in the cell other than modifying anchoring, discussed in Sec. 2.4.7.

Katanin

In the *fra2* mutant of AtKTN1, MT severing is inhibited, which delays [23] or inhibits entirely [24] MT organization. The angle distribution in *fra2* has been measured [24]. Overexpression of katanin destabilizes the MT array [122]. The *katanin* mutant results in disorganized array [101], for which the angle distribution has been reported.

Nucleation and helicity

Branch-form MT-dependent MT nucleation [32, 100] consistently occurs at around 40°. Two mutants of members of γ-TuRC modify this angle. The *spr3* mutant [101] perturbs the tightly controlled nucleation from $40 \pm 7^\circ$ in WT to $50 \pm 12^\circ$. This results in arrays that are organized with roughly the same order parameter, but a dominant direction 10° away from the transverse direction, resulting in a left-handed helical pattern [101]. The *amiR* mutant [81] has a decreased nucleation angle with a bimodal distribution peaked at 14° and 30° in pavement cells. Pavement cells typically produce MT arrays that are disorganized, but form more parallel arrays in the *amiR* mutant [81]. It will be important to measure the angle distribution in elongating root cells of *amiR*.

The nucleation mutants above are part of a larger class of mutants whose arrays are self-organized but with a dominant direction angled with respect to the transverse direction [72]. In the majority of these cases, the organ comprised of cells with helical CMT arrays are also twisted, but with opposite handedness, further evidence of the link between CMTs, cell wall

elongation and organ structure. Many of these mutants involve the auxin pathway. In these cases, what is the input that could generate helical output?

2.4 Mathematical models of CMT organization

2.4.1 Classes and aims of mathematical models

There are two questions that cell-scale models can help elucidate: (1) What input parameters, in particular MT dynamic parameters, collision resolution probabilities and nucleation rules, result in self-organization of the array, in a theoretical cell? And (2) of the input parameters that result in self-organization, which are actually the primary determinants of organization in plant cells? The answer to the second question will involve matching model outputs to mutants and other experimental perturbations.

Computer simulation, individual-based models and mean-field models

Modelling efforts to date can be classified into two overlapping and non-exhaustive classes: individual-based models and mean-field models. Individual-based models (also called rule-based or agent-based models), in which each MT or MT segment is represented as an individual, and rules for individual dynamics and interactions determine the evolution of the system. Computer simulation is used to find the patterns that result from these rules.

The other class represents the population of MTs as a density $p(x, y, \theta, l, t)$ at location (x, y) with orientation θ and length l . The dynamics are encoded in a partial differential equation (PDE) or integro-PDE, which describes how $p(x, y, \theta, l, t)$ changes in time. Because the density approach averages over a population of individual MTs, these models are called mean-field models [77]. Since the full, spatially-dependent equation is too cumbersome for analysis, researchers typically assume the MT array has approximately the homogeneous density at all locations, and use $p(\theta, l, t)$ instead. I elaborate on the spatial homogeneity assumption in Appendix A. In the study of coarsening systems such as liquid crystals (see Sec. 2.4) and other aggregation phenomena in biology [96, 98], mean-field methods have been greatly successful. However, questions remain regarding whether the spatial uniformity approximation is valid for extended bodies such as MTs, which act non-locally [16].

2.4. Mathematical models of CMT organization

The advantage of computer simulation of individual-based models [3, 16, 48, 121, 126] is that it accounts for stochasticity, can accommodate rules of almost unlimited complexity, and provides output that visually recapitulates microscopy images. However, it is computationally taxing (simulating a population of 10^3 MTs for a 10^3 min can take a day of computing time). Moreover, input parameters need to be fully specified and it is difficult to use the output from one set of input parameters to extrapolate the behaviour of another set of input parameters.

In this sense, the mean-field models can provide deeper insight. Their disadvantage is that they require drastic simplification of interaction rules, and simplifying assumptions such as the spatial-homogeneity assumption described above. The most powerful modelling occurs when computer simulation is combined with mean-field modelling, as in Tindemans et al. [126] and Shi and Ma [121].

2.4.2 Zumdieck et al. [143]: Liquid crystals

Early theoretical work on CMT organization [84, 143] built on the wealth of understanding of self-organization in liquid crystal systems. A liquid crystal [41] is a phase of molecules that are typically rod-like. At low temperatures, these molecules pack closely together, resulting in an array that has orientational order, even without bonds between the molecules. Thus, the system exhibits crystal properties (orientational order) as well as liquid properties (the absence of fixed molecular bonds). The concept of entropy in liquid crystals [108] may have implications for CMTs — there are many more ways to arrange N rods in a given volume if they are aligned, as opposed to if they are randomly ordered. Thus, neglecting energetics, the system is much more likely to be ordered. When liquid crystals display orientational order, they are referred to as *nematic*. A seminal result of statistical physics is that as temperature is decreased, liquid crystals transition from an isotropic phase to a nematic phase [41]. Liquid crystals are different from CMTs in that liquid crystals migrate by translation and rotation, as opposed to through treadmilling, and do not dynamically change in length. Zumdieck et al. [143] developed a model of CMT organization, assuming CMTs are mobile and diffusing in an overdamped fluid. Since then, evidence has accrued that that MTs are strongly anchored to the cortex and migrate predominantly by treadmilling [120]. The absence of this anchoring inhibits organization [42]. However, much current theoretical work makes use of the insight and vocabulary of nematic liquid crystals.

2.4.3 Dixit and Cyr [44]: Angle-dependent collision resolutions

In the pioneering paper that first emphasized the importance of angle-dependent collision outcomes, Dixit and Cyr [44] carried out simulations including collision-induced catastrophe (CIC) as well as plus-end entrainment (which they refer to as zippering). However, given the computational difficulty of the problem, the authors were only able to consider at most 20 MTs for 10 minutes, and a statistically meaningful interpretation is difficult to extract from their results. Further simulations by one of the authors in Eren et al. [48], discussed below, harnessed more powerful computational techniques.

2.4.4 Baulin et al. [16]: Oblique domains for simplified MT dynamics and collision-induced pausing

Baulin et al. [16] simulated a simplified model in which MTs were represented with a single state: their plus-end grows at a constant velocity, while their minus-end shrinks at a (slower) velocity. This single-state model of a MT is a limit of the two-state model [3]. Collisions resulted in the incident plus-end pausing until either the barrier had moved out of its way, or the incident MT's minus-end has depolymerized it completely, independent of angle. The authors found order emerged in oblique domains. A key contribution of Baulin et al. [16] was that even small external biases in interactions can tune the dominant direction of the resulting array. Baulin et al. [16] also developed a mean-field theory, however it was unable to capture the behaviour of even their simplified model. They hypothesize the inconsistency is due to the mean-field assumption of spatial homogeneity, that is, “disagreement is mainly due to the impossibility for a two-dimensional system to be at the same time considered as anisotropic and homogeneous.”

2.4.5 Tindemans et al. [126]: Mean-field analysis and simulation

The first mean-field model to capture angle-dependent collision resolutions, including both collision-induced catastrophe and entrainment, was developed by the group of Mulder [65, 126]. MTs were represented by the two-state model, and nucleation was assumed to occur uniformly in space, independent of existing MTs. The mean-field model made two major contributions. First, that the MT dynamics parameters only affect organization

2.4. Mathematical models of CMT organization

through the function

$$G = \left(\frac{2v_g^p v_s^p}{k_0(v_s^p + v_g^p)} \right)^{1/3} \frac{v_g^p f_{cat} - v_s^p f_{res}}{v_s^p v_g^p} \quad (2.4)$$

meaning two sets of MT dynamics parameters with the same G have identical self-organization properties. G depends on the nucleation rate k_0 , which must be large enough to ensure high MT densities so that collisions occur frequently. Second, a critical value of G (a *bifurcation point*), called G^* , was found, where if $G < G^*$, the system exhibits no organization¹. Remarkably, the bifurcation point depends only on the probability of catastrophe, $p_{cat}(\theta)$, and not at all on entrainment. Further, as long as $p_{cat} > 0$ for some θ , the bifurcation point is invariant to, for example, halving or doubling p_{cat} . In their mean-field theory, if a system does self-organize, the degree to which it orders in steady state (its S -value) depends on the magnitude of p_{cat} , as well as entrainment. This predicts that in the absence of collision-induced catastrophe, entrainment alone cannot give rise to self-organization.

The authors also carried out computer simulation, which, for simplified collision resolution probabilities, was found to agree with their mean-field theory. This suggests the spatial homogeneity assumption is appropriate, in contrast to the conclusions of Baulin et al. [16]. However, they did not simulate entrainment probabilities that decrease monotonically with angle, as observed experimentally [44] and were found to be sufficient for self-organization in other computer simulations [3, 48].

How does the parameter G^* relate to piece-wise constant collision resolution probabilities used in [3, 48, 121]? If catastrophe occurs independent of angle with probability p_{cat} , then $G^* = (p_{cat}/3)^{1/3} > 0$, in which case the authors find that for any nucleation rate and any $p_{cat} > 0$, order will never emerge, in contrast to the findings of Baulin et al. [16], Allard et al. [3] (Ch. 4) and Shi and Ma [121].

2.4.6 Allard et al. [3] (Ch. 4): Simulation matching mutants

Computer simulations using two-state and three-state models, with collision resolution probabilities considering both angle-dependent collision-induced

¹The bifurcation point depends on the function $p_{cat}(\theta)$ by

$$G^* = (2\hat{c}_2)^{1/3} \left(\frac{\hat{c}_0}{2\hat{c}_2} + 1 \right) \quad (2.5)$$

where \hat{c}_0, \hat{c}_2 are the first two Fourier coefficients of the function $p_{cat}(\theta)|\sin \theta|$.

2.4. Mathematical models of CMT organization

catastrophe and angle-dependent entrainment, were carried out by Allard et al. [3] (Ch. 4). This study found that entrainment alone was sufficient for self-organization, with or without collision-induced catastrophe, while collision-induced catastrophe alone is insufficient when using physiological parameters from [44, 78, 120]. For uniform nucleation, the rate was taken that produced a steady-state MT density comparable to experiment, as described in Sec. 2.3.3. For collision resolutions, Allard et al. [3] (Ch. 4) assumed that above a critical angle θ_{ent} , collision-induced catastrophe occurs with probability p_{cat} , while below, entrainment occurs with probability p_{ent} . Thus all details of the functions $p_{cat}(\theta)$ and $p_{end}(\theta)$ are reduced to three parameters $(p_{cat}, \theta_{ent}, p_{ent})$. This study found that $(\theta_{ent} = 0.7 \text{ rad}, p_{ent} = 0.9)$ produced self-organization, while $\theta_{ent} = 0 \text{ rad}, p_{ent} = 0$) failed to self-organize for any p_{cat} .

Allard et al. [3] (Ch. 4) also simulated MT-dependent branched nucleation. In the absence of uniform nucleation, this produced arrays that were sparse, suggesting that MT-dependent nucleation cannot be the only nucleation pathway.

The biological relevance of Allard et al. [3] (Ch. 4) was explored by using input parameters from the *mor1-1* and *clasp-1* mutants. In the *mor1-1* case, the simulations recapitulated the loss of self-organization as the MT dynamic parameters were changed. In the case of *clasp-1*, which modified the entrainment probabilities, the simulation did not recapitulate the slight increase in ordering. The primary role of MOR1 as a modifier of MT dynamic parameters is well-supported by its homologues both in other *in vivo* systems and biophysically [129], while the primary role of CLASP may not be to modify the entrainment probabilities. Further studies of CLASP have generated a new hypothesis for its primary role, described in the next section.

2.4.7 Ambrose et al. [9] (Ch. 5): Dynamics on polyhedral cells

Insight into the effects of cell edges comes from a recent study by Ambrose et al. [9] (Ch. 5), in which the CLASP protein was found to preferentially localize to specific cell edges at different points in a cell's development. Evidence suggests that CMTs suffer edge-induced catastrophe at sufficiently high-curvature edges, and that CLASP allows CMTs to bypass edges wherever it localizes.

Including this in the computer simulations of Allard et al. [3] (Ch. 4), we found that modulating the probability of edge-induced catastrophe produces

2.4. Mathematical models of CMT organization

arrays that are either transverse, longitudinal or mixed. One limitation of the simulations is that the probability of edge-induced catastrophe used were taken from experimental measurements in leaf pavement cells as opposed to root cells, which exhibit the arrays being simulated.

2.4.8 Eren et al. [48]: Dynamics on cylindrical cells

Eren et al. [48] performed computer simulations of MTs on the surface of cylinders. In agreement with Allard et al. [3] (Ch. 4), they found entrainment sufficient, with or without CIC, and CIC to be insufficient to generate an ordered array. Simulations of the *mor1-1* MT dynamic instability parameters resulted in loss of self-organization. When they increase the critical entrainment angle to $\theta_{ent} = 60^\circ$, self-organization was slightly reduced as in Allard et al. [3] (Ch. 4).

A novel aspect of Eren et al. [48] are attempts to address the helical arrays observed experimentally. Catastrophe-inducing top and bottom edges promote a transverse array with no polarity — approximately equal number of MTs pointed in the dominant direction as were antiparallel to it. They found that a mixture of branch-form and background nucleation leads to an array with polarity, although the direction of polarity was found to be random. If the branch-form is biased towards either the right or left of the extant (mother) MT, the dominant direction depends on the initial conditions: *de novo*, the arrays became helical but with randomly either left- or right-handedness, whereas from an initially transverse, polarized array, the result is emergence of right- or left-handedness, depending on the direction of initial polarity and the nucleation bias.

2.4.9 Shi and Ma [121]: Catastrophe in a simplified MT model

Shi and Ma [121] developed a computer simulation and mean-field theory for organization. Instead of the Dogetrom-Leibler models, they use the linear dimer-level model of Flyvbjerg et al. [50]. Collisions result in the inability to polymerize, which soon result in catastrophe unless the barrier MT depolymerizes out of the way. This is approximately equivalent to collision resolution probabilities with $p_{cat}(\theta) = 1$.

Shi and Ma [121] find that, as the polymerization rate and MT density are varied, the system exhibits three phases: isotropic (disorganized), a highly nematic (ordered) and less nematic phases. Their mean-field model also demonstrates three phases. In contrast to Tindemans et al. [126], as

2.5. Outlook: Branching of new questions from existing ones

parameters are varied slowly, the order parameter can either increase gradually, or suddenly and irreversibly. Irreversibility as an input parameter is varied is known as *bistability* since it corresponds to two (or more) stable steady states existing for the same set of input parameters.

2.5 Outlook: Branching of new questions from existing ones

The most striking open question emerging from the modelling literature concerns the significance of the two dominant collision resolutions: collision-induced catastrophe and entrainment. The question of the significance of CIC is duplicated by the two primary questions of mathematical modelling described in Sec. 2.4.1 (What is required theoretically to self-organize? And which of these possibilities is exploited by real plants?). There are thus four possibilities.

1. If CIC is the dominant promoter of organization, as suggested by the results of Tindemans et al. [126], then either
 - (a) experimental measurements of CIC in *Arabidopsis* underestimate CIC, or,
 - (b) CIC is indeed rare and an as-yet-unidentified factor is promoting organization. The unidentified factor could be MT severing [138] or edge interactions [9, 48].
2. If entrainment is the dominant promoter of organization, as suggested by the results of Allard et al. [3] (Ch. 4) and Eren et al. [48], and
 - (a) entrainment alone is sufficient and experimentally observed, as reported, then theory and experiment are in agreement and further models will be modifications of this base model.
 - (b) The fourth possibility is that entrainment is theoretically sufficient and CIC is not, but entrainment is found to be biologically unnecessary. At this point, novel hypotheses for organization will need to be invoked.

To distinguish between possibilities (1) and (2), further computer simulations need to be carried out to bridge the gap between disagreeing simulations. Also, experiments need to be carried out to further constrain the parameters such as nucleation rates. In either case (1) or (2), to distinguish between (a) and (b), the most direct experiments would turn on and

2.5. Outlook: Branching of new questions from existing ones

off entrainment and CIC independently, possibly by controlling MAP65 (to perturb entrainment) and GTP hydrolysis (to perturb CIC). Such experiments are riddled with difficulty.

It is possible that disagreement can be explained by the bistability observed in Shi and Ma [121]. The mean-field work of Tindemans et al. [126] does not preclude the existence of a self-organized steady-state with entrainment alone, but only that it cannot be generated from a perfectly homogeneous, isotropic initial state. It could be that the random fluctuations of a finite number of MTs effectively mean that plants and computer simulations do not start from a homogeneous, isotropic initial state. It could also be that some other element causes an initial anisotropy, which is exploited by entrainment to further align the array.

The ultimate validation of models lies in recapitulating phenomena, including mutants and experimental perturbations. This has been accomplished for the *mor1-1* [3] mutant, *fra2* mutant [48] and *clasp-1* mutant [9], and remains to be accomplished for *spr1* and γ -tubulin mutants *amiR* and *spr3*. However, once validated, the ultimate goal of models is to generate novel predictions. These new predictions represent new hypothesis and can spur new experiment and theory. For example, Eren et al. [48] have identified three inputs that result in helical arrays. Experiment must now be used to identify which is used by nature.

Chapter 3

Biophysical basis of cortical microtubule interactions²

3.1 Introduction

Two scales of questions about CMT self-organization remain to be elucidated. First are cell-level questions: How do molecular interactions between MTs give rise to cell-scale order? How do changes in the molecular interactions affect self-organization? This aspect has received recent attention Allard et al. [3] (Ch. 4), [16, 44, 126, 143]. These models have assumed phenomenological descriptions of MT-MT interaction. A second scale of questions is molecular: how do interactions such as entrainment and collision-induced catastrophe occur? Why do they occur at different frequencies for different collision angles? How are MTs held to the cortex and how does this anchoring affect MT-MT interactions?

In this chapter, I present a mechanochemical model of CMTs to address the latter questions. The first section introduces a kinetic model for MT anchoring to the cortex, which allows us to infer chemical rate constants from experimentally measured free lengths. This model is used in subsequent sections of MT-MT interactions. The second section introduces mechanical models for collision-induced catastrophe, crossover and plus-end entrainment. For collision-induced catastrophe, a dimer-level model leads to an estimate of its probability, P_{cat} . For crossover we present an energetic model independent of details of the crossover pathway. For entrainment, we present an energetic model as well as a dynamic (torque-based) model. In the final section we use the energetic models of crossover and entrainment in an adiabatic approximation to compute probabilities for these collision resolutions. Through these models, entrainment is explained by a competition between crosslinkers, which tend to bundle adjacent MTs, and the

²A modified version of this chapter has been published in Allard, Ambrose, Wasteneys and Cytrynbaum, “A mechanochemical model explains interactions between cortical microtubules in plants”, Biophysical Journal 99 p.1082, 2010 (see bibliography [2]). The introduction has been shortened here.

3.2. MT-cortex anchoring

bending stiffness of the incident MT, which opposes entrainment. We find this energetic competition is sufficient to explain the angle-dependence of entrainment and crossover.

3.2 MT-cortex anchoring

While the molecular identity of the anchor linking MTs to the cortex is unknown, the process involves phospholipase-D [42, 53] and the CLASP protein [7]. One or both of these may form the physical anchor. MTs in CLASP null mutants remain attached to the membrane, although with longer free ends [7]. Here, we refer to the physical anchor without speculation regarding its components. As a MT grows, the anchor protein chemically attaches and detaches along its length. If the MT were a long, stationary rod adjacent to the membrane, and anchors attached with rate constant k_{on} (with units $\mu\text{m}^{-1} \text{min}^{-1}$) and detached with rate k_{off} (in min^{-1}), then the density of attachments, $a(x, t)$, would be governed by the equation

$$\partial a / \partial t = k_{\text{on}} - k_{\text{off}} a. \quad (3.1)$$

Here we assume that the binding rate k_{on} is uniform along the length of the filament. In reality, the free plus-end can fluctuate away from the membrane, in principle reducing k_{on} near the tip compared to near the anchored regions, where the filament is always close to the membrane. However two facts suggest that nonuniformity of k_{on} is insignificant. First, the persistence length of a MT is millimeters, whereas the free length is typically $3 \mu\text{m}$, so thermal undulations are small. Second, below we estimate $k_{\text{on}} \sim 0.3 \text{ min}^{-1} \mu\text{m}^{-1}$, suggesting that anchor attachment is reaction-limited as opposed to diffusion limited, thus fluctuation of the filament is not the bottleneck. Note that the anchor kinetics may be different tens of microns behind the plus-end, where the MT is older and other MAPs may act. Our model is only concerned with anchors near the plus-end. Consistent with this, the data we use below to estimate the kinetic rates only incorporates anchor spacings at the tip of the MT.

In steady-state, the density of anchors is $a = k_{\text{on}}/k_{\text{off}} \equiv a_c$. This density corresponds to a spatial Poisson process [115], and the distance between anchors, L , would have cumulative probability distribution $G(l) = 1 - \exp(-a_c l)$ (that is, $G(l)$ is the probability that $L < l$). Thus, free lengths would be exponentially distributed. However, if the plus-end of the MT is growing at constant velocity v_g^p , then the density of anchors is lower near its growing tip, since this region of MT has not been present for as

3.2. MT-cortex anchoring

long as the region further back. The anchor density is governed by same differential equation, Eq. 3.1, but with boundary condition $a(v_g^p t, t) = 0$. The solution is $a(x, t) = a_c(1 - e^{-k_{\text{off}}(t-x/v_g^p)})$ or, as measured a distance $l = x - v_g^p t$ from the growing tip, $a(l) = a_c(1 - e^{-\lambda l})$ where $\lambda \equiv k_{\text{off}}/v_g^p$. This varying density gives rise to a non-homogeneous Poisson process [115], and the distance between the growing tip and the first anchor, L , is a random variable with cumulative density

$$P(L < l) = G(l) = 1 - \exp\left(-\int_0^l a(l') dl'\right). \quad (3.2)$$

The probability density, $g(l)$, is found by differentiating Eq. 3.2. There are two competing length scales, the mean spacing in absence of growth, a_c^{-1} and the length of growth before detachment, λ^{-1} .

The free length distribution has been experimentally measured by Ambrose and Wasteneys [7] in both WT cells and the *clasp-1* mutant and is shown in Fig. 3.1. We estimate a_c and λ in the probability density by fitting Eq. 3.2 to the data using the method of maximum likelihood and a bootstrap. The fit is shown in Fig. 3.1. Note that the exponential distribution predicted by the stationary model would not reproduce the nonzero maximum seen in the experimental data, while the model including growth does. Furthermore, given $v_g^p = 3.5 \mu\text{m}/\text{min}$ [78], we can back-engineer the kinetic rate constants near the tip. These are shown in Table 3.1.

The small detachment rate predicts that once an anchor has attached, it will be, on average, weeks before it detaches — anchoring appears to be an effectively irreversible process. However, near the tip, the density of anchors is limited not by dissociation but by the growth of the MT tip. Further back, the anchor density will be limited by MT catastrophe. Note we are modelling growing MTs only, and the experimentally observed free lengths are from growing MTs, thus the rates in Table 3.1 are only relevant while the MT is in the growing state.

	k_{on} ($\text{min}^{-1} \mu\text{m}^{-1}$)	k_{off} (min^{-1})
WT	0.34 ± 0.13	$(5.5 \pm 1.3) \times 10^{-5}$
<i>clasp-1</i>	0.16 ± 0.08	$(4.5 \pm 1.0) \times 10^{-5}$

Table 3.1: Chemical kinetic rate constant for the anchor protein in WT and *clasp-1* mutants.

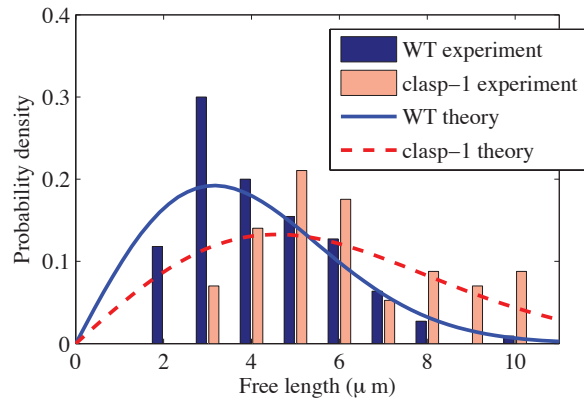


Figure 3.1: The free lengths L from the MT tip to the last anchoring site. Experimental data from Ambrose and Wasteneys [7]. The nonhomogeneous distribution predicted by Eq. 3.2 provides qualitative agreement for both WT and *clasp-1* data.

3.3 MT-MT interactions

In this section, we consider the interaction between two MTs after collision, in which the growing plus-end of an “incident” MT collides along the length of a “barrier” MT. There are several possible resolutions to a collision. The incident MT may switch to the shrinking state, which we refer to as collision-induced catastrophe. It may cross over the barrier MT and continue growing, [64] or it may become entrained. We consider these three resolutions, depicted in Fig. 3.2, neglecting other possible resolutions, such as buckling before the barrier or becoming severed at the crossover point [138].

In the following, we assume the incident MT is colliding with the barrier at collision angle $\theta \in [0, \pi/2]$ where $\theta = 0$ for parallel MTs and we ignore the polarity of the barrier MT. The distance from the collision site to the closest anchor on the incident MT is L .

The remainder of the paper is organized as follows. Anchoring and catastrophe are slow processes and effectively irreversible but mechanical relaxation and MAP crosslinking are fast and reversible. When a collision occurs, it is resolved as soon as an anchor attaches, either on the distal side of the target or in an entrained configuration, or if the incident MT catastrophes. The catastrophe probability is described by a dimer-level model we describe in the next section.

We then consider the conditional probabilities of crossover and entrainment, given no catastrophe occurred during the collision (either “natural” catastrophes or collision-induced catastrophes). The incident MT has a large configuration space to explore thermally, including some configurations where its tip is far from the membrane, some where it is crossed over the barrier and close to the membrane, and finally, configurations where it is entrained by the barrier MT. Assuming these are explored in quasi-equilibrium, at the moment of anchoring, the probabilities of being in a crossover configuration or an entrained configuration only depend upon the energies of those states. Therefore, we compute the energy of crossover configurations, and the energy of entrained configurations. To be certain that the entrained configurations are indeed explored in quasi-equilibrium, we present a mechanistic (torque-based) model of entrainment describing how an incident MT is progressively entrained by a barrier MT and the action of crosslinking MAPs. In the final section, we use the crossover and entrainment state energies to compute overall angle-dependent probabilities of entrainment and crossover.

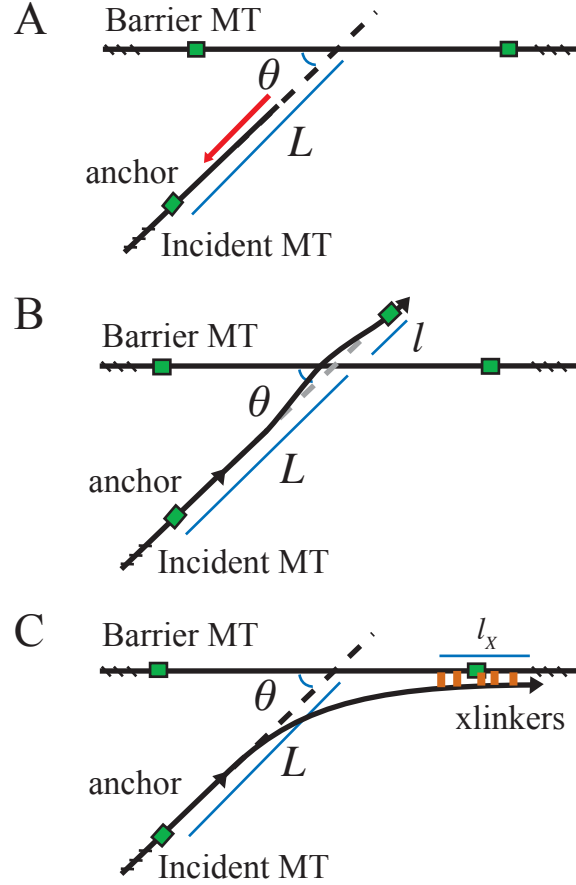


Figure 3.2: Three possible collision resolutions. The incident MT collides with a barrier at an angle θ and with free length L . Possible resolutions are (A) catastrophe, in which the incident MT begins shrinking, (B) crossover, in which the incident MT develops a small bend to overpass the barrier and continue growing unperturbed, and (C) plus-end entrainment, in which the incident MT becomes entrained by the barrier via crosslinking proteins (orange online). MTs are shown in black, while anchors are shown as green squares.

3.3.1 Collision-induced catastrophe

Catastrophe is the spontaneous switch of the MT plus-end from a state in which growth dominates, to a state in which shrinkage dominates, due to

3.3. MT-MT interactions

the loss of the polymerization-promoting GTP-tubulin cap. VanBuren et al. [128] developed a model for MT polymerization and catastrophe at the dimer level. In this model, dimers associate at a rate k_+^0 and dissociate at a rate $k_- = k_+^0 \exp(-\Delta G/k_B T)$ where ΔG is the energy required to remove the dimer from the MT lattice. This energy is different for GTP-tubulin dimers, which favour growth, and GDP-tubulin dimers, which favour disassembly. Newly associated dimers are GTP-tubulin, and they switch to GDP-tubulin through GTP hydrolysis at rate k_{hyd} .

We fit the bond energies and hydrolysis rate parameters in the model of VanBuren et al. [128] to the growth rate, shrinkage rate and catastrophe rate of Arabidopsis at 31C from Kawamura and Wasteneys [78] and found parameters listed in Table 3.2. These parameters are comparable to the parameters reported in VanBuren et al. [128]. We modify the model to consider collision with a barrier MT as follows. A growing MT that encounters a barrier will have the same k_{hyd} and k_- , but for protofilaments in contact with the barrier, k_+ will be modulated by a prefactor α , that is, $k_+ = \alpha k_+^0$. We compute α as follows. When the incident MT encounters the barrier, its tip is undergoing thermal fluctuations and is a distance ρ away from its equilibrium position. Its energy, $E_{jump}(\rho)$, is the minimum of the linear elastic rod energy,

$$E = \frac{B}{2} \int_0^L \kappa(s)^2 ds \quad (3.3)$$

where B is the bending modulus of a MT, L is the MT's free length, $\kappa(s)$ is the curvature, and arclength s of the incident MT is measured from the last anchor. For small deformation, $\kappa(s) \approx y''(x)$ where y is the height of the MT above the membrane and x is distance along the membrane. From this we obtain the familiar beam equation $y^{(iv)}(x) = 0$ for $x \in (0, L)$, where L is the distance from the anchor to the barrier and we measure from the anchor. We use boundary conditions $y(0) = y'(0) = 0$, $y''(L) = 0$ and $y(L) = \rho$ and find $E_{jump}(\rho, L) = 6B\rho^2/(25L^3)$. The prefactor α , which depends on L , is the probability that thermal fluctuations allow the incident MT tip to clear the barrier, allowing the addition of a subunit, as opposed to subunit addition being blocked by the barrier (see Fig. 3.3A). We compute the fraction

$$\alpha(L) = \frac{\iint_{clear} e^{-E_{jump}/k_B T} dA}{\iint_{clear} e^{-E_{jump}/k_B T} dA + \iint_{block} e^{-E_{jump}/k_B T} dA} \quad (3.4)$$

where the “block” region is $0 < y < d$ and the “clear” region is $y > d$, both regions with infinite width in the direction parallel to the barrier, ρ is the radial coordinate and d is the diameter of a MT. In choosing to integrate

3.3. MT-MT interactions

over the tip's location only, we implicitly ignore higher modes of bending in the free length of the MT. These higher modes have energies that increase quadratically with mode number. This means the probability of accessing the same tip deflection through, for example, the third mode (only odd modes result in tip deflection) has probability $\exp(-3^2) \approx 10^{-4}$. The first mode reproduces the behaviour of interest. Buckling of the MT is irrelevant here, since the MT may relax by surpassing the barrier.

Parameter	Value
k_+^0 ($s^{-1} \mu\text{m}^{-1}$)	4
c (μM)	5
ΔG_{Lat} ($k_B T$)	10
ΔG_{Long}^* ($k_B T$)	6.8
ΔG_{kink} ($k_B T$)	6
k_{hyd} (s^{-1})	1.3

Table 3.2: Parameters used in the dimer-level model modified from VanBuren et al. [128].

For $\alpha = 1$ (no barrier), we simulate MT growth in this way 1000 times and observe that the probability of still being in the growth state P_g decays exponentially as a function of space. That is, fitting to $\partial P_g / \partial x = -r(x)P_g$, we find a constant $r(x) = r_0$. The catastrophe rate is $f_{\text{cat}} = r(x)\bar{v}_g^p = 0.2 \text{ min}^{-1}$ by construction. If $\alpha \ll 1$, P_g exhibits a rapid drop near the barrier, shown in Fig. 3.3B, which corresponds to a temporary increase in catastrophe rate near the barrier. The width of the drop represents MTs that either impact the barrier, and depolymerize GTP dimers before undergoing catastrophe, or MTs that overcome the barrier, but have a “weakened” GTP-cap, and thus undergo a collision-induced catastrophe beyond the collision site. As $\alpha \rightarrow 0$, the $r(x)$ resembles a delta function. The width of the drop depends on how the precise time of catastrophe is defined. As in VanBuren et al. [128], we use the moment when the MT has lost its entire GTP cap, after which we find the MT always enters the shrinking state. To compute a catastrophe probability independent of the arbitrarily-defined beginning and end of the collision, we plot P_g on a log-linear plot and take the drop, $P_{\text{cat}}(\alpha)$, to be the difference in y -intercepts of the line before and after the collision site, as shown in Fig. 3.3B. Note this quantity is distinct to the experimentally measured probabilities of catastrophe [44, 138], which may include spontaneous catastrophes. Using the relationship

3.3. MT-MT interactions

between α and L from Eq. 3.4, we compute the probability of collision-induced catastrophe as a function of the free length L . Convoluting this with the anchoring model $P_{cat} = \int_0^\infty P_{cat}(L)g(L)dL$, we find $P_{cat} = 0.03$ for WT *Arabidopsis*. A low probability agrees with experiments on petiole cells of *Arabidopsis* where the probability of catastrophe during a steep collision is 9% [138]. However, a study of Tobacco BY-2 cells [44] reported collision-induced catastrophe in up to 50% of collisions. Interpreting this in light of our model, it suggests differences in anchoring properties between cell lines: Denser anchors would disfavour crossover and entrainment, favouring catastrophe. As a demonstration of this concept, increasing the anchor attachment rate k_{on} to ten times the value we found for *Arabidopsis*, lead to a mean length of $1.2\ \mu\text{m}$, a third of WT. This tighter anchoring leads to $P_{cat} = 0.47$, roughly in agreement with Dixit and Cyr [44].

In our model, dimer addition at any protofilament requires the entire MT tip to fluctuate above the barrier. In reality, heterogeneity in the way each protofilament confronts the barrier may lead to the incident MT getting stuck near the cortex, or partially or entirely above the barrier. These effects are neglected in our model. We also assume all protofilaments encounter the barrier at the same depth in the lattice, which neglects the cylindrical shape of the barrier as well as the slight offset of protofilaments in a B-lattice [128]. To test the sensitivity on the latter assumption, we ran simulations in which protofilaments encountered the barrier at different depths and found the effect to be weak. A more detailed model of protofilament and barrier geometry may explain the strong angle-dependence observed experimentally in Dixit and Cyr [44], but would be computationally taxing.

3.3.2 Crossover

For crossover, the MT must bend to surpass the barrier. Note that in many eukaryotic cells, the fluid membrane may undulate, allowing a hypothetical MT to crossover without bending. In the plant case, turgor pressure and the stiff cell wall, with a Young's modulus of several hundred pN/nm² [33], render membrane undulations insignificant. The configuration of the incident MT is determined by minimizing the linear elastic rod energy, similar to Eq. 3.3, except with $x \in (-L, 0) \cup (0, l)$ and boundary conditions $y(-L) = y'(-L) = y(l) = y'(l) = 0$, and $y(0) = d$ where d is the diameter of a MT. We find the energy associated with crossover to be

$$E_{cross}(l, L) = \frac{3Bd^2(L + l)^3}{L^3l^3}. \quad (3.5)$$

3.3. MT-MT interactions

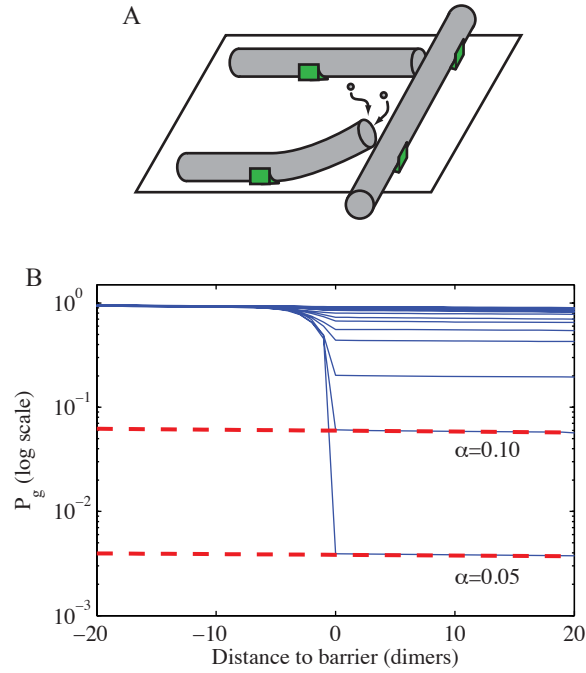


Figure 3.3: Collision-induced catastrophe. (A) Two MTs approaches a barrier MT. Thermal fluctuations at their tips allows it to either clear the barrier (bottom incident MT), otherwise it is temporarily blocked (top incident MT). Anchors are shown as green boxes. (B) Probability of being in the growth stage, i.e., that catastrophe has not yet occurred, versus distance to the barrier MT, for various values of α (log-linear scale). The drop between the pre-barrier curve and the post-barrier curves (shown as dashed lines for some α) provides the probability of collision-induced catastrophe.

3.3. MT-MT interactions

Note that there are many pathways to this final state, some of which involve prolonged contact between the barrier and incident MT [138]. However, energetically, the final state of these distinct pathways is assumed to be the same.

3.3.3 Plus-end entrainment

While plus-end entrainment (commonly called “zippering”) has been reported frequently [7, 44, 120], its molecular mechanism remains unclear. After a MT is entrained by another, the MTs form a bundle most likely mediated by members of the MAP65 class of MAPs, which crosslink adjacent MTs together with a spacing of 20 – 30 nm [29]. Once bundled, MTs remain dynamic [120], although possibly with different polymerization properties [127]. In our model, depicted in Fig. 3.2C, we refer to a crosslinker protein that preferentially bundles adjacent MTs with a rest length of l_0 between MTs, and a spacing of δ between adjacent crosslinkers. The chemical bonding energy gained by the crosslinker associating with two MTs is μ_X . The crosslinker is stiff, with a Hookean spring stiffness of $k_X \sim 10^{-2}$ pN/nm [36].

In this section, we present a model for how an incident MT can be progressively bundled into a parallel orientation with the barrier MT, as subsequent crosslinkers provide a torque reorienting its plus-end. Its final configuration will minimize the energy

$$E_{ME} = \frac{B}{2} \int_0^{l+L} \kappa(s)^2 ds + \frac{k_X}{2\delta} \int_0^{l_X} y(s)^2 ds. \quad (3.6)$$

where y is the distance from the incident MT to the barrier MT, l_X is the length of incident MT that is crosslinked, so $n_X \equiv l_X/\delta$ is the number of associated crosslinkers. In this case, it is convenient to measure arclength s of the incident MT back from its plus-end. On the length scale of interest, L , Eq. 3.6 can be nondimensionalized to

$$\tilde{E} = \int_0^1 (\tilde{y}''(\tilde{x}))^2 d\tilde{x} + K \int_0^r \tilde{y}^2 d\tilde{x} \quad (3.7)$$

where $r = l_X/L$ and $K = (k_X L^4)/(\delta B) \approx 10^3$ using the parameters in Table 3.3. The mechanical energy in the crosslinked region is $1/K$ relative to the energy in the MT bending energy, so in the region of MT that is crosslinked, deflection is insignificant. Thus we restrict our treatment to the uncrosslinked region. For small collision angles, the minimal energy is

3.3. MT-MT interactions

$E_{ME} = 2B\theta^2(l^{*2} + 3l^*L + 3L^2)/l^{*3}$ where $l^* = L + l - l_X$. For larger collision angles, we minimize Eq. 3.6 numerically.

Parameter	Meaning	Value	Reference
Parameters used in computing entrainment probability			
B	Bending modulus of MT	$3 - 20 \times 10^6 \text{ pN nm}^2$	[129]
d	Width of MT	25 nm	[29]
δ	Mean spacing between crosslinkers	35 nm	[29]
μ_X	Chemical bonding energy of crosslinker	$14k_B T$	[137]
v_g^p	MT growth velocity	$3.5 \mu\text{m}/\text{min}$	[78]
Other parameters			
f_{cat}	Free-space catastrophe rate	0.2 min^{-1}	[78]
l_0	Mean spacing between crosslinked MTs	35 nm	[29]
k_X	Crosslinker spring constant	$10^{-3} - 10^{-2} \text{ pN/nm}$	[36]

Table 3.3: Parameters used in the biophysical model of MT-MT interactions. The chemical bonding energy of a crosslinker is calculated from the dissociation constant K_d measured in tobacco MAP65-1b by Wicker-Planquart et al. [137] using $\mu_X = k_B T \ln K_d$ [66].

3.3. MT-MT interactions

In addition to the mechanical energy, E_{ME} , of the bent MT and stretched crosslinkers, there is also the chemical bonding energy of the crosslinkers, $-\mu_X n_X = -\mu_X l_X / \delta$, which acts favorably (negatively). The energy associated with entrainment is thus

$$E_{ent}(l, L, n_X) = E_{ME}(l, L, n_X) - \mu_X n_X. \quad (3.8)$$

The energy in Eq. 3.8 describes the final state of an entrained MT, without mentioning the pathway through which it arrived there. As mentioned above, the adiabatic approach we use in the next section to compute the probability of entrainment is independent of the details of the pathway, provided that such a pathway exists and that there are no energetic barriers preventing entrainment. Here, we describe a possible mechanistic model for entrainment via torque provided by crosslinkers to demonstrate a pathway free of energetic barriers to the entrained state. This model is similar to the model of actin bundling proposed in Yang et al. [141].

The mechanistic model below is presented as follows. The incident MT tip has an initial deflection making its angle at the collision site θ_X (which is distinct from θ , the angle between the undeflected portion of the incident MT and the barrier MT, see Fig. 3.4). We compute the torque τ with which the bending rigidity of the MT resists entrainment. We then compute the torque τ_X with which putative crosslinkers promote further entrainment. If $\tau_X > \tau$, then θ_X decreases. If $\theta_X = 0$ is an attractive steady-state of this process, the MT becomes entrained.

Suppose the straight, anchored section of an incident MT makes an angle θ with a barrier MT, while its free length bends slightly, so that the angle between the two MTs at the collision site is θ_X , as shown in Fig. 3.4. The MT acquires an initial deflection before the first crosslinker attaches. Here we assume this initial deflection is due to thermal fluctuations, under which the average tip deflection and tip angle [71] are

$$y_0 = 0.57 \sqrt{L^3/L_p}, \quad (3.9)$$

$$\tan(\theta - \theta_X) = 1.90 \sqrt{L/L_p} \quad (3.10)$$

where $L_p = B/k_B T$ is the persistence length of a MT. Cytoplasmic streaming [120] may further promote initial deflection, so our assumption in this section is an underestimate.

At the collision site, the incident free end is subject to torque τ , caused by crosslinkers elaborated upon below. The MT's shape is described by the beam equation with boundary conditions $y(L) = y'(L) = 0$, $y'(0) =$

3.3. MT-MT interactions

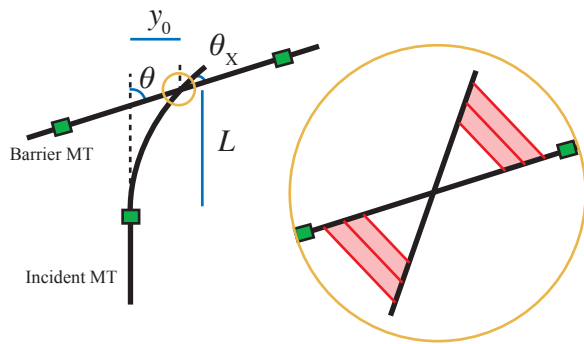


Figure 3.4: A mechanical pathway to entrainment. An incident MT encounters a barrier MT at an approach angle θ . The incident MT is slightly bent due to thermal fluctuations and, at the point of intersection, makes an angle θ_X with the barrier MT. (Inset) Crosslinkers (red online) attach two intersecting MTs. The crosslinkers vary in length, $l_i \in [l_0, l_M]$ and are spaced δ apart. Distance along the bisector to the i th crosslinker is x_i .

3.3. MT-MT interactions

$\tan(\theta - \theta_X)$ and $y''(0) = \tau/B$. We find the relationship between the tip deflection y_0 , crosslinker torque and intersection angle,

$$y_0 = (L/6)(4\tan(\theta - \theta_X) - \tau L/B). \quad (3.11)$$

A particular Hookean crosslinker at position i provides a torque $\tau_i = x_i k_X(l_i - l_0)$ where l_i is the length of crosslinker i and x_i is its position along the bisector of the MTs, see Fig. 3.4. While crosslinkers have a chemical bond energy μ_X favouring attachment, this attachment cannot pull distant MTs together separated by tens of nanometers of cytoplasm, even if it is energetically favourable. Therefore we assume a crosslinker will attach only if the MT bond sites are separated by no more than l_M given by the Equipartition Theorem, $k_B T/2 = (k_X/2)(l_M - l_0)^2$. The total torque from all crosslinkers is

$$\begin{aligned} \tau_X &= 2 \int x(s) \frac{k_X}{\delta} (l(s) - l_0) ds \\ &= \frac{k_X}{\delta} \left(\frac{1}{3} l_M^3 + \frac{1}{6} l_0^3 - \frac{1}{2} l_0 l_M^2 \right) \frac{\cos(\theta_X/2)}{\sin^2(\theta_X/2)} \\ &= C \frac{\cos(\theta_X/2)}{\sin^2(\theta_X/2)} \end{aligned} \quad (3.12)$$

where the characteristic torque $C \approx 2-5 \text{ pN nm}$ contains the molecular properties of a crosslinker, using ranges from Table 3.3. The torque is unbounded as $\theta_X \rightarrow 0$. This divergence occurs because as the angle between the MTs shrinks, the number of crosslinkers that pull them together increases.

In mechanical equilibrium, the elastic restoring torque of the MT τ , found by solving Eqs. 3.11-3.10, will balance with the crosslinker torque τ_X from Eq. 3.12. Out of mechanical equilibrium, the angle θ_X obeys $d\theta_X/dt = \nu(\theta_X)(\tau_X(\theta_X) - \tau(\theta_X))$ where ν is the rotational mobility. If $\tau_X < \tau$, the incident MT will straighten. If $\tau_X > \tau$, the incident MT will bend towards the barrier MT and another crosslinker can attach. We find that $\tau_X(\theta_X) - \tau(\theta_X) < 0$ for $\theta_X > 0$ and passes through the origin (not shown). That is, attachment of a crosslinker increases the torque and, because of the geometry, allows yet another crosslinker to attach. Thus, the MT becomes entrained.

For $L = 3 \mu\text{m}$, the MT can access the entrained state through this pathway at collision angles up to 90° . At $L = 1 \mu\text{m}$, this pathway leads to entrainment for $\theta < 65^\circ$. These angles are comparable to angles at which entrainment occurs. This tells us that thermal fluctuations in the pre-entrained free tip are sufficient to allow the crosslinkers to entrain the incident MT.

3.4. Entrainment and crossover probabilities

Bending induced by the drag force of cytoplasmic streaming [7] will increase the range of angles that can be entrained, however it is not necessary.

This calculations tells us when entrainment *may* occur; to find out the probability that it *will* occur, we use an adiabatic approach described below.

3.4 Entrainment and crossover probabilities

Entrainment and crossover do not occur deterministically but rather, for each collision angle θ , there is a probability that the incident MT will entrain, $p(\text{ent}|\theta)$ or crossover, $p(\text{cross}|\theta)$. In this section, we derive a model to compute these probabilities.

In thermodynamic equilibrium, a pair of collided MTs will exhibit collision resolution $j \in \{\text{ent}, \text{cross}\}$ with probability given by the Maxwell-Boltzmann distribution

$$P_j = \frac{1}{Z} \exp(-E_j/k_B T). \quad (3.13)$$

where Z is a normalizing factor. The MTs in living cells are open systems far from equilibrium. However, a separation of timescales allows us to make an adiabatic approximation and use a modified version of Eq. 3.13. The elastic relaxation timescale of the MT is $\tau_{\text{relax}}^{-1} \approx 10^3 \text{ s}^{-1}$ [71], and typical values for MAP kinetics are s^{-1} [43, 62]. Meanwhile, on the relevant length scale of $L \sim 3 \mu\text{m}$, MT growth is slow $v_g^p/L \approx 1 \text{ min}^{-1}$, and we found above that MT-cortex anchoring is also slow, $k_{\text{on}}L \approx 1 \text{ min}^{-1}$, $k_{\text{off}} \approx 10^{-4} \text{ min}^{-1}$. Thus, mechanics and crosslinking kinetics occur on a fast timescale of seconds, while MT growth and anchoring kinetics occur on a slow timescale of minutes or longer.

On the slow timescale of MT growth and anchoring, the incident MT has free length $L + l(t)$ which grows at rate v_g^p . Mechanics and crosslinking are reversible and occur on the fast timescale, so an ensemble will have a distribution of n_X , the number of crosslinkers attaching the incident and barrier MTs, given by

$$\begin{aligned} p(n_X \geq 1 | \theta, l, L) &= \frac{1}{Z} \sum_{n_X=1}^{\infty} \exp(-E_{\text{ent}}(l, L, n_X)/k_B T) \\ p(n_X = 0 | \theta, l, L) &= \frac{1}{Z} \exp(-E_{\text{cross}}(l, L)/k_B T). \end{aligned} \quad (3.14)$$

In this case, the normalizing factor is

$$Z = \sum_{n_X=1}^{\infty} \exp(-E_{\text{ent}}(l, L, n_X)/k_B T) + \exp(-E_{\text{cross}}(l, L)/k_B T). \quad (3.15)$$

3.4. Entrainment and crossover probabilities

We think of $n_X \geq 1$ as states that, if anchored, would be entrained, while $n_X = 0$ states would cross over the barrier. We measure time on the slow scale, t , from the time the incident MT's plus-end arrives at the collision site, so $l = v_g^p t$. In the time interval $(t, t + dt)$, a portion $g(v_g^p t)dt$ of the ensemble is anchored, as described in Eq. 3.2. At any time t , the mechanics and crosslinking remain in equilibrium, so Eqs. 3.14 are satisfied. For a given free length of L ,

$$p(ent|\theta, L) = \int_0^\infty p(n_X \geq 1|\theta, l, L)g(l)dl. \quad (3.16)$$

The overall probability of entrainment at collision angle θ is given by the the following equation, the principal result of this paper:

$$p(ent|\theta) = \int_0^\infty \int_0^\infty p(n_X \geq 1|\theta, l, L)g(l)g(L)dldL. \quad (3.17)$$

In a similar manner, we calculate the overall probability of crossover at collision angle θ as

$$p(cross|\theta) = \int_0^\infty \int_0^\infty p(n_X = 0|\theta, l, L)g(l)g(L)dldL. \quad (3.18)$$

The collision resolution probabilities $p(ent|\theta)$ is shown in Fig. 3.5A for both WT and *clasp-1* anchoring kinetics. Crossover probability $p(cross|\theta)$ is the complement, $1 - p(ent|\theta)$.

The model parameters are listed in Table 3.3.

Some experimental studies measure $p(\theta|ent)$ rather than $p(ent|\theta)$, that is, the angular distribution of all entrainment events. We convert between the two using Bayes' rule, $p(\theta|ent) = p(ent|\theta)p(\theta)/\int p(ent|\theta')p(\theta')d\theta'$ with the approximating assumption that collisions are uniformly distributed in collision angle. These are shown in Fig. 3.5B. The experimental observations from Ambrose and Wasteneys [7] are also shown. In order to dismiss coincidences, the authors only reported readily noticeable changes in orientation, which would underreport low-angle collisions. For this reason, we assume the uncertainties are large for collisions below 20° and omit them from the figure.

The results are insensitive to model parameters. Varying parameters $k_{on}, k_{off}, \delta_\parallel, \mu_X, E_{cat}, B$ and d by $\pm 10\%$ led to no significant change in the collision resolution probabilities.

3.5. Discussion

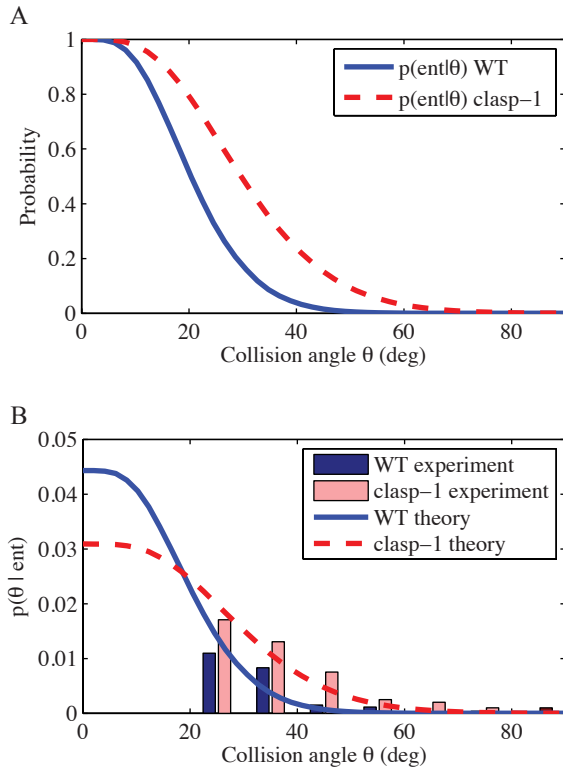


Figure 3.5: Collision resolution probabilities. (A) Probability of entrainment given by Eq. 3.17 for WT and *clasp-1* anchoring kinetics. Dashed lines are an upper bound for probability of collision-induced catastrophe. (B) Distribution of zippering angles for WT and *clasp-1* anchoring kinetics, along with experimental histograms from Ambrose and Wasteneys [7]. These are calculated from the results in panel A using Bayes' Rule. In the experimental histograms, we exclude entrainment events below 20° since low-angle entrainment events are difficult to resolve experimentally.

3.5. Discussion

energy of the incident MT.

A major prediction of our model is the limited significance of collision-induced catastrophe, in agreement with observations in *Arabidopsis*. However, Dixit and Cyr [44] report significant collision-induced catastrophe in Tobacco BY2 cells. As noted above, one possible explanation is a difference in anchoring in different organs and species. Another possible explanation is the action of an unknown MAP at collision sites, which may promote catastrophe.

This model makes several testable predictions concerning MT-cortex anchoring. The parameter fits found in Table 3.1 demonstrate that the association and dissociation rates in WT and *clasp-1* of *Arabidopsis* are slow. Furthermore, these parameters suggest how CLASP affects anchoring. The *clasp-1* mutant has roughly half the WT k_{on} , but leaves k_{off} unaffected. This suggests CLASP is involved in promoting anchor association between MTs and the cortex, while it is not involved in dissociation of anchors. The model also predicts that faster anchoring kinetics lead to higher rates of collision-induced catastrophe.

This model predicts that the probability of entrainment decreases monotonically with collision angle. This is in agreement with observations of Dixit and Cyr [44], but contrasts with the results of Ambrose and Wasteneys [7] (see Fig. 3.5B), where entrainment at small angles is not reported. However, as mentioned above, in order to dismiss coincidences, the authors only reported readily noticeable changes in orientation, which would underreport low-angle collisions.

The adiabatic approach we use here allows us to produce collision resolution probabilities with only a few, and experimentally well-constrained, parameters: the MT bending modulus, crosslinker spacing, and the crosslinker bonding energy. Moreover, it is independent of the details of the pathway a particular MT follows to its proper collision resolution, which remains to be experimentally elucidated. However, the approach has several drawbacks. It relies heavily on slow anchoring and implicitly assumes there are no impediments to the rapid exploration of the energy landscape. A dynamic approach involving either Langevin equations [83, 142] or Fokker-Planck equation [11, 97] remains desirable, however this will require kinetic rate constants for all processes and other presently unmeasured experimental details.

Chapter 4

Cortical microtubule organization at the cell scale³

4.1 Introduction

In this chapter, I present a computational study of CMTs in plants. We simulate several thousands of MTs over timescales of minutes to hundreds of minutes, including the effects of CIC, plus-end entrainment and MT-dependent nucleation. We explicitly model the *mor1-1* and the *clasp-1* mutants of *Arabidopsis thaliana* and find agreement with experiments for *mor1-1*, but not *clasp-1*. Our results illustrate assumptions under which an ordered array will emerge, and assumptions under which it does not.

4.2 Materials and methods

Ambrose and Wasteneys [7] and Shaw et al. [120] report CMTs switching spontaneously between growth (g), pause (p) and shrinkage (s). This three-state dynamic instability model thus involves eight parameters: six transition rates between the states f_{ij} where $i, j = g, p, s$, and growth and shrinkage velocities v_g and v_s . As a simplification of this three-state model, a two-state dynamical instability model involving four parameters has been studied [46, 116] and used extensively in cell biology [56, 60, 139]. The mean length Dogterom and Leibler [46] and mean lifetime [116] of a MT in the two-state model depend on a threshold quantity $f_{gs}v_s - f_{sg}v_g$. If the quantity is positive, the MTs tend to shrink more than they grow, and the MTs will have a finite mean length and mean lifetime. Otherwise, on average, they tend to grow forever. For the three-state case, we compute the equivalent equations below.

³A modified version of this chapter has been published as Allard, Wasteneys and Cytrynbaum, “Mechanisms of self-organization of cortical microtubules in plants revealed by computational simulations”, Molecular Biology of the Cell, 21 p. 278, 2010 (see bibliography [3]).

4.2. Materials and methods

In the absence of interactions, the length distribution of a population can be modeled using a partial differential equation [46]. For the two-state model,

$$\frac{\partial}{\partial t} \begin{bmatrix} N_g \\ N_s \end{bmatrix} = A \begin{bmatrix} N_g \\ N_s \end{bmatrix} + \frac{\partial}{\partial l} \left(V \begin{bmatrix} N_g \\ N_s \end{bmatrix} \right) \quad (4.1)$$

where $N_g(l, t)$ and $N_s(l, t)$ represent the density of growing and shrinking MTs of length l , respectively, and

$$A = \begin{bmatrix} -f_{gs} & f_{sg} \\ f_{gs} & -f_{sg} \end{bmatrix}, \quad V = \begin{bmatrix} -v_g & 0 \\ 0 & +v_s \end{bmatrix} \quad (4.2)$$

represent transitions between states and advection, respectively. If new MTs are nucleated with zero length and in the growing state at rate k , the boundary conditions are $v_g N_g(0, t) = k$ and $N_s(l, t) \rightarrow 0$ as $l \rightarrow \infty$. This leads to a unique steady-state $N_i = \alpha_i \exp(-l/\bar{l})$ where

$$\bar{l} = \frac{v_g v_s}{f_{gs} v_s - f_{sg} v_g} \quad (4.3)$$

as long as the denominator is positive [46]. The mean lifetime can be found by assuming the system is in steady-state, when nucleation must balance a constant death rate τ^{-1} ,

$$k = \frac{1}{\tau} \int_0^l N_g + N_s dl \quad (4.4)$$

where τ is the mean lifetime. This gives

$$\tau = \frac{v_g + v_s}{f_{gs} v_s - f_{sg} v_g} \quad (4.5)$$

in agreement with [116]. For the three-state model, the partial differential equations now involve $N_i(l, t)$, $i = (g, p, s)$ and the matrices become

$$A = \begin{bmatrix} -(f_{gp} + f_{gs}) & f_{pg} & f_{sg} \\ f_{gp} & -(f_{pg} + f_{ps}) & f_{sp} \\ f_{gs} & f_{ps} & -(f_{sg} + f_{sp}) \end{bmatrix} \quad (4.6)$$

and

$$V = \begin{bmatrix} -v_g & 0 & 0 \\ 0 & 0 & 0 \\ 0 & 0 & +v_s \end{bmatrix}. \quad (4.7)$$

4.2. Materials and methods

The mean length and mean lifetime can be found as above,

$$\bar{l} = \frac{v_g v_s (f_{pg} + f_{ps})}{D} \quad (4.8)$$

$$\tau = \frac{v_s (f_{gp} + f_{pg} + f_{ps}) + v_g (f_{sp} + f_{pg} + f_{ps})}{D} \quad (4.9)$$

where the denominator

$$D = v_s (f_{gp} f_{ps} + f_{gs} f_{pg} + f_{gs} f_{ps}) - v_g (f_{pg} f_{sg} + f_{pg} f_{sp} + f_{ps} f_{sg}) \quad (4.10)$$

is the threshold quantity: if it is negative, the mean length and lifetime are infinite. In both the two-state and three-state models, if the minus-end shrinks at a constant velocity, we make the coordinate transformation

$$v_g = v_g^p - v_s^m \quad (4.11)$$

$$v_s = v_s^p + v_s^m. \quad (4.12)$$

There is an equivalent threshold quantity that determines if the MTs tend to remain finite or grow indefinitely. Note that these simplified models only consider dynamic instability: they are only valid in the absence of interactions between the MTs and any growth boundaries, and in the abundance of free tubulin. Thus the mean length and mean lifetime should be thought of as characteristic scales that are perturbed by MT-MT interactions and the action of MAPs. Tables 4.1 and 4.2 summarize parameters from the literature that we use in this paper.

4.2. Materials and methods

	Kawamura and Wasteneys [78]				Shaw et al. [120]	Dixit and Cyr [44]
	WT 21°C	WT 31°C	mor1-1	21°C	mor1-1	31°C
f_{gp} (min ⁻¹)	0.20	0.38	0.20	0.96	0.28	—
f_{gs} (min ⁻¹)	0.17	1.59	0.38	0.82	0.52	1.61
f_{pg} (min ⁻¹)	2.01	1.40	1.56	0.70	0.26	—
f_{ps} (min ⁻¹)	1.02	0.70	0.56	0.62	1.30	—
f_{sg} (min ⁻¹)	1.00	1.99	1.18	0.61	0.59	3.26
f_{sp} (min ⁻¹)	0.31	0.44	0.59	1.21	1.09	—
v_g^p (μm/min)	3.50	6.50	2.50	2.00	3.69	5.60
v_s^p (μm/min)	9.00	12.00	6.20	3.80	5.80	10.09
v_s^m (μm/min)	—	—	—	—	0.53	—
Assuming minus-end stationary						
\bar{l} (μm)	-15.12	13.55	-11.47	3.27	7.89	-28.1
τ (min)	-6.46	3.83	-7.38	4.47	5.26	-7.8
Assuming minus-end shrinking, $v_s^m = 0.53 \mu\text{m}/\text{min}$						
\bar{l} (μm)	-21.46	9.49	-49.67	1.74	5.2	94.5
τ (min)	-10.18	2.79	-37.03	2.81	3.75	27.5

Table 4.1: Dynamic instability parameters from three-state models using data from [78, 120] and two-state models using data from [44]. The mean length \bar{l} and mean lifetime τ in the absence of interactions or cell boundaries are computed using Eqs. 4.3-4.9. The minus-end shrinking velocity is taken from the average shrinking velocity, including pauses, in [120]. Since \bar{l} and τ consider only the effects of dynamic instability, they should be thought of as characteristic scales which are perturbed by MT-MT interactions and the action of MAPs.

Parameter	Meaning	Value	Reference
θ_Z	Critical zippering angle	$40^\circ, 60^\circ$	[7, 44]
θ_{nuc}	Branched nucleation angle	40°	[100]
k_0	Background nucleation rate	$10 \mu\text{m}^{-2} \text{min}^{-1}$	Estimated
k_1	MT-dependent nucleation rate	10^3 min^{-1}	Estimated
p_{cat}	Probability of catastrophe upon steep collision	0.09–0.6	[44, 138]
p_{zip}	Probability of zippering upon shallow collision	1	[44]
δ	Spacing between bundled MTs	25 nm	[29]

Table 4.2: Parameters used in the model in addition to the dynamic instability parameters in Table 4.1.

4.2. Materials and methods

We assume the minus-end is either always static, or continuously shrinking with constant rate v_s^m . Shaw et al. [120] report MT minus ends spending 25.3% of the time shrinking at, on average, $2.78 \mu\text{m}/\text{min}$, and 8.4% of the time growing at $1.96 \mu\text{m}/\text{min}$, and the remaining time (66.3%) paused. Thus, for instances in which we assume minus ends shrink, we use an appropriately weighted average of these data,

$$v_s^m = 0.253(2.78 \mu\text{m}/\text{min}) + 0.084(-1.96 \mu\text{m}/\text{min}) + 0.663(0) = 0.53 \mu\text{m}/\text{min}. \quad (4.13)$$

When two MTs collide, the outcome depends on the angle between the incident and barrier MTs [132], which we call the collision angle θ_X . We define the critical entrainment angle θ_Z as follows. If $\theta_X > \theta_Z$, the collision is steep and catastrophe occurs with probability p_{cat} , otherwise the incident MT crosses over the barrier MT (with probability $1 - p_{cat}$). In *Arabidopsis*, 9% of steep-angle collisions result in catastrophe in petiole epidermal cells and 25% in leaf pavement cells [138], while in tobacco BY2 cells, catastrophe results 60% of the time [44]. In these studies, the angles 45° and 40° , respectively, were found to delineate the transition between entrainment and catastrophe.

If $\theta_X < \theta_Z$, the collision is shallow and plus-end entrainment occurs with probability p_{zip} . After an entrainment event, the extant segment of the incident MT remains in its pre-collision configuration, but the plus end continues to grow parallel to the barrier MT. Thus, the MT is now composed of two line segments with a kink. In this paper we assume this phenomenological description of entrainment, neglecting fine-grain biophysical properties of the kink. The segment from the kink to the plus-end of the entrained MT is kept a distance of $\delta = 25 \text{ nm}$ from the barrier MT in agreement with electron microscopy of crosslinking due to MAP65 [29].

We consider two modes of MT nucleation. The first is independent of the extant MT array. MTs of zero initial length and uniform random orientation are inserted randomly into the cortex, at rate k_0 (in $\mu\text{m}^{-2} \text{ min}^{-1}$). The second is MT-dependent nucleation, where new MTs are nucleated off extant MTs. The rate of MT-dependent nucleation will depend upon both the length of existing polymer and the number of available γ -TuRC in the cytoplasm [100]. However, we assume the γ -TuRC is rate-limiting and thus MT-dependent nucleation occurs at a constant rate k_1 in min^{-1} . Once the new MT is nucleated, its plus-end immediately begins dynamic instability, and if $v_s^n > 0$, the minus-end immediately begins shrinking. In reality, there is likely to be a delay before katanin severs the minus-end [118], but since an actual lag time is unknown, we assume this is negligible. Also, we find

4.2. Materials and methods

that a completely static minus-end only delays the onset of self-organization, suggesting the katanin delay would not change our results significantly.

There are physical details not explicitly included in the model, such as the mechanical properties of the MTs, the cortex and the anchors connecting them. We assume that anchors are sufficiently strong and densely distributed along MTs so that (1) the radius of curvature of the cortex is not mechanically significant and (2) the kink in an entrained MT remains in place even if the barrier MT is removed through depolymerization.

There are several ways to measure how well-oriented an array is. A common qualitative approach is to plot a histogram of MT angles defined so that the dominant direction is either 0 or 90° [7, 69]. If the angle distribution is unimodal, its standard deviation serves as a quantitative measure of orientation. As an extension of this, the distribution can be weighted by length, i.e., the angles of longer MTs count for more in the histogram.

More generally, Baulin et al. [16] define an order parameter $0 < S_l < 1$ based on an angular cost function, weighted by l_i^2 where l_i is the length of each MT. Here, we define a slightly modified version of their order parameter,

$$S = \sum_i l_i (\cos^2(\theta_i - \Omega) - \sin^2(\theta_i - \Omega)) / \sum_i l_i \quad (4.14)$$

where θ_i is the angle of each straight MT segment and Ω is the dominant angle. Heuristically, S represents the relative difference between the projected polymer length in the dominant direction and the projected polymer length in its perpendicular direction.

4.2.1 Details of computer simulation

We simulate on a $10\text{ }\mu\text{m} \times 10\text{ }\mu\text{m}$ domain, which is a typical size of a plant cell face in early interphase, with periodic boundary conditions in both directions, except where we explicitly explore the consequences of boundaries. All simulations are run for 1000 minutes and were replicated ten times with different, random initial conditions. We use dynamic instability parameters from Table 4.1 and, unless otherwise noted, other parameters from Table 4.2.

The stochastic simulation uses a mixed-timestep method, which combines the stochastic-timestep Gillespie method with a fixed-timestep method. For MTs switching between MT states (competing Poisson processes with rates f_{ij}) and constant growth and shrinkage velocities, we use a Gillespie algorithm to simulate resulting in a variable timestep on the order of $t = 10^{-3}\text{ min}$. Detect and resolution of collisions is more computationally

4.2. Materials and methods

taxing, so we do not do it every Gillespie timestep. Instead, we use a fixed timestep of $t = 0.05$ min.

Detecting collisions by comparing the plus-end of every MT with the bulk length of every other MT would be an $O(n^2)$ computational cost [113] where n is the number of MTs. To increase the efficiency, we split the domain into a rectangular grid where each grid box has side length Δx_{ColDet} , as shown in Fig. 4.1.

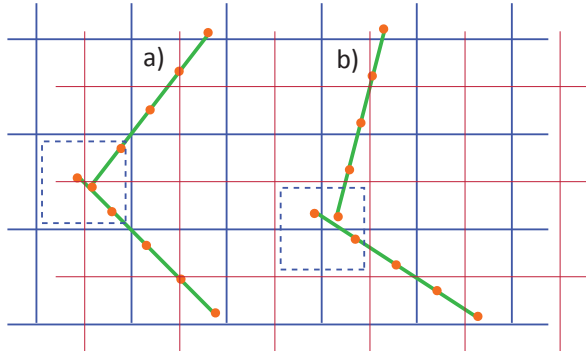


Figure 4.1: Collision detection algorithm. The domain is divided into grid boxes (blue), each MT is determined to occupy a grid box by determining the location along its length at regular intervals, and only MTs occupying the same grid box are compared. (a) The MT collision is detected in the dashed grid box. (b) A single grid (blue grid) will miss some collisions, but with a second grid staggered from the first (red grid) no collision goes undetected.

$$O\left(\frac{n^2 \Delta x_{ColDet}}{L} + \frac{n}{\Delta x_{ColDet}}\right), \quad (4.15)$$

which can be made smaller by choosing Δx_{ColDet} . This grid will not detect MTs near the edges of one grid box (See Fig. 4.1). To detect all collisions, we use two subgrids staggered by $0.5\Delta x_{ColDet}$.

4.3. Results

4.3 Results

4.3.1 Collision-induced catastrophe does not lead to ordering for physiological kinetic parameters.

With parameters as given in Tables 4.1 and 4.2, collision-induced catastrophe (CIC) did not lead to any ordering. Instead, they lead to sparse arrays shown in Fig. 4.2A. For high values of $p_{cat} = 0.9$ (shown in the figure), the MTs were too short in length and lifetime for orientation to emerge, while for low values of $p_{cat} = 0.1$, they simply did not interact enough. Intermediate values of p_{cat} also failed to organize. However, Baulin et al. [16] report that pause-inducing collisions alone are enough to give rise to an oriented array, a result we confirm with our simulations (see Fig. 4.2B and Supplemental Movies S1 and S2 of [3]). Here, we show that the pause-inducing collision model is a limiting case of the catastrophe-inducing collision model.

To understand the difference between catastrophe-inducing collisions and pause-inducing collisions, we consider the two-state model, which has five parameters, v_g^p , v_s^p , f_{gs} and f_{sg} which all pertain to the plus-end, and v_s^m , which pertains to the minus-end. In addition, the rate of nucleation, k_0 , provides an additional time scale. However, if we rescale time to be measured in units of $T \equiv (v_g^p)^{-2/3} k_0^{-1/3}$ and length $L \equiv (v_g^p/k_0)^{1/3}$, then the two-state model is described by four parameters,

$$\alpha = v_s^p/v_g^p \quad (4.16)$$

$$\beta = f_{gs}T \quad (4.17)$$

$$\gamma = 1/(f_{sg}T) \quad (4.18)$$

$$\delta = v_s^m/v_g^p. \quad (4.19)$$

(Note that scaling by \bar{l} and τ is not appropriate here, since we are sometimes in the infinite-growth regime.) To ensure MT nucleation can occur, $\delta < 1$. In this parametrization, the model of Baulin et al. [16] corresponds to $\alpha, \beta, \gamma \rightarrow 0$ and it completely described by one parameter, δ (related to their α , which they set in [0.17, 1.5]). The two-state parameters reported in [44] (Table 4.1) give $\alpha = 1.8$, $\beta = 0.16$, $\gamma = 3.1$ and either $\delta = 0$ (since they did not study minus-end dynamics) or $\gamma = 0.09$ (using v_s^m from [120]).

After conducting a random sweep of 103 kinetic parameter sets, we conclude that CIC only leads to self-organization in the limit where the shrinkage rate and catastrophe rate are approximately zero ($v_s^p, f_{gs} \approx 0$) and the rescue rate is much larger than the catastrophe rate ($f_{sg} \gg f_{gs}$), consistent with Baulin et al. [16].

4.3. Results

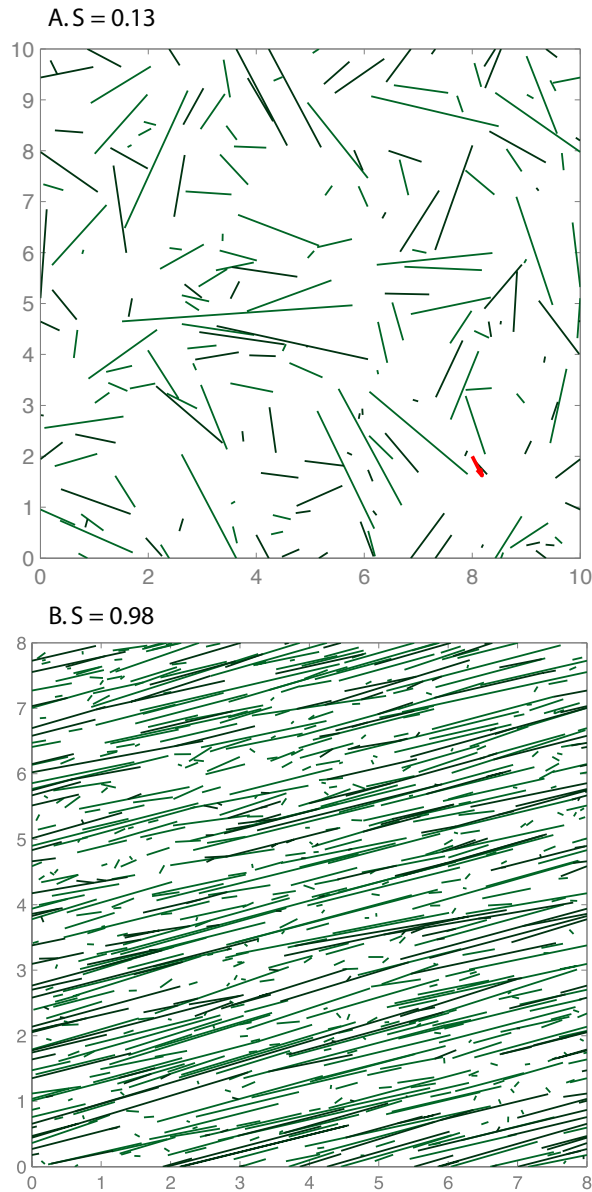


Figure 4.2: Simulation snapshots at $t=60$ min with (A) collision-induced catastrophe only, using parameters from WT at 31°C (Kawamura and Wasteneys 2008), and (B) collision-induced pauses, using the single-state model of Baulin et al. [16].

4.3. Results

4.3.2 Plus-end entrainment, with or without CIC, results in an ordered array.

Simulations that include entrainment gave rise to significant order parameters within the first 60 min. In Fig. 4.3, we display snapshots from the simulations for the four kinetic parameter sets taken from Kawamura and Wasteneys [78] for plus-end dynamics and the average v_s^m from Shaw et al. [120]. In Fig. 4.3A-C, a single dominant direction is evident with patches of deviation present. The dominant direction (red arrows) is uniformly random (data not shown) across simulations and persists for at least 10^3 min.

Movies showing the time course of some of these simulations are in Supplemental Material S3-S7 of [3]. Initially, several locally ordered domains emerge, grow and shrink (but never rotate, as reported in Chan et al. [31]). By 10^3 min, typically a single orientation dominates. However, sometimes the cortex is divided into two domains with distinct dominant orientations. These directions were never observed to differ by more than the critical entrainment angle Z . It remains possible that one of these domains becomes globally dominant on timescales much larger than 10^3 min.

In Fig. 4.4A-B, we show time series from 10 runs with WT 31°C parameters (blue curves). The mean lengths increase slowly. After $\approx 10^3$ min, in each simulation, the mean MT length converges to a value below \bar{l} , the predicted mean length in the absence of interaction (Table 4.1, Eq. 4.8). For comparison, single CMTs have been reported to be $2 - 4 \mu\text{m}$ when measured by transmission electron microscopy [63]. The number of MTs converges quickly to roughly 10^3 (data not shown). Note that the steady-state number of MTs depended on k_0 , and we chose $k_0 = 10 \mu\text{m}^{-2} \text{min}^{-1}$ to give $\approx 10^3$ MTs.

Using S as our measure of order, we conclude that plus-end entrainment does give rise to order. This order emerges with a timescale below 10^2 min (Fig. 4.4B), in agreement with the observed time-to-order in vivo [135]. The full orientational distribution are shown in Fig. 4.4C. Notably, without CIC in the simulations (ie. $p_{cat} = 0$) ordering still emerged, see Fig. 4.6A. Ordering also occurred using parameters from Shaw et al. [120] and for the two-state model using parameters from Dixit and Cyr [44] (data not shown).

4.3.3 With kinetic parameters taken from the *mor1-1* mutant at 31°C, ordered arrays do not form.

In simulations of the *mor1-1* mutant at 31°C, the MTs were short and therefore much lower in total polymer density. From Fig. 4.5A, we see their

4.3. Results

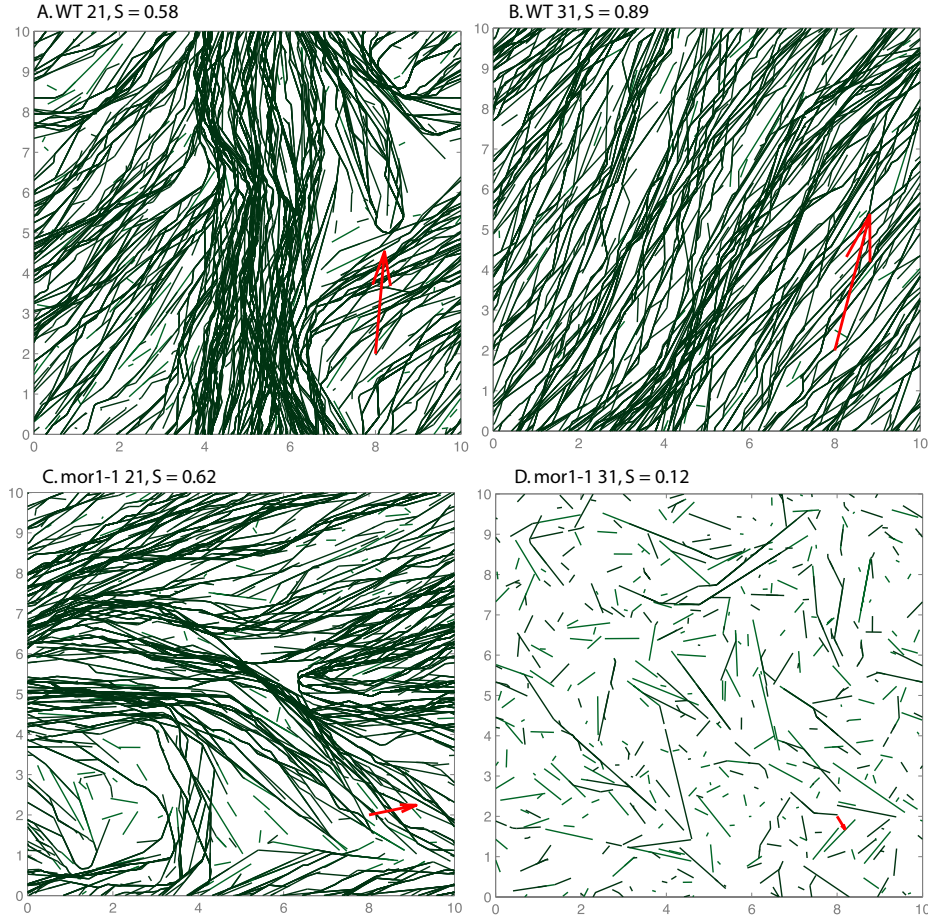


Figure 4.3: Collision-induced catastrophe at steep angles ($\theta > 40^\circ$) and entrainment at shallow angles ($\theta < 40^\circ$) for four sets of kinetic parameters from Kawamura and Wasteneys [78] and continuously depolymerizing minus-end [120]. The top and bottom rows are WT and *mor1-1* kinetic parameters, respectively, and the left and right are at 21°C and 31°C, respectively. New MTs are inserted randomly at a rate of $k_0 = 10 \mu\text{m}^{-2} \text{ min}^{-1}$. The boundaries are periodic in both directions. After 60 minutes, order emerges in local domains in all cases except *mor1-1* at 31°C. The direction of the red arrow indicates the dominant direction of the MT array, while their lengths are proportional to the order parameter.

4.3. Results

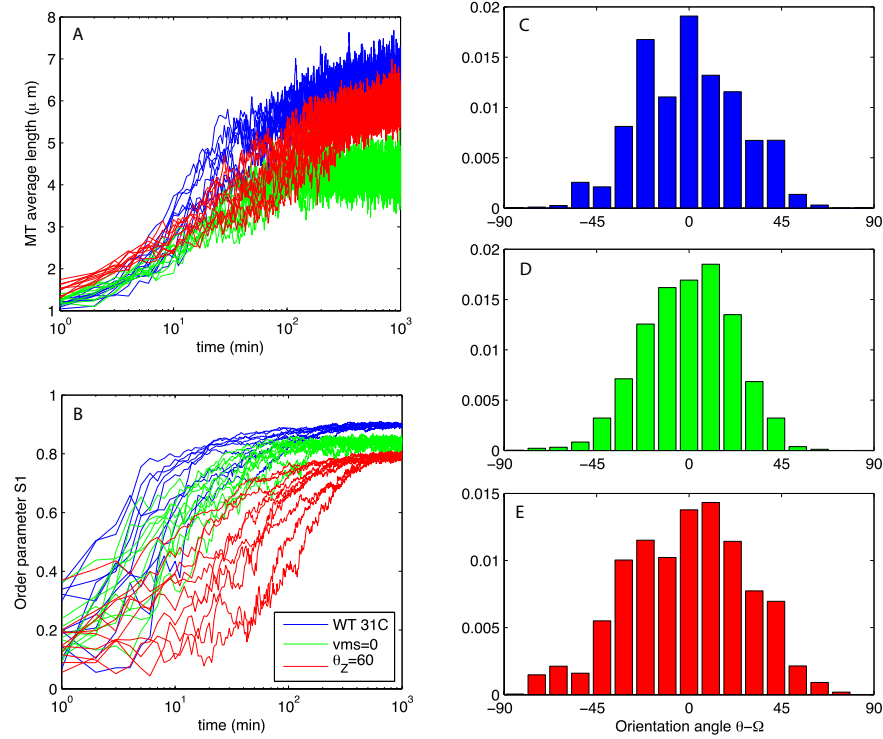


Figure 4.4: Data from WT (WT) simulation runs. (A) Average length of a MT. (B) Order parameter S_1 , given by Eq. 4.14. All simulations use kinetics from WT at 31°C in Table 4.1. (C-E) Histograms from selected runs depicted in Fig. 4.3. Blue curves in A-B and histogram in C have a depolymerizing minus end and a critical entrainment angle of $\theta_Z=40^\circ$. Green curves in A-B and histogram in D have a static minus-end ($v_s^p = 0$) with $\theta_Z=40^\circ$, and red curves in A-B and histogram in E have depolymerizing minus end with $\theta_Z=60^\circ$. Time series from ten independent simulations are shown in each case.

4.3. Results

average length is $0.5 \mu\text{m}$, roughly one sixth of their mean free length in the absence of interactions. Reducing the nucleation rate increased their mean length slightly, but still did not allow for ordering.

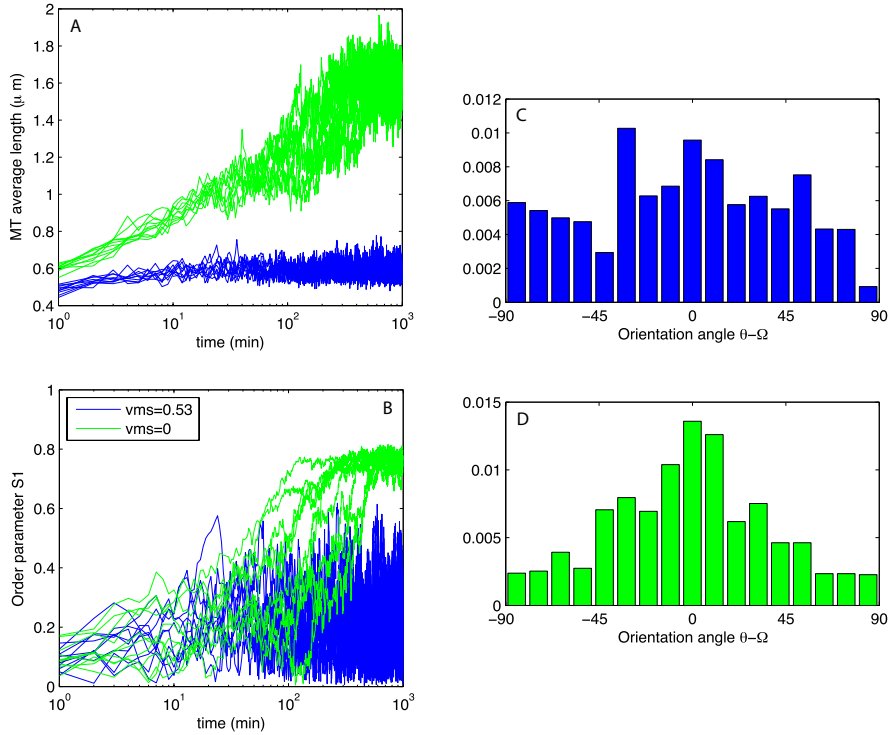


Figure 4.5: Data from simulations of the *mor1-1* mutant. (A) Average length of a MT. (B) Order parameter S_1 , given by Eq. 4.14. All simulations use kinetics from *mor1-1* at 31°C in Table 4.1. Blue curves in A-B and histogram in C have a depolymerizing minus end while green curves and histogram in D have a static minus-end ($v_s^p = 0$).

4.3.4 Static minus-ends delay, but do not prevent, array organization.

While three-state dynamic instability of MT plus-ends has been reported extensively [44, 78, 120], the hybrid treadmilling has been reported less often [120]. To explore the consequences of a freely depolymerizing minus-end, we ran simulations with static minus ends ($v_s^m = 0$).

4.3. Results

A typical array arising from $v_s^m = 0$ is qualitatively similar to the arrays in Fig. 4.3B, the equivalent runs with $vms = 0.53 \mu\text{m}/\text{min}$. The order parameter S after 10^2 min is, on average, also comparable (0.9 and 0.8 for $v_s^m = 0.53 \mu\text{m}/\text{min}$ and $v_s^m = 0$, respectively). However, static minus-ends appeared to delay the onset of self-organization. In Fig. 4.4B, we show the order parameter's time evolution for both $v_s^m = 0.53 \mu\text{m}/\text{min}$ (blue curves) and $v_s^m = 0$ (green curves). While the simulation with a shrinking minus-end has reached its well-ordered steady-state (within 10% of its steady-state order parameter S) within 20 min, it takes the simulation with static minus-ends roughly 80 min, which is four times longer. The dynamics of the minus-ends affect the average length of MTs (Table 4.1) in that if minus-ends are static, the MTs grow slightly longer. In simulations with kinetic parameters from the *mor1-1* mutant at 31°C , we find that static minus-ends induce a change sufficient to allow for ordering. Time series data for this kinetic parameter set are shown in Fig. 4.5A-B. The order parameter in Fig. 4.5B, shows that the mutant with a depolymerizing minus-end does not organize (blue curve). With static minus ends, organization is rescued (green curve). In this case, however, self-organization still takes longer than in simulations of WT plants with non-static minus ends.

4.3.5 Increasing the critical entrainment angle does not enhance, but rather delays, array organization.

MTs in the *clasp-1* mutant described by Ambrose and Wasteneys [7] entrain over a wider range of incident angles, with a mean entrainment angle roughly 11° larger than in WT, and demonstrate “hyperparallel” arrays, indicated by a smaller standard deviation of MT orientations. To test whether a higher critical entrainment angle can explain the hyperparallel arrays, we ran simulations in which we increased the critical entrainment angle from $\theta_Z=40^\circ$ to $\theta_Z=60^\circ$, which is equivalent to increasing the mean entrainment angle by 10° .

Qualitatively, the resulting arrays appear indistinguishable from the corresponding array in Fig. 4.2 (see Supplemental Movie S8 of [3]). However, examining the time course of the order parameter S reveals that the increased θ_Z delays and slightly reduces array ordering, similar to the case of static minus-ends. The time series of ordering is shown in red in Fig. 4.4B, with a typical angle distribution in Fig. 4.4E. This suggests that the *clasp-1* hyperparallel MT phenotype is dependent on another mechanism.

4.3. Results

4.3.6 MT-dependent branched nucleation leads to unrealistic array structures.

Up to this point, all MT nucleation has been assumed to occur uniformly in space and at random angles, referred to here as background nucleation. To explore the reports of MT-dependent branched nucleation, we ran simulations without background nucleation ($k_0 = 0$) and non-zero MT-dependent nucleation rate $k_1 = 10^3 \text{ min}^{-1}$.

These simulations always resulted in arrays with a distinct structure reminiscent of shattered glass. As with background nucleation, one or a few dominant angles emerged locally at early times, the domains grew or shrank, and often one direction dominated globally. However, the arrays were always sparse with large gaps free of persisting MTs. A typical snapshot is shown in Fig. 4.6C. Time courses of typical simulations are shown in Supplemental Movies S9 and S10 of [3].

While MT-dependent branch nucleation alone leads to an unrealistic array organization, this does not necessarily mean it is not important. We ran simulations with a combination of MT-dependent and MT-independent nucleation. As MT-independent nucleation is reduced, the arrays appeared more and more sparse. A simulation with a combination of nucleation types, $k_1 = 500 \text{ min}^{-1}$ and $k_0 = 5 \mu\text{m}^{-2} \text{ min}^{-1}$, is shown in Fig. 4.6D.

4.3.7 Catastrophe-inducing boundaries are enough to bias the dominant orientation.

Up to now, all simulations described were carried out on a square cortex with periodicity in both directions. That is, a MT that disappears off any edge appears from the opposite edge. When a dominant angle emerges in our simulations, it is uniformly random. In diffusely elongating plant cells, the dominant angle is transverse to the direction of elongation, indicating that there must be a symmetry-breaking mechanism that signals a preferred orientation to the MTs. One candidate for this mechanism is interaction with the apical and basal poles of the plant cell [47]. Real cells have distinct faces. Side walls may allow MTs oriented transverse to the elongation axis to continue growing indefinitely, unperturbed by boundaries between faces. In the longitudinal direction, MTs can treadmill onto the cross walls but rarely do [37]. It has been suggested that the boundaries of the poles inhibit MT growth, either sterically or through MAP activity [47]. We represent this interaction by imposing catastrophe on any MT that collides with the top or bottom of the cylinder.

4.3. Results

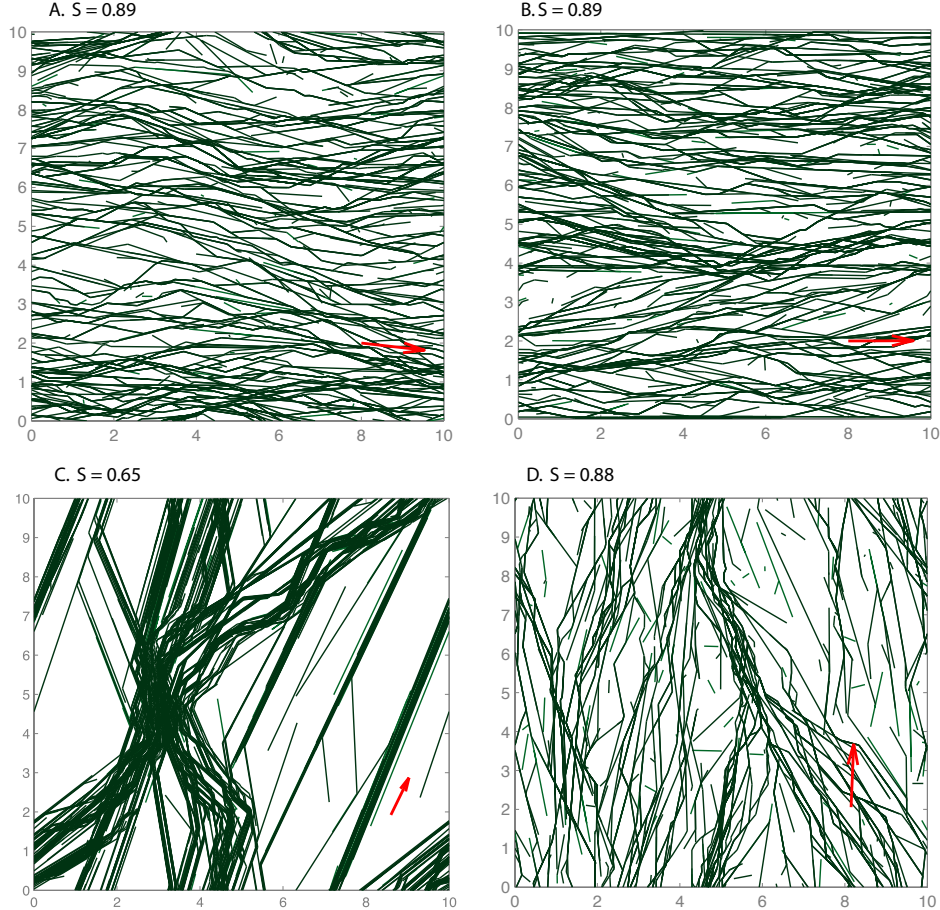


Figure 4.6: Simulation snapshots at $t=60$ min using kinetic parameters from WT at 31°C . (A) Entrainment at shallow angles ($< 40^\circ$), and no collision-induced catastrophe ($p_{cat}=0$). (B) A biased, transverse dominant angle that arises if two edges (here, the top and bottom) induce catastrophe. This provides a possible mechanism for selecting a direction transverse to the cell elongation axis. (C) Sparse array that results if all nucleation is branched MT-dependent nucleation. (D) Moderately sparse array arising from a combination of MT-dependent and MT-independent nucleation.

We find that this catastrophe-inducing boundary effect is enough to cause selection of the transverse angle as the dominant orientation. Snap-

4.4. Discussion

shots from these simulations are shown in Fig. 4.6B. At $t = 60$ min, not all non-transversely oriented patches disappear, yet the dominant transverse angle always persists.

In fact, even in the complete absence of MT-MT interactions, catastrophe-inducing boundaries at the cross walls will lead to a certain amount of ordering. MTs transverse to the elongation axis can treadmill indefinitely while those parallel to the elongation axis will quickly encounter a boundary. The ordering of MTs is therefore strongest near the cross walls and decays toward the midcell over a distance of roughly the mean length in the absence of interaction.

Even in the absence of any MT-MT interactions, MTs randomly nucleated on a cylindrical cortex can lead to a transverse ordering if collisions with the boundaries induce catastrophe. A MT plus-end a distance y from the boundary making an angle θ , measured from transverse the axis of the cylinder, can grow to a maximum length $L = (L_C - y)/\sin \theta$ where L_C is the cell length. In this case, the right boundary condition on the system of partial differential equations in Eq. 4.1 is $v_s N_s(L, t) = v_g N_g(L, t)$. The solution is still exponential with decay length \bar{l} but is truncated. The average length of MTs of angle θ at height y is

$$\langle l \rangle \propto \left(1 - e^{-y/(\bar{l} \sin \theta)}\right) \left(1 - e^{-(L_C - y)/(\bar{l} \sin \theta)}\right). \quad (4.20)$$

From this it is straightforward to compute the order parameter S . We can also compute a *local* order parameter $S(y)$ that takes into account all MTs passing through a given y value (a given circumference of the cylinder). Although $S(y)$ has no closed form, it can be computed numerically. We find that this boundary-induced ordering decays away from the boundaries towards midcell, with a decay length scale of roughly \bar{l} , shown in Fig. 4.7.

MT-MT interaction allows this boundary-induced orientation to propagate further into the midcell cortex. We also found that the introduction of catastrophe-inducing boundaries does not induce ordering in the CIC-only model described in Sec. 4.3.1.

4.4 Discussion

Recent genetic and pharmacological experiments on CMTs in plants have given rise to a model for the self-organization of these MTs into a parallel array. Here, we have presented the results of large-scale simulations of a quantitative implementation of this model. We find that self-organization into a parallel array can arise from a combination of MT dynamic instability,

4.4. Discussion

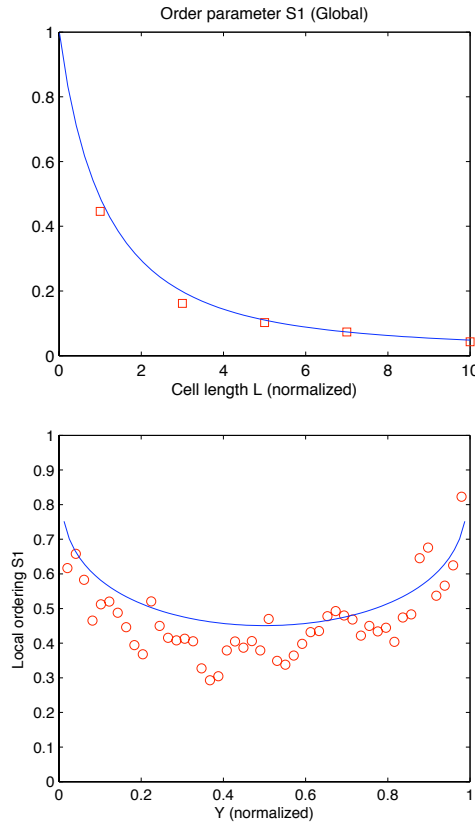


Figure 4.7: Orientational order over the whole cell, (Left) for various normalized cell lengths $L = \lambda L_C$ and (Right) as it varies across the length of one cell. The solid curve was found by Eq. 4.20, while the plot symbols are from the Monte Carlo simulation.

4.4. Discussion

plus-end entrainment and, in certain cases, CIC. The arrays that arise in our simulations appear qualitatively similar to the arrays in plant cells, including the local domains of orientation that are similar to the patchwork patterns in maturing *Chara* cells [134] and the outer epidermis of *Arabidopsis* hypocotyl cells [31]. In addition to recapitulating WT behavior, our model also agrees with mutant studies [78].

It has been proposed that CIC can explain ordering. Our results show that CIC is neither necessary nor sufficient for ordering when physiologically reasonable dynamic instability parameters are used. Previous modelling efforts have focused on the role of CIC in the emergence of order. Dixit and Cyr [44] showed that CIC in combination with plus-end entrainment leads to ordering. In light of our results, we suggest ordering in their model arises due to entrainment rather than CIC. The model of Baulin et al. [16] corresponds to a limit in which the growth rate dominates the shrinkage rate, and the rescue frequency dominates the catastrophe frequency. This model fails to self-organize when extended to a regime that matches reported kinetic parameters [44, 78, 120].

Plus-end entrainment with branched MT-dependent nucleation gives rise to an oriented array that appears sparse since areas of low MT content have no candidate nucleation sites, while areas of high MT content have many. From this, we conclude that exclusive MT-dependent branched nucleation leads to unrealistic array structures. Free nucleation appears to be necessary to explain the dispersed arrays seen *in vivo*. This appears to contradict the hypothesis that branched nucleation helps to disperse the array throughout the cortex [132], but is consistent with the observation that during recovery from drug-induced disassembly, the initial transverse order of freely nucleated MTs is progressively lost when most subsequent MTs are produced by branch-form nucleation [135]. While MT-dependent branch-form nucleation alone leads to unrealistic arrays, this does not suggest that it does not occur. As proposed by Wasteneys and Ambrose [132], it may be specifically promoted under conditions where it is beneficial to change the predominant orientation of MTs. Recent improvements in live cell imaging has enabled the detection of microtubule-dependent nucleation that is parallel to the parent MT (see Fig. 1C in Ambrose and Wasteneys [7]) and this alternative form of MT-dependent nucleation might prove to be much more common than previously thought [132].

We find that increasing the critical entrainment angle does not enhance the array order. In fact, order is reduced slightly and delayed. This conflicts with recent experiments in which Ambrose and Wasteneys [7] observed “hyperparallel” arrays in the *clasp-1* mutant. This suggests that the CLASP

4.4. Discussion

protein affects array organization through more than simply modulating the critical entrainment angle.

Two of the phenomena we neglect in our simulations are increased MT stability through bundling, and severing after crossover. MTs within bundles remain dynamic, however, with slightly modified kinetic parameters [127]. It is unknown whether this effect arises simply through the reduced collision frequency, or whether it is important for MT array organization. MT severing at sites of existing crossovers, possibly mediated by katanin, has also been reported [138], however this appears rarely as severing of elongated MTs is rare [120].

Three novel predictions arise from this work. First, if the transverse dominant direction is selected by catastrophe-inducing boundaries at the top and bottom edges of the cell, then the time to order will increase as the cell length increases, as it takes longer for the signal to propagate inwards.

The other two predictions demonstrate the paradoxical influence of static minus ends. First, if minus ends do not become mobile in wildtype (e.g. in a katanin knockout), we predict ordering to take fourfold longer. Second, we predict that a similar perturbation of the *mor1-1* 31°C mutant rescues ordering.

This last set of predictions illustrates one of the values of computational modeling. The subtle influence of static as opposed to mobile minus-ends, which in one case promotes and in the other inhibits organization, is essentially impossible to tease out without recourse to computational techniques.

Chapter 5

Cell edges can drive cortical microtubule organization⁴

5.1 Introduction

In Chapter 4, we studied CMTs on an abstract surface with no boundaries (i.e. periodic boundaries), and on a cylinder. However, multicellular plant tissues contain cells that are most often polyhedral in shape. In the absence of clear spatial input from the cell (such as centrosomes), what determines whether an array will be oriented transverse or longitudinal relative to the cell axis? And how is the orientation of cortical arrays coordinated between different cell faces? Recent experiments described by Ambrose et al. [9] show that the inherent geometry of the cell provides a powerful spatial cue that contributes to MT array organization, and that the non-uniform distribution of the MAP CLASP is required to modulate this intrinsic bias. CMTs were observed to undergo catastrophe when encountering specific cell edges or regions of edges. Local accumulation of CLASP to distinct edge domains enables MTs to grow around sharp bends at cell edges, which leads to the formation of stable MT bundles that traverse two or more faces.

Here, we use computer simulations of CMTs on a “cube” with differentially traversable edges to support the hypothesis that external input can result in highly biased MT arrays.

5.2 Biophysical basis for edge-induced catastrophe

In this section, I present a biophysical argument that the curvature of an edge promotes catastrophe, that under certain circumstances (but not all),

⁴A modified version of this chapter is in preparation to be submitted as Ambrose, Allard, Cytrynbaum and Wasteneys, “Asymmetric distribution of CLASP to specific cell edges enables microtubule growth between cell faces and drives cell-wide microtubule order in *Arabidopsis*.” (see bibliography [9]).

5.2. Biophysical basis for edge-induced catastrophe

larger curvature results in a higher edge-induced catastrophe probability, and finally that promoting the stability of MTs can result in a lower edge-induced catastrophe probability.

A particular cell edge has angle θ and curvature κ . The path length l , curvature κ (specifically, the inverse of an inscribed circle's radius, measured in μm^{-1}) and angle θ are related by $\kappa l = \theta$. Theoretically, the probability of bypassing an edge, p_{bypass} , depends on both curvature and angle by the formula

$$p_{\text{bypass}} = 1 - \exp\left(-\frac{1}{v_g} f_{\text{cat}}(\kappa) \frac{\theta}{\kappa}\right)$$

where v_g is the MT growth velocity and the function $f_{\text{cat}}(\kappa)$ tells us how the catastrophe rate is affected by curvature. This probability accounts for spontaneous catastrophes that would have occurred even in the absence of curvature [2]. The probability of an edge-induced catastrophe, discounting spontaneous catastrophe, is

$$p_{\text{cat}} = \exp\left(\frac{f_{\text{cat}}(0) - f_{\text{cat}}(\kappa)}{v_g} \cdot \frac{\theta}{\kappa}\right). \quad (5.1)$$

The details of this relationship depend on the microscopic details of the edge interaction. Interestingly, Eq 5.1 says that if the curvature does not substantially increase the rate of catastrophe (if $f_{\text{cat}} \propto \kappa^\beta$ where $\beta < 1$), then the probability of bypassing an edge may actually increase with increasing curvature. This occurs since, for a fixed angle, low curvature means the MT is subject to retardation by the edge for longer. To illustrate how edge-induced catastrophe may occur, in the case where curvature substantially increases the rate of catastrophe, I assume $f_{\text{cat}}(\kappa) = f_{\text{cat}}^0 + f_{\text{cat}}^*(\kappa/\kappa_0)^3$.

According to the dimer-level model of MT assembly of VanBuren et al. [128] the free-space, no-curvature catastrophe rate is determined by the attachment rate k_{on} , the hydrolysis rate k_{hyd} and the bond energies. Allard et al. [2] extended this model to include physical impediments, which affect the attachment rate by a factor $k_{\text{on}} \rightarrow \alpha k_{\text{on}}$. The catastrophe rate depends on α : if α is nearly zero, f_{cat} is much higher. If α is nearly 1, then f_{cat} is close to its free-space value. An analogous factor α_{curv} is induced by curvature. There is evidence from the animal homologues of CLASP [92] that CLASP alters the MT assembly by modifying the hydrolysis rate k_{hyd} . This would give a new relationship between f_{cat} and α_{curv} , and also different growth velocities and free-space catastrophe rates (higher and slower, respectively). In turn, this determines how severely curvature affects catastrophe rates (via f_{cat}^0 and f_{cat}^1).

5.3. Computer modelling of cell edge effects on MT organization

The probability of catastrophe, as a function of edge curvature, is shown in Fig. 5.1. The probability of edge catastrophe has been measured in *Arabidopsis* leaf pavement cells, both in the presence and absence of CLASP. These are shown as dashed lines. The parameters, as well as the functional form of $f_{cat}(\kappa)$, used in this figure are illustrative of the phenomenon. Detailed derivation or experimental measurement of these parameters, including edge curvatures for different cell edges, are desirable to constrain quantitative values in the figure.

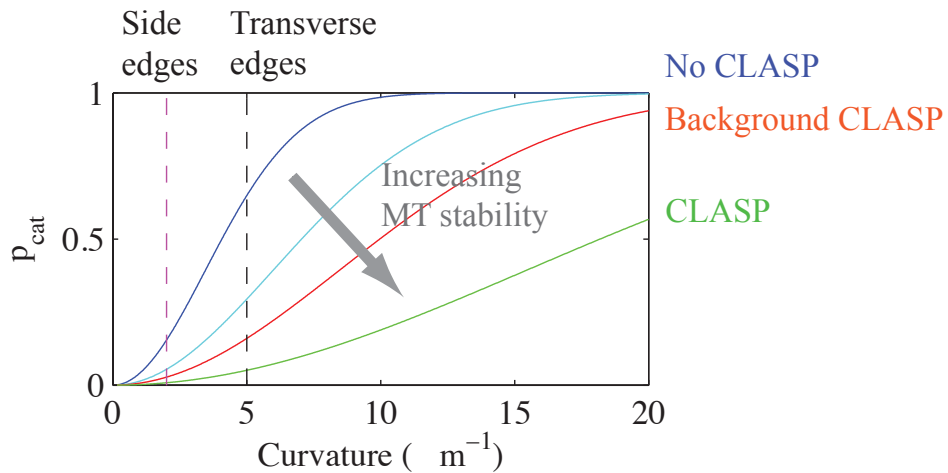


Figure 5.1: Probability of edge-induced catastrophe for different curvatures (for example, for side edges and transverse edges in root cells) and differences in MT stability (for example, as CLASP modulates the hydrolysis rate of GTP-tubulin dimers). Since the dependence of the catastrophe rate on curvature was chosen in an ad hoc manner, quantitative values in this figure are only illustrative.

5.3 Computer modelling of cell edge effects on MT organization

We used computational simulation [3] to test the hypothesis that MT organization can be controlled by modulating the ability of MTs to bypass the edges between cell faces. Using algorithms described in Allard et al. [3] and parameters measured in this study, we simulated MTs migrating around the

5.3. Computer modelling of cell edge effects on MT organization

cortex via dynamic instability at the plus-end and continuous depolymerization at the minus-end, and MT-MT interactions through entrainment at low angles of collision and collision-induced catastrophe at high angles of collision. We approximated the cell as a cube comprised of faces and edges. In our model, the cube's six faces are divided into three classes; periclinal, side, and transverse (see Fig 5.2A) and the cube's twelve edges are divided into three classes: side-periclinal (SP), transverse-side (TS), and transverse-periclinal (TP). We simulated the presence or absence of CLASP edge protein by modulating the ability of MTs to cross different edges. When a MT encounters an edge, it undergoes edge-induced catastrophe with probability p_i , where $i = \{SP, TS, TP\}$. The alternative outcome is growth of the MT past the edge.

Table 5.1: Edge-induced catastrophe probabilities used in simulations.

p_{SP}	p_{TS}	p_{TP}	Situation: Simulation results
0	0.95	0.95	<i>clasp-1</i> root cells: Transverse array (Fig. 5.2ABC)
0	0.85	0.10	WT dividing root cells: Mixed array (Fig. 5.2D,E)
0	0.85	0.85	WT elongating root cells: Transverse array

We assume SP edges never induce catastrophe, thus $p_{SP} = 0$. For TS and TP edges, we use the probabilities of edge-induced catastrophe measured in leaf cell edges with and without anticlinal bundles, as a proxy for edges with or without CLASP, respectively, in WT and in *clasp-1*, rounded to the nearest 5%. These values are shown in Table 5.1.

Simulations with low or no CLASP (Fig 5.2A), as in WT elongating root cells and *clasp-1* root cells, result in an array that is self-organized and whose dominant direction is transverse to the elongation axis in agreement with simulations in Allard et al. [3] and Eren et al. [48]. MT arrays on top and bottom faces self-organize into independent, random directions and are less dense.

If CLASP localizes to the transverse-periclinal edges, the increased ability of MTs to bypass the edge, as observed in WT division zone cells, generates a mixed orientation MT array (Fig 5.2D,E). MTs on the left and right side faces organize in the transverse direction, while MTs on the top and bottom transverse faces organize with dominant direction in-to-out (Fig 5.2D,E). MTs growing into the periclinal faces from the top and bottom faces promote longitudinal MTs on the periclinal faces, while MTs growing into the periclinal faces from the left and right faces promote transverse MTs on the periclinal faces. In this way, CLASP localization at the

5.3. Computer modelling of cell edge effects on MT organization

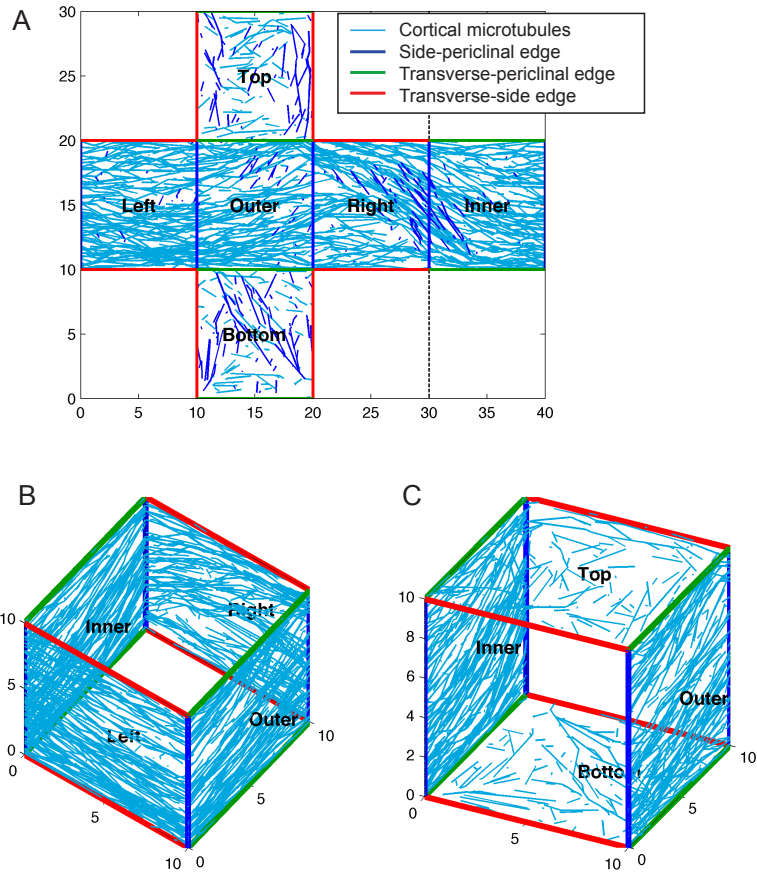


Figure 5.2: Simulations of CMT organization on a cube with differential edge interactions. (A)-(C) MTs can bypass side-periclinal edges (blue) but undergo catastrophe upon contact with transverse-periclinal and transverse-side edges (red, green). The same simulation is shown in (A), (B) and (C) in a flattened and 3D views. This edge interaction results in a transverse array on the side and periclinal faces, as in WT elongating and clasp-1 cells.

5.3. Computer modelling of cell edge effects on MT organization

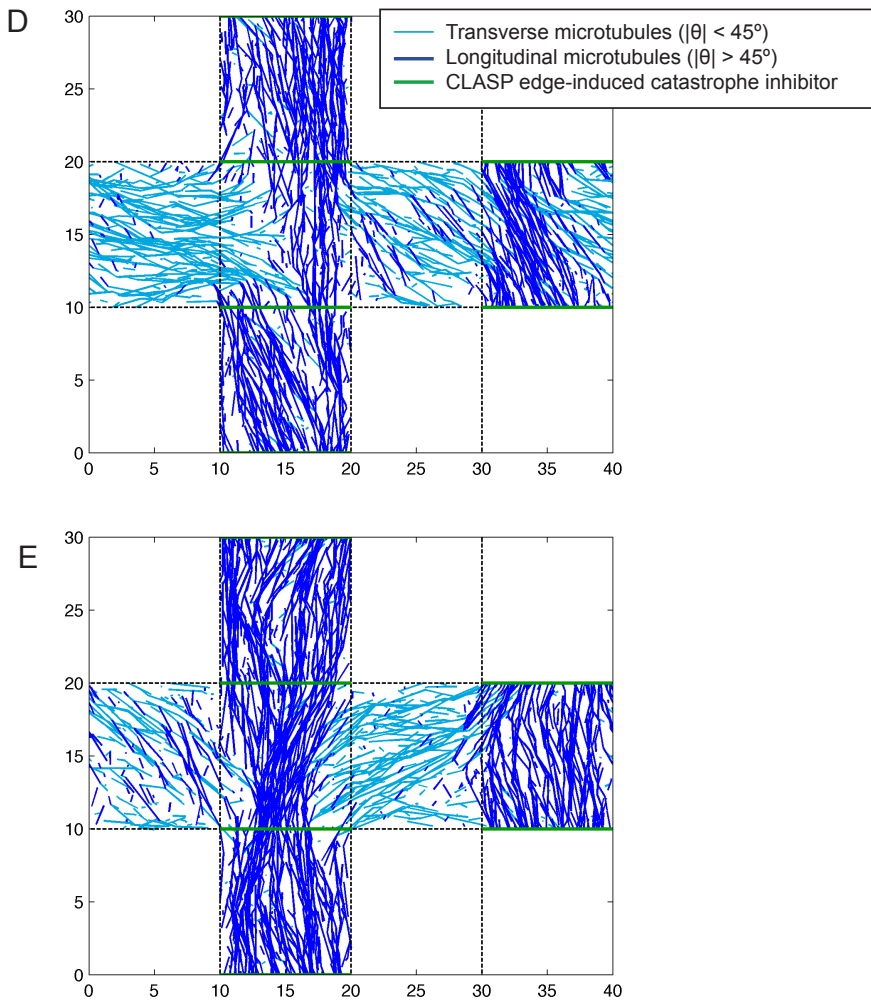


Figure 5.2: (D)-(E) During WT division, CLASP localizes to the transverse-periclinal edges, inhibiting edge-induced catastrophe. This leads to a mixed array with two subpopulations: mainly traverse (0-45 angle to the transverse axis, light blue) and mainly longitudinal (45-90, dark blue).

5.3. Computer modelling of cell edge effects on MT organization

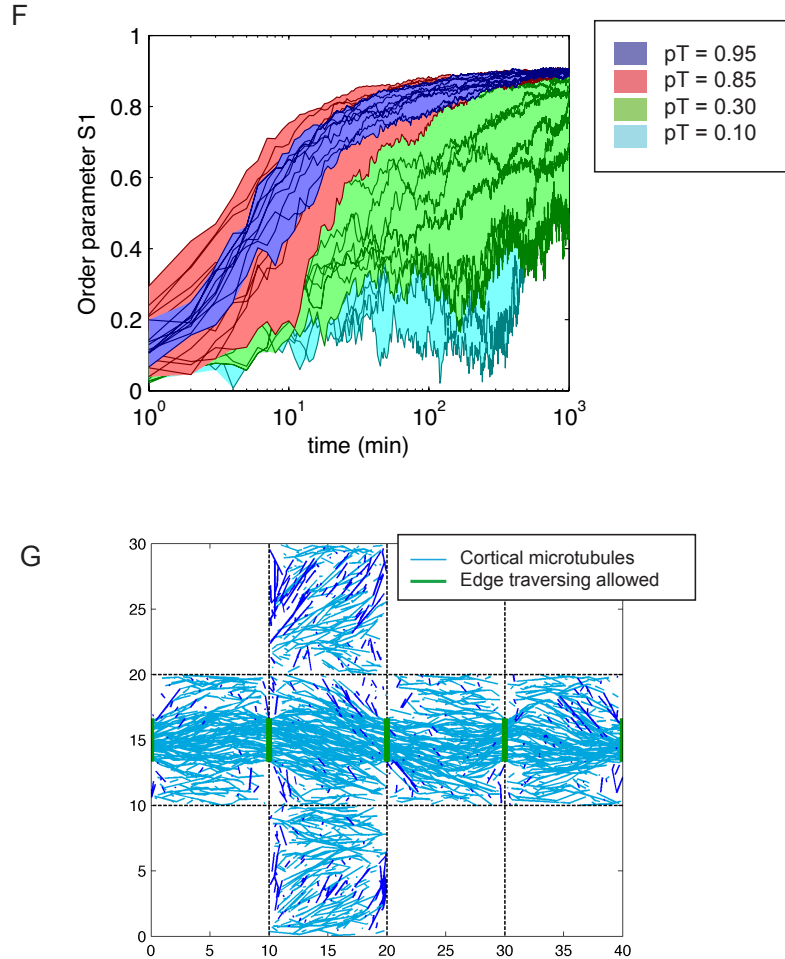


Figure 5.2: (F) Time series showing the order parameter S , defined in Eq. 4.14, for ten instances of simulations of WT elongating cells, *clasp-1* cells and two intermediate values of edge bypass probabilities. Shaded regions indicate the ranges of all ten simulations. Background levels of CLASP in the WT simulations lead to a slightly lower order parameter. (G) MTs are allowed to traverse the middle third of side-periclinal edges (green), resulting in a transverse band evocative of a PPB

5.4. Discussion

TP edge results in a mixed periclinal array, in agreement with experiment. Two examples are shown in Fig 5.2D,E.

Previously, Ambrose and Wasteneys [7] observed increased self-organization in the *clasp-1* null mutant compared to elongating WT cells, a difference that could not be explained by the postulated increased entrainment angle [3, 48]. During WT elongation phase, we assume there is a background level of CLASP still at the TS and TP edges, as suggested by different edge-induced catastrophe probabilities between WT and *clasp-1* elongating cells. Simulations in both cases (*clasp-1*, and WT elongating cells, which have a slightly lower edge-induced catastrophe probability at the TP and TS edges) result in a transverse array. The order parameter S , defined in Eq. 4.14, is shown in Fig 5.2F. In the presence of background CLASP, the variance of the time course of S is reduced for WT parameters (purple) compared with *clasp-1* parameters, however the steady-state order is the same. It is probable that the edge bypassing parameters in elongating root cells are different from that measured in leaf cells. For this reason, we ran simulations with edge bypass probabilities that were reduced further to $p_{TS} = p_{TP} = 0.3$. This resulted in more variability in the time course and lower organization (Fig 5.2F, green). Thus a background level of CLASP at the TP and TS edges in WT can explain the increased self-organization in *clasp-1* mutant observed in [7].

To test whether MT-edge interactions can produce more complex MT arrays, we simulated a cell in which only the middle third of SP edges allow MT traversing; the other two-thirds of SP edges and all TP and TS edges induce catastrophe. This results in a band of MTs organized in the transverse direction, with sparse, transient MTs outside the band, as shown in Fig 5.2G. This pattern is evocative of the PPB, as well as leaf epidermal cells that have non-uniform bundling on anticlinal walls. This suggests the cell may organize the PPB by tuning MT-edge interactions, either with CLASP or some other edge-localized MAP.

5.4 Discussion

The experimental work of Ambrose et al. [9] prompted the hypothesis that MT stabilization at cell edges by CLASP may allow cells to generate the transverse, longitudinal and mixed arrays observed in root cells, as well as patterns in leaf pavement cells and the pre-prophase band. Results from computational simulations support these findings, wherein modulating the degree of permissiveness to MT passage at a given edge can have dramatic

5.4. Discussion

effects on cell-wide MT organization.

The combined *in vivo* / *in silico* study leads to the proposal that plant cell edges fit the criteria of a MT organizing structure — by locally inducing catastrophe or allowing passage of MT plus-ends along cell edges, cell wide MT organization is affected. Taken together, our new findings indicate that CLASP action at anticlinal faces and edges works both locally to facilitate anticlinal MT bundle stability, as well as remotely to facilitate the net-like mixed arrays on periclinal cell faces. The ability to locally effect cell-wide MT ordering is consistent with the properties of a MT organizing centre, with the exception that it is spatially distributed, unlike the MTOC in MT asters and spindles (Sec. 1.2).

Chapter 6

Conclusions

6.1 Mathematical modelling techniques

An overarching principle of this research has been the connections between multiple scales and how the same physical object may be represented in different ways, depending on the scale. The nature of plant CMTs necessitated modelling from several nanometers to tens of microns.

- Representation of microtubules at the scale of individual dimers of tubulin allowed us to tease out the relationship between steric barriers, cortex anchoring and induced catastrophe, addressing the inconsistencies in experimental and theoretical literature. Specifically, differences in probabilities of catastrophe can be explained as differences in anchoring kinetics.
- Representation of microtubules as elastic bodies to which MAPs bind allowed for a mechanistic description of entrainment. This mechanical description acts as a framework to address questions as they arise at other scales. For example, cell-scale simulations could make two assumptions when treating entrainment or catastrophe of bundles of MTs [126]: when a bundle of MTs is incident upon another bundle, it can be treated as either one collision resolution that moves the entire incident bundle, one collision per incident MT, or one collision resolution for each pair of incident and barrier MTs. The mechanical description of entrainment we developed suggests entrainment events are approximately independent, and the latter pairwise treatment of entrainment is more appropriate, while collision-induced catastrophe can be explained as a steric obstruction, so an incident MT colliding with a bundle of barrier MTs will only feel the leading barrier.
- Representation of microtubules as a series of line segments allowed efficient large-scale simulation of thousands of interacting MTs. These simulations provided the first verification of a phenomenon that had

6.2. The reductionist approach in cell biology

been hypothesized for several years, i.e., that MT-MT interactions can generate parallel arrays on physiological timescales.

- Representation of microtubule arrays as faces on polyhedra allowed simulation of the CMT array in its *in vivo* geometry, and allowed for the testing of hypotheses generated by the concurrent experiments in the Wasteneys lab.

Each scale corresponds to a different aspect of the pathway leading to CMT organization. The overall model developed in this thesis is shown in Fig. 6.1. This pathway is itself one step in the larger pathway of plant morphogenesis, described in Fig. 2.2.

Different representations necessitated different mathematical tools, with two tools providing useful throughout the research. The first is random-timestep stochastic simulation (Gillespie methods [58]). In the case of the dimer-level model, it allows chemical rate stochasticity on the well-defined lattice of a 13-3 microtubule. In the case of cell-scale MT simulations, it allows the results to be compared with analysis of PDEs to an accuracy that was difficult to achieve with fixed-timestep stochastic simulation. The second tool is an energetic description of dynamics, which allows biochemistry (reaction rates and bond energies) to be combined with mechanics (elastic deformation energies and stresses).

6.2 The reductionist approach in cell biology

The reductionist approach in cell biology [112] suggests that phenomena can be understood by first understanding the constituent molecules and gradually building up to cell behaviour. This approach has met success in the cytoskeleton over the past decade in many fields, in each case moving from molecular models to intracellular structures to cell function: actin, filopodia and lamellipodia, and cell motility [27, 79]; microtubules, the mitotic spindle and mitosis [55, 75, 109]; the bacterial actin homologues, the MreB helix and bacterial growth [6]; and bacterial FtsZ, the cytokinetic Z-ring and bacterial division [4].

Insight from theoretical and experimental studies of these systems informs the present study of plant CMTs. In all cases, mechanics, biochemistry and self-organization give rise to a vital cell function. There are striking parallels between CMTs, which are involved in regulating the machinery for lateral cell wall (cellulose) insertion, and bacterial actin MreB [5, 6], which is also involved in regulating the machinery for lateral cell wall (peptidogly-

6.2. The reductionist approach in cell biology

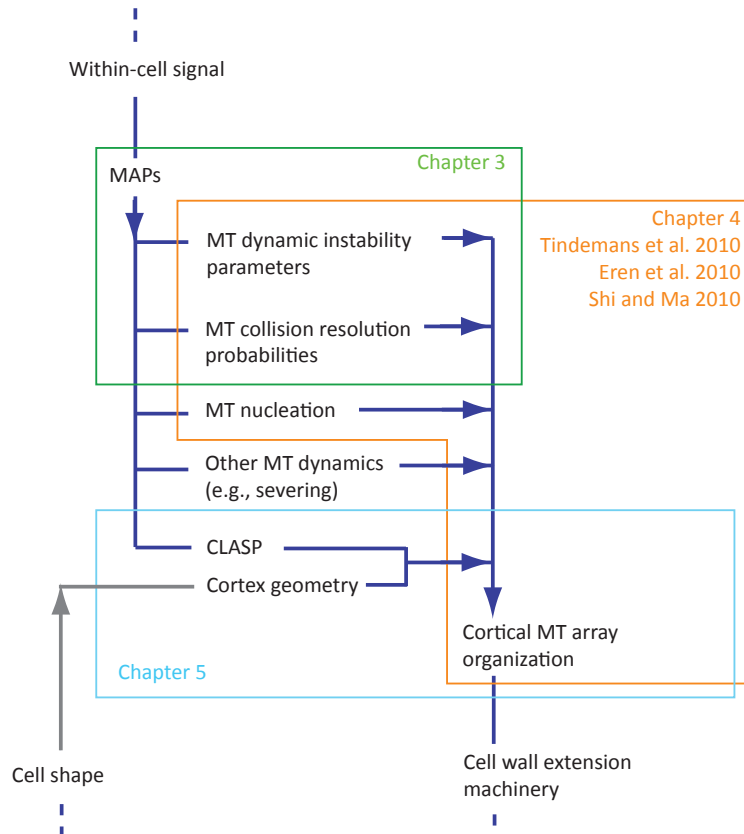


Figure 6.1: The pathway of CMT organization. MAPs such as MAP65 give rise to MT-MT interactions. CLASP combines with cell geometry to induce boundary conditions on the MTs. Together, MT-MT interactions and boundary conditions lead to the organization of the CMT array. Boxes indicate corresponding chapters in this thesis. This is part of a larger pathway of plant morphogenesis, shown in Fig. 2.2, in which this figure is a detail of the green box.

6.3. The appeal of modelling plant cortical microtubules

can) insertion. In both cases, the geometry of the stiff cell wall applies stress to the cytoskeletal elements, which self-organizes into well-defined patterns (parallel arrays and helices, respectively).

6.3 The appeal of modelling plant cortical microtubules

The plant CMT array provides an elegant system for mathematical modelling for many reasons:

- its two-dimensional nature
- its constituent parts, such as microtubules and cell membranes, are well-studied and relevant in other contexts,
- the analogies with other coarsening systems and aggregation phenomena, and
- its role in agriculture and biotechnology in governing plant growth and its relationship with cellulose.

Indeed, cellulose is a major component of the world economy, as the primary ingredient of the paper we print on, the cotton and rayon we wear, the dietary fibre in the food we eat, and possibly eventually in the cellulosic biofuel we use for transportation [19, 104].

Bibliography

- [1] B. Alberts, A. Johnson, J. Lewis, M. Raff, K. Roberts, and P. Walter. Molecular biology of the cell New York: Garland Science, 2002.
- [2] J.F. Allard, J.C. Ambrose, G.O. Wasteneys, and E.N. Cytrynbaum. A mechanochemical model explains interactions between cortical microtubules in plants. *Biophysical Journal*, 99:1082, 2010.
- [3] J.F. Allard, G.O. Wasteneys, and E.N. Cytrynbaum. Mechanisms of Self-Organization of Cortical Microtubules in Plants Revealed by Computational Simulations. *Molecular Biology of the Cell*, 21(2):278, 2010.
- [4] Jun F Allard and Eric N Cytrynbaum. Force generation by a dynamic z-ring in *Escherichia coli* cell division. *Proc Natl Acad Sci U S A*, 106(1):145–50, Jan 2009.
- [5] Jun F Allard and Andrew D Rutenberg. Steady-state helices of the actin homolog mreb inside bacteria: dynamics without motors. *Phys Rev E*, 76:031916, Sep 2007.
- [6] Jun F Allard and Andrew D Rutenberg. Pulling helices inside bacteria: imperfect helices and rings. *Phys Rev Lett*, 102(15):158105, Apr 2009.
- [7] J. Christian Ambrose and Geoffrey O. Wasteneys. CLASP Modulates Microtubule-Cortex Interaction during Self-Organization of Acentrosomal Microtubules. *Molecular Biology of the Cell*, 19(11):4730–4737, Nov 2008.
- [8] J. Christian Ambrose, Tsubasa Shoji, Amanda M. Kotzer, Jamie A. Pighin, and Geoffrey O. Wasteneys. The Arabidopsis CLASP Gene Encodes a Microtubule-Associated Protein Involved in Cell Expansion and Division. *Plant Cell*, 19(9):2763–2775, 2007.
- [9] J.C. Ambrose, J.F. Allard, E.N. Cytrynbaum, and Geoffrey O. Wasteneys. On the edge: Spatial cues from cell geometry is relayed

Bibliography

- to cortical microtubule arrays via clasp-based mtocs located along cell edges in arabidopsis. (*in progress*), 2010.
- [10] S.S. Antman and M. Renardy. Nonlinear problems of elasticity. Springer Berlin, 2005.
 - [11] E. Atilgan, D. Wirtz, and S.X. Sun. Mechanics and dynamics of actin-driven thin membrane protrusions. *Biophysical journal*, 90(1):65–76, 2006.
 - [12] C. Ballatore, M.Y.L. Virginia, and J.Q. Trojanowski. Tau-mediated neurodegeneration in Alzheimer’s disease and related disorders. *Nature Reviews Neuroscience*, 8(9):663–672, 2007.
 - [13] Alex Bannigan, Allison M D Wiedemeier, Richard E Williamson, Robyn L Overall, and Tobias I Baskin. Cortical microtubule arrays lose uniform alignment between cells and are oryzalin resistant in the arabidopsis mutant, radially swollen 6. *Plant Cell Physiol*, 47(7):949–58, Jul 2006.
 - [14] D.A. Barton, M. Vantard, and R.L. Overall. Analysis of cortical arrays from Tradescantia virginiana at high resolution reveals discrete microtubule subpopulations and demonstrates that confocal images of arrays can be misleading. *The Plant Cell Online*, 20(4):982, 2008.
 - [15] T.I. Baskin. On the alignment of cellulose microfibrils by cortical microtubules: A review and a model. *Protoplasma*, 215(1):150–171, 2001.
 - [16] Vladimir A. Baulin, Carlos M. Marques, and Fabrice Thalmann. Collision induced spatial organization of microtubules. *Biophysical Chemistry*, 128(2):231–244, 2007.
 - [17] D.D. Billadeau, J.C. Nolz, and T.S. Gomez. Regulation of t-cell activation by the cytoskeleton. *Nature Reviews Immunology*, 7(2):131–143, 2007.
 - [18] Sherryl R Bisgrove, Yuh-Ru Julie Lee, Bo Liu, Nick T Peters, and Darryl L Kropf. The microtubule plus-end binding protein eb1 functions in root responses to touch and gravity signals in arabidopsis. *Plant Cell*, 20(2):396–410, Feb 2008.
 - [19] Y.B. Blume, B. Baird, W. Vance, and A.I. Yemets. The Plant Cytoskeleton: a Key Tool for Agro-Biotechnology. Springer, 2009.

Bibliography

- [20] G.J. Brouhard, J.H. Stear, T.L. Noetzel, J. Al-Bassam, K. Kinoshita, S.C. Harrison, J. Howard, and A.A. Hyman. XMAP215 is a processive microtubule polymerase. *Cell*, 132(1):79–88, 2008.
- [21] L. Brun, B. Rupp, J.J. Ward, and F. Nédélec. A theory of microtubule catastrophes and their regulation. *Proceedings of the National Academy of Sciences*, 106(50):21173, 2009.
- [22] A. Burakov, E. Nadezhina, B. Slepchenko, and V. Rodionov. Centrosome positioning in interphase cells. *The Journal of cell biology*, 162(6):963, 2003.
- [23] D H Burk, B Liu, R Zhong, W H Morrison, and Z H Ye. A katanin-like protein regulates normal cell wall biosynthesis and cell elongation. *Plant Cell*, 13(4):807–27, Apr 2001.
- [24] David H Burk and Zheng-Hua Ye. Alteration of oriented deposition of cellulose microfibrils by mutation of a katanin-like microtubule-severing protein. *Plant Cell*, 14(9):2145–60, Sep 2002.
- [25] James F. Cahill, Jr. Gordon G. McNickle, Joshua J. Haag, Eric G. Lamb, Samson M. Nyanumba, and Colleen Cassady St. Clair. Plant root growth is modified in the presence of within-species competition and uneven local resource distributions. *Science*, 328(5986):1657, June 2010.
- [26] R. Carballido-Lopez. The bacterial actin-like cytoskeleton. *Microbiology and molecular biology reviews*, 70(4):888, 2006.
- [27] A.E. Carlsson. Actin dynamics: From nanoscale to microscale. *Annual Review of Cell and Developmental Biology*, 25:407–429, 2009.
- [28] P.M. Chaikin and T.C. Lubensky. Principles of condensed matter physics. Cambridge Univ Pr, 2000.
- [29] J. Chan, C.G. Jensen, L.C.W. Jensen, M. Bush, and C.W. Lloyd. The 65-kDa carrot microtubule-associated protein forms regularly arranged filamentous cross-bridges between microtubules. *Proceedings of the National Academy of Sciences*, 96(26):14931–14936, 1999.
- [30] J. Chan, G.M. Calder, J.H. Doonan, and C.W. Lloyd. EB1 reveals mobile microtubule nucleation sites in Arabidopsis. *Nature Cell Biology*, 5:967–971, 2003.

Bibliography

- [31] J. Chan, G. Calder, S. Fox, and C. Lloyd. Cortical microtubule arrays undergo rotary movements in *Arabidopsis* hypocotyl epidermal cells. *Nature Cell Biology*, 9:171–175, 2007.
- [32] Jordi Chan, Adrian Sambade, Grant Calder, and Clive Lloyd. *Arabidopsis* cortical microtubules are initiated along, as well as branching from, existing microtubules. *Plant Cell*, 21(8):2298–306, Aug 2009.
- [33] E. Chanliaud, K.M. Burrows, G. Jeronimidis, and M.J. Gidley. Mechanical properties of primary plant cell wall analogues. *Planta*, 215 (6):989–996, 2002.
- [34] M.A. Chesarone, A.G. DuPage, and B.L. Goode. Unleashing formins to remodel the actin and microtubule cytoskeletons. *Nature Reviews Molecular Cell Biology*, 11(1):62–74, 2009.
- [35] Vijay Chickarmane, Adrienne H K Roeder, Paul T Tarr, Alexandre Cunha, Cory Tobin, and Elliot M Meyerowitz. Computational morphodynamics: a modeling framework to understand plant growth. *Annu Rev Plant Biol*, 61:65–87, Jun 2010.
- [36] M.M.A.E. Claessens, M. Bathe, E. Frey, and A.R. Bausch. Actin-binding proteins sensitively mediate F-actin bundle stiffness. *Nature Materials*, 5(9):748–753, 2006.
- [37] DA Collings and GO Wasteneys. Actin microfilament and microtubule distribution patterns in the expanding root of *Arabidopsis thaliana*. *Canadian Journal of Botany*, 83(6):579–590, Jun 2005.
- [38] C. Conde and A. Cáceres. Microtubule assembly, organization and dynamics in axons and dendrites. *Nature Reviews Neuroscience*, 10 (5):319–332, 2009.
- [39] R J Cyr and B A Palevitz. Organization of cortical microtubules in plant cells. *Curr Opin Cell Biol*, 7(1):65–71, Feb 1995.
- [40] EN Cytrynbaum, V. Rodionov, and A. Mogilner. Computational model of dynein-dependent self-organization of microtubule asters. *Journal of cell science*, 117(8):1381, 2004.
- [41] PG De Gennes. The Physics of Liquid Crystals. *Mol. Cryst. Liq. Cryst*, 21:49, 1973.

Bibliography

- [42] P. Dhonukshe, A.M. Laxalt, J. Goedhart, T.W.J. Gadella, and T. Munnik. Phospholipase D activation correlates with microtubule reorganization in living plant cells. *The Plant Cell*, 15(11):2666, 2003.
- [43] J.F. Diaz, I. Barasoain, and J.M. Andreu. Fast Kinetics of Taxol Binding to Microtubules. *Journal of Biological Chemistry*, 278(10):8407–8419, 2003.
- [44] Ram Dixit and Richard Cyr. Encounters between Dynamic Cortical Microtubules Promote Ordering of the Cortical Array through Angle-Dependent Modifications of Microtubule Behavior. *Plant Cell*, 16(12):3274–3284, 2004.
- [45] Ram Dixit, Eric Chang, and Richard Cyr. Establishment of Polarity during Organization of the Acentrosomal Plant Cortical Microtubule Array. *Mol. Biol. Cell*, 17(3):1298–1305, 2006.
- [46] Marileen Dogterom and Stanislas Leibler. Physical aspects of the growth and regulation of microtubule structures. *Phys. Rev. Lett.*, 70(9):1347–1350, Mar 1993.
- [47] David W. Ehrhardt and Sidney L. Shaw. Microtubule dynamics and organization in the plant cortical array. *Annual Review of Plant Biology*, 57(1):859–875, 2006.
- [48] Ezgi Can Eren, Ram Dixit, and Natarajan Gautam. A 3d computer simulation model reveals the mechanisms for self-organization of plant cortical microtubules into oblique arrays. *Mol Biol Cell*, Jun 2010.
- [49] M.J. Farrer. Genetics of parkinson disease: paradigm shifts and future prospects. *Nature Reviews Genetics*, 7(4):306–318, 2006.
- [50] Flyvbjerg, Holy, and Leibler. Microtubule dynamics: Caps, catastrophes, and coupled hydrolysis. *Phys Rev E Stat Phys Plasmas Fluids Relat Interdiscip Topics*, 54(5):5538–5560, Nov 1996.
- [51] Jirí Friml and Klaus Palme. Polar auxin transport—old questions and new concepts? *Plant Mol Biol*, 49(3-4):273–84, 2002.
- [52] Ying Fu, Tongda Xu, Lei Zhu, Mingzhang Wen, and Zhenbiao Yang. A rop gtpase signaling pathway controls cortical microtubule ordering and cell expansion in arabidopsis. *Curr Biol*, 19(21):1827–32, Nov 2009.

Bibliography

- [53] J.C. Gardiner, J.D.I. Harper, N.D. Weerakoon, D.A. Collings, S. Ritchie, S. Gilroy, R.J. Cyr, and J. Marc. A 90-kD phospholipase D from tobacco binds to microtubules and the plasma membrane. *The Plant Cell Online*, 13(9):2143–2158, 2001.
- [54] M.K. Gardner, C.G. Pearson, B.L. Sprague, T.R. Zarzar, K. Bloom, ED Salmon, and D.J. Odde. Tension-dependent regulation of microtubule dynamics at kinetochores can explain metaphase congression in yeast. *Molecular biology of the cell*, 16(8):3764–3775, 2005.
- [55] M.K. Gardner, D.C. Bouck, L.V. Paliulis, J.B. Meehl, E.T. O'Toole, J. Haase, A. Soubry, A.P. Joglekar, M. Winey, E.D. Salmon, et al. Chromosome congression by Kinesin-5 motor-mediated disassembly of longer kinetochore microtubules. *Cell*, 135(5):894–906, 2008.
- [56] M.K. Gardner, A.J. Hunt, H.V. Goodson, and D.J. Odde. Microtubule assembly dynamics: new insights at the nanoscale. *Current Opinion in Cell Biology*, 2008.
- [57] A Gierer and H Meinhardt. A theory of biological pattern formation. *Kybernetik*, 12(1):30–9, Dec 1972.
- [58] D.T. Gillespie. Exact stochastic simulation of coupled chemical reactions. *The journal of physical chemistry*, 81(25):2340–2361, 1977.
- [59] Verônica A Grieneisen, Jian Xu, Athanasius F M Marée, Paulien Hogeweg, and Ben Scheres. Auxin transport is sufficient to generate a maximum and gradient guiding root growth. *Nature*, 449(7165):1008–13, Oct 2007.
- [60] S.W. Grill and A.A. Hyman. Spindle positioning by cortical pulling forces. *Developmental cell*, 8(4):461–465, 2005.
- [61] Olivier Hamant, Marcus G Heisler, Henrik Jönsson, Paweł Krupinski, Magalie Uyttewaal, Plamen Bokov, Francis Corson, Patrik Sahlin, Arezki Boudaoud, Elliot M Meyerowitz, Yves Couder, and Jan Traas. Developmental patterning by mechanical signals in arabidopsis. *Science*, 322(5908):1650–5, Dec 2008.
- [62] W.O. Hancock and J. Howard. Kinesin's processivity results from mechanical and chemical coordination between the ATP hydrolysis cycles of the two motor domains. *Proceedings of the National Academy of Sciences*, 96(23):13147–13152, 1999.

Bibliography

- [63] AR Hardham and BES Gunning. Structure of cortical microtubule arrays in plant cells. *J. Cell Biol.*, 77:14–34, 1978.
- [64] T. Hashimoto and T. Kato. Cortical control of plant microtubules. *Current Opinion in Plant Biology*, 9(1):5–11, 2006.
- [65] R.J. Hawkins, S.H. Tindemans, and B.M. Mulder. A model for the orientational ordering of the plant microtubule cortical array. *Physical Review E*, 83(011911), 2010.
- [66] D. Haynie. Biological thermodynamics. Cambridge University Press, 2008.
- [67] Z Hejnowicz. Autonomous changes in the orientation of cortical microtubules underlying the helicoidal cell wall of the sunflower hypocotyl epidermis: spatial variation translated into temporal changes. *Protoplasma*, 225(3-4):243–56, Oct 2005.
- [68] Harald Herrmann, Sergei V Strelkov, Peter Burkhard, and Ueli Aebi. Intermediate filaments: primary determinants of cell architecture and plasticity. *J Clin Invest*, 119(7):1772–83, Jul 2009.
- [69] R. Himmelsbach, R.E. Williamson, and G.O. Wasteneys. Cellulose microfibril alignment recovers from DCB-induced disruption despite microtubule disorganization. *Plant Journal*, 36(4):565, 2003.
- [70] D.M. Holloway. The role of chemical dynamics in plant morphogenesis (1). *Biochemical Society transactions*, 38(2):645, 2010.
- [71] J. Howard. Mechanics of Motor Proteins and the Cytoskeleton (Sunderland, MA: Sinauer). 2001.
- [72] T. Ishida, S. Thitamadee, and T. Hashimoto. Twisted growth and organization of cortical microtubules. *Journal of Plant Research*, 120(1):61–70, 2007.
- [73] Takashi Ishida, Yayoi Kaneko, Megumi Iwano, and Takashi Hashimoto. Helical microtubule arrays in a collection of twisting tubulin mutants of arabidopsis thaliana. *Proc Natl Acad Sci U S A*, 104(20):8544–9, May 2007.
- [74] Marcel E Janson, Mathilde E de Dood, and Marileen Dogterom. Dynamic instability of microtubules is regulated by force. *J Cell Biol*, 161(6):1029–34, Jun 2003.

Bibliography

- [75] M.E. Janson, R. Loughlin, I. Lododice, C. Fu, D. Brunner, F.J. Nédélec, and P.T. Tran. Crosslinkers and motors organize dynamic microtubules to form stable bipolar arrays in fission yeast. *Cell*, 128(2):357–368, 2007.
- [76] Henrik Jönsson and Paweł Krupinski. Modeling plant growth and pattern formation. *Curr Opin Plant Biol*, 13(1):5–11, Feb 2010.
- [77] E. Karsenti, F. Nedelec, and T. Surrey. Modelling microtubule patterns. *Nat Cell Biol*, 8:1204–1211, 2006.
- [78] E. Kawamura and G.O. Wasteneys. MOR1, the *Arabidopsis thaliana* homologue of *Xenopus* MAP215, promotes rapid growth and shrinkage, and suppresses the pausing of microtubules *in vivo*. *Journal of Cell Science*, 121(24):4114, 2008.
- [79] K. Keren, Z. Pincus, G.M. Allen, E.L. Barnhart, G. Marriott, A. Mogilner, and J.A. Theriot. Mechanism of shape determination in motile cells. *Nature*, 453(7194):475–480, 2008.
- [80] Yulia A Komarova, Ivan A Vorobjev, and Gary G Borisy. Life cycle of mts: persistent growth in the cell interior, asymmetric transition frequencies and effects of the cell boundary. *J Cell Sci*, 115(Pt 17):3527–39, Sep 2002.
- [81] Zhaosheng Kong, Takashi Hotta, Yuh-Ru Julie Lee, Tetsuya Horio, and Bo Liu. The gamma-tubulin complex protein gcp4 is required for organizing functional microtubule arrays in *arabidopsis thaliana*. *Plant Cell*, 22(1):191–204, Jan 2010.
- [82] G.J.P.L. Kops, B.A.A. Weaver, and D.W. Cleveland. On the road to cancer: aneuploidy and the mitotic checkpoint. *Nature Reviews Cancer*, 5(10):773–785, 2005.
- [83] C. Kozlowski, M. Srayko, and F. Nedelec. Cortical microtubule contacts position the spindle in *C. elegans* embryos. *Cell*, 129(3):499–510, 2007.
- [84] M.C. Lagomarsino, M. Dogterom, and M. Dijkstra. Isotropic–nematic transition of long, thin, hard spherocylinders confined in a quasi-two-dimensional planar geometry. *The Journal of Chemical Physics*, 119:3535, 2003.

Bibliography

- [85] L.D. Landau and E.M. Lifshitz. Theory of elasticity, course of theoretical physics vol 7. VII, 3rd revised edition (Butterworth-Heinemann, London), 1995.
- [86] Marta Laskowski, Verônica A Grieneisen, Hugo Hofhuis, Colette A Ten Hove, Paulien Hogeweg, Athanasius F M Marée, and Ben Scheres. Root system architecture from coupling cell shape to auxin transport. *PLoS Biol*, 6(12):e307, Dec 2008.
- [87] MC Ledbetter and KR Porter. A “microtubule” in plant cell fine structure. *Journal of Cell Biology*, 19(1):239–250, 1963.
- [88] Jens Luders and Tim Stearns. Microtubule-organizing centres: a re-evaluation. *Nature Reviews Molecular Cell Biology*, 8(2):161–167, February 2007.
- [89] T. Mao, L. Jin, H. Li, B. Liu, and M. Yuan. Two microtubule-associated proteins of the arabidopsis map65 family function differently on microtubules. *Plant physiology*, 138(2):654, 2005.
- [90] Gennady Margolin, Ivan V Gregoretti, Holly V Goodson, and Mark S Alber. Analysis of a mesoscopic stochastic model of microtubule dynamic instability. *Phys Rev E*, 74:041920, Oct 2006.
- [91] B Mickey and J Howard. Rigidity of microtubules is increased by stabilizing agents. *J Cell Biol*, 130(4):909–17, Aug 1995.
- [92] Y. Mimori-Kiyosue, I. Grigoriev, G. Lansbergen, H. Sasaki, C. Matsui, F. Severin, N. Galjart, F. Grosveld, I. Vorobjev, S. Tsukita, et al. Clasp1 and clasp2 bind to eb1 and regulate microtubule plus-end dynamics at the cell cortex. *The Journal of cell biology*, 168(1):141, 2005.
- [93] G J Mitchison. Phyllotaxis and the fibonacci series. *Science*, 196(4287):270–5, Apr 1977.
- [94] T Mitchison and M Kirschner. Dynamic instability of microtubule growth. *Nature*, 312(5991):237–42, 1984.
- [95] S.K. Mitra, D.A. Hanson, and D.D. Schlaepfer. Focal adhesion kinase: in command and control of cell motility. *Nature Reviews Molecular Cell Biology*, 6(1):56–68, 2005.

Bibliography

- [96] A. Mogilner and L. Edelstein-Keshet. Selecting a common direction. I: How orientational order can arise from simple contact responses between interacting cells. *Journal of mathematical biology*, 33(6):619–660, 1995.
- [97] A. Mogilner and G. Oster. Cell motility driven by actin polymerization. *Biophysical Journal*, 71(6):3030–3045, 1996.
- [98] A. Mogilner, L. Edelstein-Keshet, and GB Ermentrout. Selecting a common direction. II. Peak-like solutions representing total alignment of cell clusters J. Math. Biol., 34:811–42, 1996.
- [99] S. Molloy. Bacterial pathogenesis: Chain of transmission. *Nature Reviews Microbiology*, 6(2):93, 2008.
- [100] T. Murata, S. Sonobe, T.I. Baskin, S. Hyodo, S. Hasezawa, T. Nagata, T. Horio, and M. Hasebe. Microtubule-dependent microtubule nucleation based on recruitment of big gamma-tubulin in higher plants. *Nature Cell Biology*, 7:961–968, 2005.
- [101] Masayoshi Nakamura and Takashi Hashimoto. A mutation in the arabidopsis gamma-tubulin-containing complex causes helical growth and abnormal microtubule branching. *J Cell Sci*, 122(Pt 13):2208–17, Jul 2009.
- [102] Francois Nedelec. Computer simulations reveal motor properties generating stable antiparallel microtubule interactions. *J. Cell Biol.*, 158 (6):1005–1015, 2002.
- [103] C. Nicholson. Transport: Keeping motors running smoothly. *Nature Reviews Neuroscience*, 9(4):249, 2008.
- [104] P. Nick. Plant microtubules. Springer-Verlag, 2000.
- [105] D.J. Odde, L. Cassimeris, and H.M. Buettner. Kinetics of microtubule catastrophe assessed by probabilistic analysis. *Biophys. J.*, 69:769–802, 1995.
- [106] D.J. Odde, L. Ma, A.H. Briggs, A. DeMarco, and M.W. Kirschner. Microtubule bending and breaking in living fibroblast cells. *J. Cell Sci*, 112:3283–3288, 1999.
- [107] D.J. Odde. Mitotic spindle: disturbing a subtle balance. *Current Biology*, 15(23):R956–R959, 2005.

Bibliography

- [108] L. Onsager. The effects of shape on the interaction of colloidal particles. *Annals of the New York Academy of Sciences*, 51(4 Molecular Interaction):627–659, 1949.
- [109] R. Paul, R. Wollman, W.T. Silkworth, I.K. Nardi, D. Cimini, and A. Mogilner. Computer simulations predict that chromosome movements and rotations accelerate mitotic spindle assembly without compromising accuracy. *Proceedings of the National Academy of Sciences*, 106(37):15708, 2009.
- [110] C.G. Pearson and K. Bloom. Dynamic microtubules lead the way for spindle positioning. *Nature Reviews Molecular Cell Biology*, 5(6):481–492, 2004.
- [111] M Pinot, F Chesnel, J Z Kubiak, I Arnal, F J Nedelec, and Z Gueroui. Effects of confinement on the self-organization of microtubules and motors. *Curr Biol*, 19(11):954–60, Jun 2009.
- [112] Thomas D Pollard. The cytoskeleton, cellular motility and the reductionist agenda. *Nature*, 422(6933):741–5, Apr 2003.
- [113] W.H. Press, B.P. Flannery, S.A. Teukolsky, and W.T. Vetterling. Numerical Recipes. Cambridge University Press, 2007.
- [114] F.M. Reza. An introduction to information theory. Dover Publications, 1994.
- [115] S.M. Ross. Introduction to probability models. Academic press, 2007.
- [116] Robert J. Rubin. Mean Lifetime of Microtubules Attached to Nucleating Sites. *Proceedings of the National Academy of Sciences*, 85(2):446–448, 1988.
- [117] H.T. Schek, M.K. Gardner, J. Cheng, D.J. Odde, and A.J. Hunt. Microtubule assembly dynamics at the nanoscale. *Current Biology*, 17(17):1445–1455, 2007.
- [118] J.C. Sedbrook and D. Kaloriti. Microtubules, MAPs and plant directional cell expansion. *Trends in Plant Science*, 13(6):303–310, 2008.
- [119] D. Seetapun and D.J. Odde. Cell-length-dependent microtubule accumulation during polarization. *Current Biology*, 2010.

Bibliography

- [120] Sidney L. Shaw, Roheena Kamyar, and David W. Ehrhardt. Sustained Microtubule Treadmilling in *Arabidopsis* Cortical Arrays. *Science*, 300(5626):1715–1718, 2003.
- [121] Xia-Qing Shi and Yu-Qiang Ma. Understanding phase behavior of plant cell cortex microtubule organization. *Proc Natl Acad Sci U S A*, Jun 2010.
- [122] V. Stoppin-Mellet, J. Gaillard, and M. Vantard. Katamin’s severing activity favors bundling of cortical microtubules in plants. *The Plant Journal*, 46(6):1009–1017, 2006.
- [123] D.B. Szymanski. Plant cells taking shape: new insights into cytoplasmic control. *Current opinion in plant biology*, 12(6):735–744, 2009.
- [124] K Takesue and H Shibaoka. The cyclic reorientation of cortical microtubules in epidermal cells of azuki bean epicotyls: the role of actin filaments in the progression of the cycle. *Planta*, 205(4):539–46, Aug 1998.
- [125] G.W. Tian, D. Smith, S. Gluck, and T.I. Baskin. Higher plant cortical microtubule array analyzed in vitro in the presence of the cell wall. *Cell motility and the cytoskeleton*, 57(1):26–36, 2004.
- [126] S.H. Tindemans, R.J. Hawkins, and B.M. Mulder. Survival of the aligned: ordering of the plant cortical microtubule array. *Physical Review Letters*, 104(5):58103, 2010.
- [127] D. Van Damme, K. Van Poucke, E. Boutant, C. Ritzenthaler, D. Inze, and D. Geelen. In Vivo Dynamics and Differential Microtubule-Binding Activities of MAP65 Proteins 1. *Plant Physiology*, 136(4):3956–3967, 2004.
- [128] V. VanBuren, D.J. Odde, and L. Cassimeris. Estimates of lateral and longitudinal bond energies within the microtubule lattice. *Proceedings of the National Academy of Sciences*, 99(9):6035, 2002.
- [129] V. VanBuren, L. Cassimeris, and D.J. Odde. Mechanochemical model of microtubule structure and self-assembly kinetics. *Biophysical journal*, 89(5):2911–2926, 2005.
- [130] Geoffrey O. Wasteneys. Microtubule organization in the green kingdom: chaos or self-order? *J Cell Sci*, 115(7):1345–1354, 2002.

Bibliography

- [131] Geoffrey O. Wasteneys and Zhenbiao Yang. New Views on the Plant Cytoskeleton. *Plant Physiol.*, 136(4):3884–3891, 2004.
- [132] G.O. Wasteneys and J.C. Ambrose. Spatial organization of plant cortical microtubules: close encounters of the 2D kind. *Trends in cell biology*, 19(2):62–71, 2009.
- [133] G.O. Wasteneys and M. Fujita. Establishing and maintaining axial growth: wall mechanical properties and the cytoskeleton. *Journal of Plant Research*, 119(1):5–10, 2006.
- [134] GO Wasteneys and Williamson RE. Cortical microtubule organization and internodal cell maturation in chara-corallina. *Botanica Acta*, 106 (2):136–142, APR 1993. ISSN 0932-8629.
- [135] G.O. Wasteneys and R.E. Williamson. Reassembly of microtubules in *Nitella tasmanica*: assembly of cortical microtubules in branching clusters and its relevance to steady-state microtubule assembly. *Journal of Cell Science*, 93(4):705–714, 1989.
- [136] AT Whittington, O. Vugrek, KJ Wei, NG Hasenbein, K. Sugimoto, MC Rashbrooke, and GO Wasteneys. MOR1 is essential for organizing cortical microtubules in plants. *Nature*, 411(6837):610–3, 2001.
- [137] C. Wicker-Planquart, V. Stoppin-Mellet, L. Blanchoin, and M. Vandard. Interactions of tobacco microtubule-associated protein MAP65-1b with microtubules. *Plant Journal*, 39(1):126, 2004.
- [138] R. Wightman and S.R. Turner. Severing at sites of microtubule crossover contributes to microtubule alignment in cortical arrays. *Plant Journal*, 52(4):742, 2007.
- [139] R. Wollman, EN Cytrynbaum, JT Jones, T. Meyer, JM Scholey, and A. Mogilner. Efficient chromosome capture requires a bias in the ‘search-and-capture’ process during mitotic-spindle assembly. *Current Biology*, 15(9):828–832, 2005.
- [140] M. Wuhr, S. Dumont, A.C. Greeny, D.J. Needelman, and T.J. Mitchison. How does a millimeter-sized cell find its center? *Cell cycle*, 8(8): 1115–1121, 2009.
- [141] L. Yang, D. Sept, and AE Carlsson. Energetics and dynamics of constrained actin filament bundling. *Biophysical journal*, 90(12):4295–4304, 2006.

Bibliography

- [142] J. Zhu and A.E. Carlsson. Growth of attached actin filaments. *The European Physical Journal E-Soft Matter*, 21(3):209–222, 2006.
- [143] A. Zumdieck, M.C. Lagomarsino, C. Tanase, K. Kruse, B. Mulder, M. Dogterom, and F. Julicher. Continuum description of the cytoskeleton: ring formation in the cell cortex. *Physical review letters*, 95(25):258103, 2005.

Appendix A

PDE models and the mean field approximation

A.1 The five-dimensional system

To develop a differential equations model of the MT-MT interactions zippering and collision-induced catastrophe, we can augment the Dogetrom-Leibler equations with interaction terms. Here, for simplicity, I consider the two-state model, however generalization to the three-state model is straightforward.

Since MTs are spatially extended polymers, one MT occupies a continuum of points in the (x, y) plane. Furthermore, one MT will collide with MTs at different angles. Thus, the model below must contain non-local terms in both (x, y) and θ .

Let $p(x, y, \theta, l, t)$ be the density of MTs with plus ends at (x, y) , length l sitting at an angle θ . We define θ so that a horizontal MT has $\theta = 0$. The minus end will therefore be at $(x - l\cos(\theta), y - l\sin(\theta))$.

$$\frac{\partial p_g}{\partial t} = -v_g \begin{pmatrix} \cos(\theta) \\ \sin(\theta) \end{pmatrix} \cdot \nabla p_g - (v_g - v_m) \frac{\partial p_g}{\partial l} + f_r p_s - f_c p_g \quad (\text{A.1})$$

$$- (CAT + ZIP_{away}) p_g + ZIP_{to}$$

$$\frac{\partial p_s}{\partial t} = v_s \begin{pmatrix} \cos(\theta) \\ \sin(\theta) \end{pmatrix} \cdot \nabla p_s + (v_s + v_m) \frac{\partial p_g}{\partial l} - f_r p_s + f_c p_g \quad (\text{A.2})$$

$$+ CAT p_g. \quad (\text{A.3})$$

The advection terms in both the growing and shrinking populations represent MT elongation and depolymerization. The linear exchange terms represent catastrophe and rescue, just as in the Dogetrom-Leibler model. The interaction terms representing collision induced catastrophe, zippering away from the angle θ and into the angle θ are

$$\begin{aligned}
CAT &= k_{cat} v_g \int_{\Omega_c} \int_0^\infty \int_0^{l'} p_{g+s}(x + \sigma \cos(\theta - \theta'), \\
&\quad y + \sigma \sin(\theta - \theta'), \theta - \theta', l') |\sin \theta'| d\sigma dl' d\theta' \\
ZIP_{away} &= k_{zip} v_g \int_{\Omega'_c} \int_0^\infty \int_0^{l'} p_{g+s}(x + \sigma \cos(\theta - \theta'), \\
&\quad y + \sigma \sin(\theta - \theta'), \theta - \theta', l') |\sin \theta'| d\sigma dl' d\theta' \\
ZIP_{to} &= k_{zip} v_g \int_{\Omega'_c} p_{g+s}(x, y, \theta - \theta', l) |\sin \theta'| d\theta' \\
&\quad \times \int_0^\infty \int_0^{l'} p_g(x + \sigma \cos(\theta), y + \sigma \sin(\theta), \theta, l') d\sigma dl'
\end{aligned}$$

The catastrophe region is $\Omega_c = [\theta_Z, \pi - \theta_Z] \cup [\pi + \theta_Z, 2\pi - \theta_Z]$. The boundary conditions in l are $p_g(x, y, \theta, 0, t) = k_n / (2\pi v_g)$ and $p \rightarrow 0$ as $l \rightarrow \infty$.

This system is second-order but is inherently five-dimensional: two spatial coordinates describing location on the membrane, one describing the length distribution, one describing the angle distribution, and time. This makes the nonlinear system difficult to numerically integrate or to analyze. For this reason, it is desirable to have a low-dimensional model that gives rise to orientational order.

A.2 Spatial homogenization

One possible way of simplifying the system is to remove the MT length dimension. I argue against this length-wise homogenization with the following thought experiment. If a subpopulation of N_1 microtubules have angle θ_1 , and another smaller subpopulation has $N_2 < N_1$ MTs at angle θ_2 , then the rate of collisions with Subpopulation 1 polymers incident upon Subpopulation 2 barriers is $\propto N_1 \times \bar{l}_2 N_2$ where \bar{l}_2 is the average length of an MT in Subpopulation 2, while the rate of collisions of Subpopulation 2 polymers incident upon Subpopulation 1 barriers is $\propto N_2 \times \bar{l}_1 N_1$. That is, the number of collisions with one MT incident upon another is proportional to the length of the barriers. If we ignore length, then the collisions with Subpopulation 1 MTs against Subpopulation 2 MTs will be exactly balanced by Subpopulation 2 MTs against Subpopulation 1 MTs. This symmetry eliminates any hope for the emergence of a dominant angle.

Another way of simplifying the full five-dimensional system is to assume spatial uniformity. Here, I will show that this direct spatial homogeniza-

A.2. Spatial homogenization

tion leads to a system of differential equations that does not give rise to orientational order.

If we assume the solution is uniform in space, $A p_g(x, y, \theta, l, t) = N_g(\theta, l, t)$ where A is the cell surface area and N_g now has units $\text{rad}^{-1} \mu\text{m}^{-1}$.

$$\begin{aligned}\frac{\partial N_g}{\partial t} &= -(v_g - v_m) \frac{\partial N_g}{\partial l} + f_r N_s - f_c N_g - (CAT + ZIP_{away}) N_g + ZIP_{to} \\ \frac{\partial N_s}{\partial t} &= +(v_s + v_m) \frac{\partial N_g}{\partial l} - f_r p_s + f_c N_g + CAT \cdot N_g \\ CAT &= p_{cat} \frac{v_g}{A} \int_{\Omega_c} \int_0^\infty l' N_{g+s}(\theta - \theta', l') |\sin \theta'| dl' d\theta' \\ ZIP_{away} &= p_{zip} \frac{v_g}{A} \int_{\Omega'_c} \int_0^\infty l' N_{g+s}(\theta - \theta', l') |\sin \theta'| dl' d\theta' \\ ZIP_{to} &= p_{zip} \frac{v_g}{A} \int_{\Omega'_c} N_g(\theta - \theta', l) |\sin \theta'| d\theta' \times \int_0^\infty l' N_{g+s}(\theta, l') dl'\end{aligned}$$

A.2.1 Asymptotic expansion in p

We can approximate the equilibrium solution in the limit where $p_{zip} \ll 1$. We expand $N(\theta, l) = N^{(0)} + pN^{(1)} + \dots$ to obtain for the $O(1)$ problem the interaction-free Dogterom and Leibler model with solution

$$N_g^0(\theta, l) = K e^{-l/\lambda_0} \quad (\text{A.4})$$

$$N_s^0(\theta, l) = \frac{v_g}{v_s} K e^{-l/\lambda_0} \quad (\text{A.5})$$

where $K = k_n/(2\pi v_g)$ and

$$\lambda_0 = \frac{v_g v_s}{v_s f_c - v_g f_r}. \quad (\text{A.6})$$

The $O(p)$ problem is

$$0 = -f_c N_g^{(1)} + f_r N_s^{(1)} - v_g N_g^{(1)'} \quad (\text{A.7})$$

$$- \frac{v_g}{A} K^2 e^{-l/\lambda_0} \int_{\Omega'_c} \int_0^\infty l' \left(1 + \frac{v_g}{v_s}\right) e^{-l'/\lambda_0} |\sin \theta'| dl' d\theta' \quad (\text{A.8})$$

$$+ \frac{v_g}{A} K^2 \int_{\Omega'_c} e^{-l/\lambda_0} |\sin \theta'| d\theta' \times \int_0^\infty l' \left(1 + \frac{v_g}{v_s}\right) e^{-l'/\lambda_0} dl' \quad (\text{A.9})$$

$$= -f_c N_g^{(1)} + f_r N_s^{(1)} - v_g N_g^{(1)'} \quad (\text{A.10})$$

A.2. Spatial homogenization

with solution

$$N_g^{(1)}(\theta, l) = K_1 e^{-l/\lambda_0} \quad (\text{A.11})$$

$$N_s^{(1)}(\theta, l) = \frac{v_g}{v_s} K_1 e^{-l/\lambda_0} \quad (\text{A.12})$$

Because the boundary conditions are independent of p , $K_1 = 0$ and there is no first-order correction. All higher order corrections are identically zero.

For catastrophe only, the $O(1)$ problem is identical to above (Eq. A.4-A.5). The $O(p)$ problem is

$$0 = -f_c N_g^{(1)} + f_r N_s^{(1)} - v_g N_g^{(1)'} \quad (\text{A.13})$$

$$- \frac{v_g}{A} N_g^{(0)} \int_{\Omega_c} \int_0^\infty l' N_g^{(0)}(\theta - \theta', l') |\sin \theta'| dl' d\theta' \quad (\text{A.14})$$

$$0 = +f_c N_g^{(1)} - f_r N_s^{(1)} + v_s N_g^{(1)'} \quad (\text{A.15})$$

$$+ \frac{v_g}{A} N_g^{(0)} \int_{\Omega_c} \int_0^\infty l' N_g^{(0)}(\theta - \theta', l') |\sin \theta'| dl' d\theta'. \quad (\text{A.16})$$

Inserting Eq. A.4-A.5 we obtain

$$0 = -f_c N_g^{(1)} + f_r N_s^{(1)} - v_g N_g^{(1)'} \quad (\text{A.17})$$

$$- \frac{v_g}{A} K e^{-l/\lambda_0} \int_0^\infty l' K \left(1 + \frac{v_g}{v_s}\right) e^{-l/\lambda_0} dl' \int_{\Omega_c} |\sin \theta'| d\theta' \quad (\text{A.18})$$

$$= -f_c N_g^{(1)} + f_r N_s^{(1)} - v_g N_g^{(1)'} \quad (\text{A.19})$$

$$- \frac{v_g}{A} K^2 \left(1 + \frac{v_g}{v_s}\right) e^{-l/\lambda_0} \lambda_0^2 \int_{\Omega_c} |\sin \theta'| d\theta'. \quad (\text{A.20})$$

Inserting the integral of the kernel, $\int_{\Omega_c} |\sin \theta'| d\theta' = 4 \cos \theta_Z$, we obtain

$$-f_c N_g^{(1)} + f_r N_s^{(1)} - v_g N_g^{(1)'} = C e^{-l/\lambda_0} \quad (\text{A.21})$$

$$+f_c N_g^{(1)} - f_r N_s^{(1)} + v_s N_g^{(1)'} = -C e^{-l/\lambda_0} \quad (\text{A.22})$$

where

$$C = 4 \frac{v_g}{A} K^2 \left(1 + \frac{v_g}{v_s}\right) \lambda_0^2 \cos \theta_Z. \quad (\text{A.23})$$

The solution is

$$N_g^{(1)}(l) = -C l e^{-l/\lambda_0} \quad (\text{A.24})$$

$$N_s^{(1)}(l) = +\frac{v_g}{v_s} C l e^{-l/\lambda_0}. \quad (\text{A.25})$$

A.2. Spatial homogenization

These functions have extrema at λ_0 . These functions are also independent of θ . In the perturbation expansion, interactions at $O(p)$ are felt through the $O(1)$ solutions, which are independent of θ . Thus, this approach will never lead to angular non-uniformity.

A.2.2 Discussion

The goal here is not to find a model that aggregates in the orientational dimension, but rather to find one that predicts the self-organizing regimes of the collision-induced catastrophe model and the zippering model in agreement with large-scale simulation presented in Chapter 4. Simple dimensional scaling arguments fail to answer this question, and a partial differential equations model derived from the Eulerian version of the model fails to exhibit self-organize.

If the full five-dimensional system is an exact Eulerian version of the rule-based model, without stochasticity, then integration of Eqs. A.3 should exhibit aggregation. With stochasticity removed, the bifurcation between self-organization and the lack of self-organization should be sharper. Numerical integration of a five-dimensional system of two equations is difficult, and a lower-dimensional version is desirable.

Appendix B

Orientational order parameters in 2D

B.1 Introduction

A population of directed polymers, described either individually by lengths and angles, (l_i, θ_i) , $i = 1..N$, or density $p(\theta, l)$, exhibiting directional aggregation are said to be in the nematic phase. To describe the extent of ordering, researchers define a single number, called an order parameter S . Often, $S = 0$ indicates a perfectly isotropic population, while $S = 1$ describes a perfectly nematic population. However, different researchers studying theoretical models of cortical MT organization have chosen slightly different order parameters. Here, I show that three of these order parameters are equal.

For convenience, I use the density description $p(\theta, l)$, and assume that MTs are weighted linearly in their length, thus the order parameter only depends on

$$p(\theta) = \int_0^\infty p(\theta, l) dl / \int_{-\pi/2}^{\pi/2} \int_0^\infty p(\theta, l) dl d\theta. \quad (\text{B.1})$$

This quantity is called $k(\theta)$ in Tindemans et al. [126]. Note Baulin et al. [16] weight MTs quadratically in weight, which is undesirable when considering MTs that can develop kinks after entrainment, edge interactions or severing.

B.2 Defining four order parameters

For Allard et al. [3] (and a generalization of Baulin et al. [16]), we define the cost function at a given angle

$$\sigma_0(\Omega) = \langle \cos^2(\theta_i - \Omega) \rangle. \quad (\text{B.2})$$

The angle Ω that minimizes the cost is considered the dominant angle. We can compute the dominant angle by expanding Eq. B.2. With the help of

B.2. Defining four order parameters

trigonometric identities, we find

$$\Omega = \frac{1}{2} \arctan \left(\frac{\langle \sin 2\theta_i \rangle}{\langle \cos 2\theta_i \rangle} \right), \quad (\text{B.3})$$

If instead of the cost function in Eq. B.2, we use the cost function

$$\sigma_n(\Omega) = \langle l^n \cos^2(\theta_i - \Omega) \rangle. \quad (\text{B.4})$$

for $n = 1, 2$ then we obtain length-weighted or square-length weighted versions of σ_0 , and an equivalent dominant angle Ω . Once we have computed the dominant angle Ω , we define the order parameter S_n to be

$$S_n = \frac{\sigma_n(\Omega) - \sigma_n(\Omega + \pi/2)}{\sigma_n(\Omega) + \sigma_n(\Omega + \pi/2)}. \quad (\text{B.5})$$

Setting $n = 2$ gives the order parameter used in [16]. For $n = 1$,

$$S_1 = \frac{\langle l(\cos^2(\theta - \Omega) - \sin^2(\theta - \Omega)) \rangle}{\langle l \rangle} \quad (\text{B.6})$$

or, if the dominant angle is $\Omega = 0$,

$$S_1 = \frac{\sum l (\cos^2 \theta - \sin^2 \theta)}{\sum l}. \quad (\text{B.7})$$

The reason we always use squared trig functions is that it ensures the differentiability that allows Eq. B.3 to be used to find the dominant angle. In terms of density, this is

$$S_A = \int_{-\pi/2}^{\pi/2} p(\theta) (\cos^2 \theta - \sin^2 \theta) d\theta, \quad (\text{B.8})$$

identical to S_S . Shi and Ma [121] derive an order parameter based on the classical nematic order parameter [28]. Define a matrix $Q_{\alpha\beta} = \int p(\hat{u})(2u_\alpha u_\beta - \delta_{\alpha\beta}) d\hat{u}$ where u_α and u_β are the orthonormal components of a unit vector \hat{u} . The classical nematic order parameter S is the largest eigenvalue of this real, symmetric matrix. In three dimensions, after much simplification, this is

$$S = \frac{3}{2} \int_{-\pi}^{\pi} \int_{-\pi/2}^{\pi/2} p(\theta, \phi) \cos^2 \theta \sin \theta d\theta d\phi - \frac{1}{2} \quad (\text{B.9})$$

B.2. Defining four order parameters

while in two dimensions, it is

$$S_S = \int_{-\pi/2}^{\pi/2} p(\theta) \cos(2\theta) d\theta \quad (\text{B.10})$$

$$= \int_{-\pi/2}^{\pi/2} p(\theta) (\cos^2 \theta - \sin^2 \theta) d\theta. \quad (\text{B.11})$$

which is identical to S_A . Tindemans et al. [126] use

$$S_T = \left| \int_{-\pi/2}^{\pi/2} p(\theta) \exp(2i\theta) d\theta \right| \quad (\text{B.12})$$

$$= \left(\left(\int_{-\pi/2}^{\pi/2} p(\theta) \cos(2\theta) d\theta \right)^2 + \left(\int_{-\pi/2}^{\pi/2} p(\theta) \sin(2\theta) d\theta \right)^2 \right)^{1/2}. \quad (\text{B.13})$$

While, once again, this appears distinct from the other order parameters, note that we can assume $\Omega = 0$ without loss of generality. From Eq. B.3, this means

$$\frac{1}{2} \arctan \left(\frac{\langle \sin 2\theta_i \rangle}{\langle \cos 2\theta_i \rangle} \right) = 0 \implies \langle \sin 2\theta_i \rangle = 0 \quad (\text{B.14})$$

and the second term in Eq. B.13 vanishes, thus S_T is also equal to S_A and S_S . This form is more convenient, since it does not require prior calculation of the dominant direction.

Finally, Eren et al. [48] use the discrete information entropy of the discrete distribution $P(\theta_i)$,

$$E = - \sum_i p(\theta_i) \ln(p(\theta)) \quad (\text{B.15})$$

which, in contrast to the above order parameters, is $E = 0$ for a perfectly aligned array and $E = \Delta\theta_i / (\theta_{max} - \theta_{min})$ for a perfectly uniform array, where $\Delta\theta = 1^\circ$ in their study. It is tempting to generalize discrete information entropy to continuous distributions,

$$E = - \int_{-\pi/2}^{\pi/2} p(\theta) \ln(p(\theta)) d\theta \quad (\text{B.16})$$

but this quantity has several unappealing properties, such as a value that diverges to $-\infty$ as $p(\theta) \rightarrow \delta(\theta - \Omega)$. This is a generic property of continuous entropy [114].